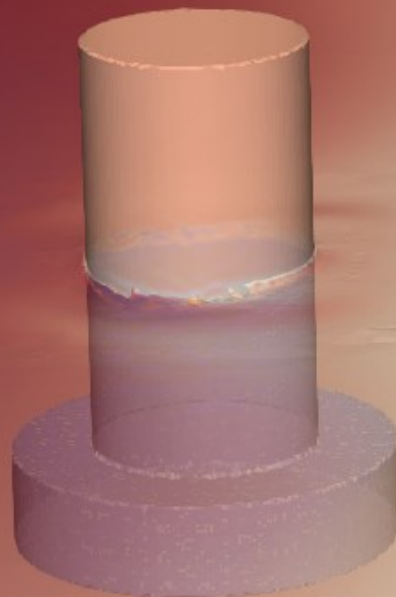
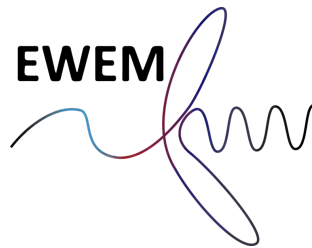


Comparison of Potential Flow and CFD for a Column With Heave Plate

Michiel Bots



This page intentionally left blank.



**EUROPEAN WIND ENERGY MASTER
OFFSHORE ENGINEERING**

**Comparison of Potential Flow and CFD for a Column With
Heave Plate**

**Master of Science Thesis
Thesis defence at the 24th of September 2020**

Michiel Willem Theodoor Bots
September 19, 2020

In partial fulfillment of the requirements for the degrees of



NORWEGIAN UNIVERSITY OF SCIENCE AND
TECHNOLOGY

Department of Marine Technology
Master of Science
Technology - Wind Energy



DELFT UNIVERSITY OF TECHNOLOGY

Faculty of 3mE
Master of Science
Offshore Engineering

Student number

517530

4343158

Assessment committee and supervisors

Prof. dr. E. Bachynski
Prof. dr. Z. Gao

Prof. dr. A. Metrikine
Dr. A. Viré
Dr. A. Antonini

An electronic version of this thesis is available at <http://repository.tudelft.nl/>

Preface

This master thesis has been written as part of the European Wind Energy Master. The thesis is the final deliverable in order for me to obtain a degree in Offshore and Dredging Engineering from Delft University of Technology and a degree in Technology - Wind Energy from the Norwegian University of Science and Technology (NTNU).

Handing in this thesis marks the end of two years of studying in the exciting field of offshore wind energy. Over the course of the last two years I have gained fascinating knowledge and developed myself both academically and personally. I am grateful for the interesting courses that have been able to take in Delft, Copenhagen and Trondheim.

Specifically with regards to this thesis I would like to thank dr. Axelle Viré for her guidance and supervision. Your guidance helped me steering my work into the right direction. I very much appreciated the time you took for our weekly meetings, even during the complicated COVID-19 times. Also, I would like to express my gratitude towards prof. dr. Erin Bachynski for her supervision and sharing her vast amount of knowledge on floating wind energy. Thank you to ir. Irene Rivera-Arebbba, for your help with setting up the software and introducing me to waves2Foam; this has helped me a lot. Furthermore, I would like to thank Mikko Folkersma, who helped me getting started and who's ample CFD experience has been very valuable to me. Thank you dr. Alessandro Antonini for your feedback and for sharing your experience with CFD and floating structures. Also, I would like to thank prof. dr. Andrei Metrikine for his valuable feedback and for chairing the assessment committee. Finally, I would like to express gratitude towards prof. dr. Zhen Gao for taking part in the assessment committee.

Finalising this thesis also marks the end of two very fun years, during which I have had the honour of studying in three different countries together with eleven talented EWEM students. I feel intensely grateful for the dear friendships I have made and the knowledge I have gained.

*Michiel Bots
Delft, September 2020*

Abstract

Floating offshore wind turbines can only withstand a limited amount of (heave) motions before the equipment fails. In order to reduce the heave motion, the DeepCwind floater for offshore floating wind turbines makes use of heave plates. This semi-submersible floater consists of three cylindrical columns with a heave plate attached to the bottom of each column. Potential flow models are often used in order to assess the response. However, potential flow theory does not take into account the viscosity and the vorticity of the fluid. Therefore, this thesis examines the effect of a heave plate on a cylindrical column's response in heave direction and subjected to wave loads with both a potential flow model and a fully nonlinear numerical wave tank. Specifically, the difference between a potential flow model and a fully nonlinear numerical wave tank is examined.

The simulations with the fully nonlinear numerical wave tank have been carried out using the open source computational fluid dynamics (CFD) software package OpenFOAM (version 1606+). An unresolved direct numerical simulation (DNS) approach is used throughout this work. Best practices for the dimensions of the wave tank, the mesh and settings of the solver were obtained from Bruinsma (2016) and Rivera-Arreba (2017). The OpenFOAM waves2Foam toolbox (developed by Jacobsen et al. (2012)) has been used to generate waves in the wave tank. The two phase solver interDyMFoam for moving bodies was coupled to the waveFoam solver from the waves2Foam toolbox in order to simulate a moving body under wave loads. The simulations in OpenFOAM were carried out on a 1:50 scale. The potential flow model WAMIT has been used in order to obtain the response amplitude operator (RAO), added mass, damping and wave excitation forces from potential flow theory.

A single cylindrical column has been tested in the numerical wave tank both with and without heave plate. Firstly, a heave decay test has been carried out. As a result, the linear damping ratio and the linear and quadratic damping coefficients have been determined. Secondly, the structure was exposed to incoming waves. The response of the structure has been assessed under three different wave periods, which were selected in order to align with Rivera-Arreba (2017). The response of the structure was measured, filtered on the frequency of the incoming wave and compared with the RAO from the potential flow model. Also, the wave excitation forces of the potential flow model have been compared with wave loads from the numerical wave tank, based on simulations where heave motion of the structure was constrained.

It was found that both the wave excitation forces and the RAO of the potential flow model are in agreement with the CFD model results. The viscous effects included in the CFD model affect the response of the structure only very lightly. The largest differences between the potential flow and CFD model were found around the heave cancellation wave frequency. At the heave natural period of the structure, the heave plate increases the linear damping coefficient with ca. 50%. The damping at this period was dominated by viscous effects. In general, the potential flow model produces an accurate RAO, due to the fact that the system is lightly damped and the damping therefore plays a minor role in the structure's response.

The outcome of this work contributes to the understanding of the effects of heave plates in general and can be used to assess the added value of computational expensive CFD software in the design process of floating wind systems.

Contents

- Preface i
- Abstract ii
- List of Tables vi
- List of Figures vii
- 1 Introduction 1
 - 1.1 Scope and Research Objectives 2
 - 1.2 Thesis Outline 4
- 2 Theory 5
 - 2.1 Floaters for Offshore Wind Turbines 5
 - 2.1.1 Hydrostatic-Stabilised Floaters 5
 - 2.1.2 Ballast-Stabilised Floaters 6
 - 2.1.3 Mooring-Stabilised Floaters 7
 - 2.1.4 Full Scale Applications 7
 - 2.2 Wave Theories 7
 - 2.3 Navier-Stokes equation 9
 - 2.4 Potential Flow Theory 10
 - 2.4.1 Governing Equations for Potential Flow Theory 10
 - 2.4.2 Potential Flow Building Blocks. 11
 - 2.4.3 Panel Method for Potential Flow Theory 11
 - 2.5 Governing Equations Navier-Stokes Solver. 12
 - 2.6 Heave Plates 14
 - 2.7 Damping and Added Mass of Heave Plates. 15
 - 2.8 Simplified Analytical Solution for Wave Structure Interaction Analysis 15
 - 2.9 Simplified Solution for Cylinder with Heave Plate and Cancellation Frequency. 18
 - 2.10 Decay Test 20

3	Numerical Tools	22
3.1	Navier Stokes Solver	22
3.1.1	WaveDyMFoam Solver	22
3.1.2	Discretisation	23
3.1.3	Pressure Velocity Coupling.	23
3.1.4	Relaxation Zone and Boundary Conditions.	25
3.1.5	Motion of the Structure (Fluid Structure Interaction)	25
3.1.6	Mesh Generation	27
3.1.7	Force and Wave Gauge Functions	27
3.2	Potential Flow Model: WAMIT.	28
4	Potential Flow Results	29
4.1	Added Mass.	29
4.2	Damping	31
4.3	Wave Excitation Forces.	32
4.4	Response Amplitude Operator	32
5	Case Study Column With and Without Heave Plate	35
5.1	Heave Decay Test.	35
5.1.1	Quantification of Viscous Damping.	38
5.2	Response Under Wave Loads	39
5.3	Wave Period $T = 12.1$ s	39
5.3.1	Spatial Domain	39
5.3.2	Wave Height and Transient Regime	41
5.3.3	Force and Displacement of the Structure	41
5.4	Wave Period $T = 8$ s	44
5.4.1	Spatial Domain	45
5.4.2	Wave Height and Transient Regime	46
5.4.3	Force and Displacement of the Structure	46
5.5	Wave Period $T = 17.4$ s	48
5.5.1	Spatial Domain	48
5.5.2	Wave Height and Transient Regime	48
5.5.3	Force and Displacement of the Structure	49
5.6	Visualisation Vorticity and y^+ -Values.	50
5.7	Viscous Forces and Pressure Forces.	52
5.8	Difficulties and Pitfalls With the Numerical Wave Tank	52

6	Comparison Potential Flow and CFD Results	54
6.1	RAO and Wave Excitation Forces	54
6.2	Natural Period	56
7	Conclusions and Recommendations	57
7.1	Conclusions.	57
7.2	Recommendations.	59
	Bibliography	61
A	Results OpenFOAM Simulations	64
A.1	Wave Period $T = 12.1$ s.	64
A.2	Wave Period $T = 8$ s	66
A.3	Wave Period $T = 17.4$ s.	69
B	OpenFOAM Code	73
B.1	fvSolution.	73
B.2	fvSchemes	77
B.3	waveDyMFoam.C	79

List of Tables

3.1	Discretization schemes	24
3.2	Boundary conditions	26
5.1	Mesh size heave decay test	36
5.2	Damping coefficients decay test	37
5.3	Damping coefficients from CFD and potential flow	38
5.4	Wave properties $T = 12.1$ s	39
5.5	Length spatial domain	40
5.6	Mesh size wave period $T = 12.1$ s	40
5.7	Measured mean wave height	41
5.8	Wave properties $T = 8$ s	45
5.9	Wave steepness kA	45
5.10	Mesh size wave period $T = 8$ s	46
5.11	Wave properties $T = 17.4$ s	48
5.12	Mesh size wave period $T = 17.4$ s	48

List of Figures

1.1	Annual offshore wind installations in Europe	1
1.2	Share of substructure types for grid-connected wind turbines	2
1.3	Schematic overview of the DeepCwind floater with the NREL 5 MW wind turbine on top.	3
1.4	Schematic overview of the column that has been assessed throughout this work	4
2.1	Illustration of floater classes	6
2.2	The Hywind Scotland wind farm under construction (Equinor, 2017).	7
2.3	Main wave parameters	8
2.4	Applicability of different wave theories	9
2.5	Potential flow building blocks (Journée and Massie, 2001).	12
2.6	Illustration of spatial discretisation schemes	13
2.7	Schematic overview of vertical floating cylinder	16
2.8	Visualisation of the flow separation around the edge of a heave plate	16
3.1	Schematic overview of flow domain	25
4.1	Added mass, damping and wave excitation force for column with heave plate	30
4.2	Added mass, damping and wave excitation force for column without heave plate	30
4.3	Wave excitation force	31
4.4	RAO for column with heave plate	32
4.5	RAO for column without heave plate	33
4.6	Wave excitation force subdivided	34
5.1	Heave decay test	36
5.2	Moving mean heave force	42
5.3	Amplitude of heave force normalized by buoyancy	42
5.4	Average heave force cycle for wave period $T = 12.1$ s	43
5.5	Heave motion for wave period $T = 12.1$ s	44
5.6	Average motion cycle for wave period $T = 12.1$ s	45
5.7	Heave motion for wave period $T = 8$ s	46

5.8	Average motion cycle for wave period $T = 8$ s	47
5.9	Heave motion for wave period $T = 17.4$ s	49
5.10	Average motion cycle for wave period $T = 17.4$ s	50
5.11	Flow visualisation column without heave plate $T = 8$ s	51
5.12	Flow visualisation column without heave plate $T = 12.1$ s	51
5.13	Flow visualisation column with heave plate $T = 17.4$ s	51
5.14	Flow visualisation column with heave plate $T = 12.1$ s	51
6.1	RAO for column with heave plate	55
6.2	RAO for column without heave plate	55
6.3	Wave excitation force	55
A.1	Average wave height over position in x-direction	64
A.2	Wave height	65
A.3	Heave force for wave period $T = 12.1$ s	65
A.4	PSD heave force column with heave plate	66
A.5	PSD heave force column without heave plate	66
A.6	Average wave height over position in x-direction	66
A.7	Wave height	67
A.8	Moving mean heave force	67
A.9	Amplitude of heave force normalized by buoyancy	67
A.10	Average heave force cycle for wave period $T = 8$ s	68
A.11	Heave force for wave period $T = 8$ s	68
A.12	PSD heave force column with heave plate	69
A.13	PSD heave force column without heave plate	69
A.14	Average wave height over position in x-direction	69
A.15	Wave height	70
A.16	Moving mean heave force	70
A.17	Amplitude of heave force normalized by buoyancy	70
A.18	Average heave force cycle for wave period $T = 17.4$ s	71
A.19	Heave force for wave period $T = 17.4$ s	71
A.20	Disturbances in heave force for wave period $T = 17.4$ s	72
A.21	PSD heave force column with heave plate	72
A.22	PSD heave force column without heave plate	72

1

Introduction

In order to fulfill the goals set by the Paris Agreement in 2015, countries worldwide have to reduce their CO₂ emissions (United Nations). Wind energy is considered a promising low carbon source of electric energy. Especially due to efforts from governments worldwide and a significant reduction of the levelized cost of energy (LCOE) by industry, specifically offshore wind energy is considered one of the cornerstones of the energy transition in (a.o.) North-West Europe. As a consequence, the cumulative installed capacity of offshore wind has grown steeply over the past decade (Figure 1.1).

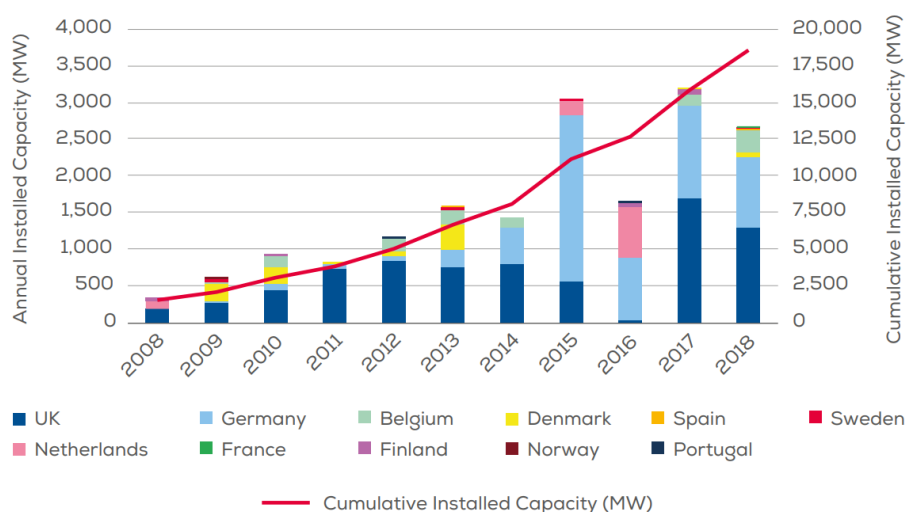


Figure 1.1: Annual offshore wind installations in Europe by country and cumulative capacity (MW) (Selot et al., 2019).

Currently, the most popular way of installing offshore wind turbines is bottom-founded structures. As can be seen in Figure 1.2, monopiles make up over three quarters of the offshore wind turbine foundations in Europe. However, bottom-founded structures are only viable for a restricted range of relatively low water depths. Floating wind turbines can be used in a larger range of water depths and thus offer a solution for countries with unsuitable water depths for bottom-founded foundations. Therefore, this promising technique is being investigated by both academia and industry.

Different design concepts for floating wind turbines exist (see Figure 2.1), but the focus of this report is on semi-submersible floaters. The column geometry that was used throughout this report, was based on the DeepCwind floater (see Figure 1.3). This floating wind system has been devel-

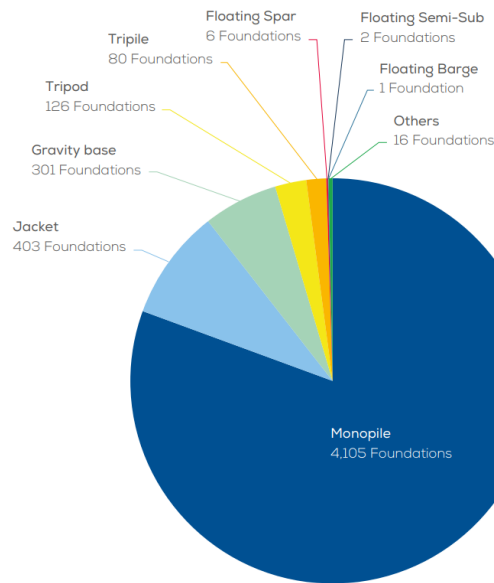


Figure 1.2: Share of substructure types for grid-connected wind turbines at the end of 2018 (Selot et al., 2019)

oped by an international cooperation of universities and research institutes and has been studied thoroughly as part of the Offshore Code Comparison Collaboration project. For the Offshore Code Comparison Collaboration Continued with Correlation project OC5 (Robertson et al., 2016) a scale model of a semi-submersible wind system has been tested. For the ongoing OC6 project, a specific focus is set towards the heave plates of the DeepCwind floater. These are horizontal plates attached to the bottom of all three main columns of the floater.

Heave plates are an important part the the floater. Since the equipment of the wind turbine can only withstand a limited amount of heave motion (motion in the vertical direction), heave plates are used in order to reduce the excitation in heave direction due to incoming waves. Potential flow theory based models are often used to calculate the hydrodynamic response of floating structures, such as the DeepCwind floater. A disadvantage of these type of models, is the fact that potential flow theory neglects the viscosity and vorticity of the fluid. Computational fluid dynamics models (CFD), such as the fully nonlinear Navier-Stokes numerical wave tank used throughout this work, overcome this issue. But this comes at great computational costs.

Therefore, this report aims to provide insight into the hydrodynamic response of a single column of a semi-submersible floater. Specifically, the added value of computational expensive CFD software in the design process of floating wind systems with heave plates is assessed, based on a comparison of CFD and potential flow model results. The geometry of the single column that is assessed throughout this work is largely based on the DeepCwind geometry, however, the diameter of the main column differs slightly.

1.1. Scope and Research Objectives

Two main research questions have been formulated. Answering these two main research questions, gives an insight into the hydrodynamic response of a single column similar to the DeepCwind floater columns. Also, based on a comparison between a potential flow model and a CFD model, the added value of CFD for this type of problems can be evaluated. The two main research questions that have been formulated are:

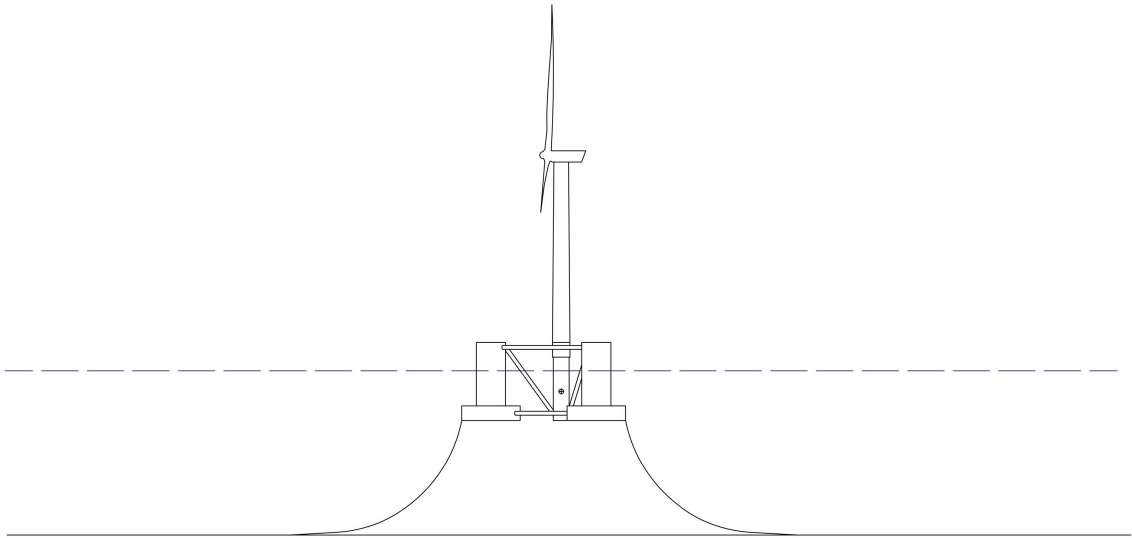


Figure 1.3: Schematic overview of the DeepCwind floater with the NREL 5 MW wind turbine on top (Rivera-Arreba, 2017).

- **How does a potential flow theory based model compare to a fully nonlinear Navier-Stokes numerical wave tank when applied to a single column with and without heave plate?**
- **How do the heave plates affect the (heave) dynamics of single column?**

The response of a floating body due to incoming waves, can be expressed in terms of a response amplitude operator (RAO). Another interesting statistic is the wave excitation force exerted by the waves on the floating structure. Since the RAO and the wave excitation force are usually normalized by the wave height, the latter is also an important statistic. Finally, since the damping is expected to be significantly affected by the presence of the heave plate, this is another relevant statistic. All of the aforementioned parameters have been calculated with both a potential flow model and a CFD model in order to answer the following sub-questions:

1. *How is the wave field in the numerical wave tank affected by the presence of the structure?*
2. *How do the wave excitation forces of a column with and without heave plate obtained with a potential flow theory based model compare to the wave excitation forces obtained with a fully nonlinear Navier-Stokes numerical wave tank?*
3. *How does the Response Amplitude Operator (RAO) of a column with and without heave plate obtained with a potential flow theory based model compare to the RAO obtained with a fully nonlinear Navier-Stokes numerical wave tank?*
4. *How much does the heave damping at the natural period increase due to the addition of a heave plate to the single column?*

Note that the geometry that was analysed in this report is based on the geometry of a single column of the DeepCwind floater, but is not exactly the same. The diameter of the main column used in this report is two meters (17%) larger than the DeepCwind main column. A schematic overview of the column with heave plate is depicted in Figure 1.4.

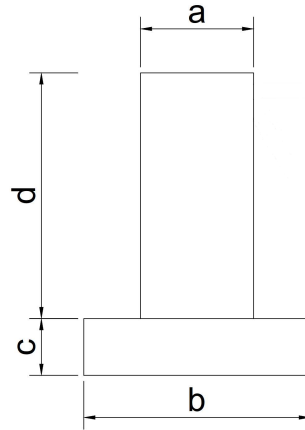


Figure 1.4: Schematic overview of the column that has been assessed throughout this work. The full-size dimensions are: $a = 14$ m, $b = 24$ m, $c = 6$ m, $d = 26$ m. Furthermore, the draft of the structure is 20 m. For the column without heave plate $b = a = 14$ m.

1.2. Thesis Outline

In order to answer the research questions mentioned above, simulations have been carried out with both a CFD model comprising the fully nonlinear Navier-Stokes numerical wave tank and a potential flow theory model. In Chapter 2 the underlying theory that is used throughout this work is touched upon, including the basic principles of potential flow theory and the governing equations for the Navier-Stokes solver. Next, Chapter 3 presents the numerical tools that have been used in order to carry out the simulations. The main features of the Navier-Stokes solver are explained as well as for the potential flow theory model.

Chapter 4 provides an overview of the results that were obtained using the potential flow theory model. Chapter 5 presents similar content for the results that were obtained from the Navier-Stokes solver. This chapter also includes a description of the spatial lay-out of the numerical wave tank and details on the wave properties that have been used, since these settings differ from case to case. Finally, Chapter 6 contains a comparison of the results from the numerical wave tank and the potential flow model. The conclusions of this work and recommendations are presented in Chapter 7.

2

Theory

This section includes an overview of the most important theory that has been used throughout this work. This ranges from floater types for offshore wind turbines, wave theory, the basics of potential flow theory and governing equations of Navier-Stokes solvers up to an analytical solution that can be used in order to describe the response of a column with(out) heave plate under wave loading.

2.1. Floaters for Offshore Wind Turbines

As the water depth increases, bottom founded foundations for offshore wind turbines become unviable, due to increasing costs and complexity of the structure. Floating wind turbines offer a solution for large waters depths. This section discusses the most common categorization of different types of floating wind turbines. Based on the way that the floater is stabilized in the water, Henderson and Witcher (2010) have defined three main classes of floater types. This classification will be used as the backbone for this section. Using this classification the following three classes can be distinguished:

- hydrostatic class;
which refers to structures using the water plane area to stabilize itself;
- ballast class; and
which refers to (typically) long and slender structures that stabilize themselves with a center of gravity below the center of buoyancy;
- mooring class (often referred to as tension leg platforms (TLP));
which refers to structures using a (tensioned) mooring system to stabilize themselves.

The main focus of this report is on the the DeepCwind semisubmersible floater, which within this classification falls under the hydrostatic class type of floaters.

2.1.1. Hydrostatic-Stabilised Floaters

The hydrostatic-stabilised floaters are, like a ship, stabilised by the waterplane area. The large wind loads on the top of the wind turbine tower typically make the floater heel over during operation. Since hydrostatic stabilised floaters are generally large structures, the hydrodynamic loads are relatively large. Especially, due to the relatively large waterplane area. Semi-submersible floaters, hav-

ing their hull well below the water surface, decrease the waterplane area compared to barge-type floaters.

Mathematically, the effect from semi-submersible type of floaters can be seen in Equation 2.1, which gives the linear stiffness for floating structures in pitch (Bachynski, 2018):

$$C_{55} + K_{55} = \rho g I_{55} - M g z_G + \rho g \nabla z_B + K_{55} \quad (2.1)$$

where C_{55} , represents the hydrostatic stiffness; and K_{55} , is the stiffness of the mooring system. The hydrostatic stiffness C_{55} is obtained from the mass M , the vertical centre of gravity z_G , the displaced volume ∇ , the centre of buoyancy z_B , and the water plane moment of inertia in pitch I_{55} . The latter can be described mathematically as (Bachynski, 2018):

$$I_{55} = \iint_{A_{wp}} x^2 dx dy \quad (2.2)$$

where A_{wp} represents the water plane area.

From this equation it can be seen that a more material efficient way to increase I_{55} is through adding material far from the central axis, rather than increasing the total area. This effect is what semi-submersible floaters use to achieve stability. The typical semi-submersible column structure is the result of application of this effect.

2.1.2. Ballast-Stabilised Floaters

Ballast-stabilised floaters are stabilised by bringing down the center of mass of the wind turbine as far as possible below the center of buoyancy. The fact that the wind load induces a large horizontal load at nacelle height, high above the water level, is especially challenging for this type of concept (Henderson and Witcher, 2010). This usually results in long and slender structures, with ballast attached to the bottom of the floater, well below water level, see Figure 2.1.

Again Equation 2.1 can be used to investigate mathematically how ballast stabilised floaters acquire stability. Equation 2.1 indicates that for a negative centre of gravity an increase in mass M and a decrease in the centre of gravity z_G increases the stiffness of the floater in pitch. Thus, adding ballast at the bottom of the floater increases the floater's stiffness in pitch, increasing the stability.

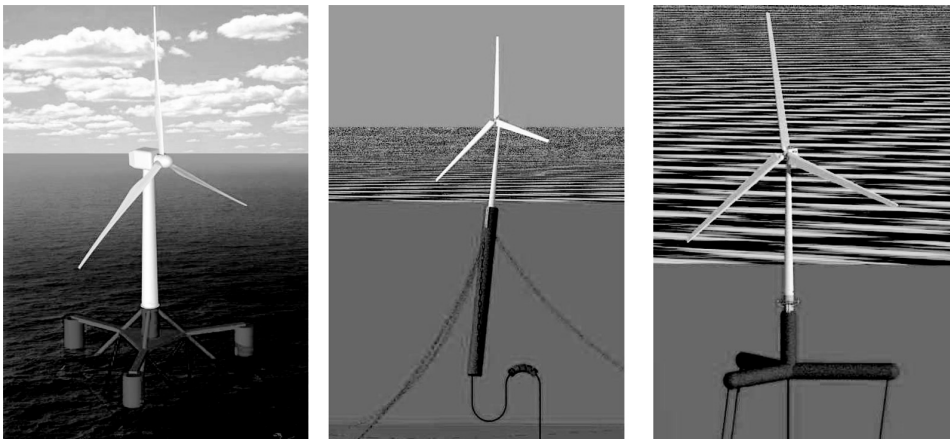


Figure 2.1: Illustration of each of the floater classes as defined by Henderson and Witcher (2010). From left to right: hydrostatic, ballast and mooring class (Henderson and Witcher, 2010)

2.1.3. Mooring-Stabilised Floaters

Mooring-stabilised floaters are floaters which acquire their stability from the mooring system. In contrast with hydrostatic- and ballast-stabilised floaters, which are usually moored with slack mooring lines, mooring-stabilised floaters are typically moored with vertical, tensioned mooring lines. Thus, the mooring stiffness K_{55} in Equation 2.1 is increased, which increases the stability of the floater.

2.1.4. Full Scale Applications

Each of the concepts discussed in this section - hydrostatic, ballast and mooring stabilised floaters - are being investigated and experimented with for wind turbines applications. Nevertheless, floating wind energy is still in an early stage of development. The largest offshore floating wind farm currently operating, is the Hywind Scotland 30 MW windfarm in the U.K. (WindEurope). This wind farm uses 5 spar type floaters, each of which carries a 6 MW wind turbine. In Figure 2.2 the installation of one of the spar type floaters is depicted. This operation is carried out by a semi-submersible ship.

Most floating wind turbines are mainly built for research and innovation purpose. The VoltrunUS wind turbine, which was developed by the University of Maine, is a good example of this. This ballast-stabilised system has been employed in-land in fresh water in 2013 (Danko, 2013).

A number of conceptual designs of floating wind turbines for research purpose exist. Throughout this work, the DeepCwind floater, depicted in Figure 1.3, is used (Robertson et al., 2016). In the past, both numerical and experimental tests have been performed with this floating wind turbine system. As a consequence, a lot of data is available on this floater. Throughout this study the work from Bruinsma (2016) and Rivera-Arreba (2017) is used extensively.

2.2. Wave Theories

Finding an accurate mathematical method to describe sea waves has been a subject of academic research for a long period of time. Especially wind waves, which are waves generated due to the



Figure 2.2: The Hywind Scotland wind farm under construction (Equinor, 2017).

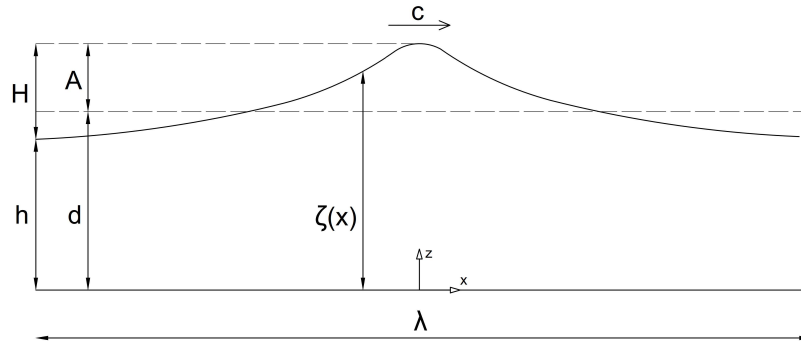


Figure 2.3: Main wave parameters that describe a regular wave propagating in x-direction. Modified from Fenton (1985).

wind blowing over the water surface, are an important feature for offshore structures, since they can induce high loads. The most important parameters to describe a wave mathematically are the wave period T (or the wave frequency $\omega = \frac{1}{T}$) and the wave height H , which is defined as the distance from the wave crest to the wave trough. Furthermore, the water depth d and the wave length λ are important parameters. The *dispersion relation* describes how these wave parameters are related, according to the following equation:

$$\left(\frac{2\pi}{T}\right)^2 = \omega^2 = gk \tanh(kd) \quad (2.3)$$

where g , is the gravitational acceleration; and $k = \frac{2\pi}{\lambda}$, is the wave number.

The ratio between the wave length and the wave period indicates the speed at which the wave crest proceeds and is referred to as the celerity: $c = \frac{\lambda}{T}$

The least complex method to mathematically describe a water wave is through Airy wave theory, which is also known as linear wave theory. According to Airy wave theory, waves can be described as purely sinusoidal. However, Airy wave theory is only valid under strictly defined conditions: the water depth shouldn't be too shallow, the wave steepness ($\frac{H}{\lambda}$) shouldn't be too high and the wave height has to be below the breaking limit. For the latter criterion, the breaking wave height H_{max} is defined as function of the water depth and wave length according to the following equation (Fenton, 1990):

$$\frac{H_{max}}{d} = \frac{0.141063 \frac{\lambda}{d} + 0.0095721 \left(\frac{\lambda}{d}\right)^2 + 0.0077829 \left(\frac{\lambda}{d}\right)^3}{1 + 0.0788340 \frac{\lambda}{d} + 0.0317567 \left(\frac{\lambda}{d}\right)^2 + 0.0093407 \left(\frac{\lambda}{d}\right)^3} \quad (2.4)$$

Under the Airy wave theory, the fluid flow is assumed to be inviscid, incompressible and irrotational. Also, it assumes a constant water depth. A significant advantage of this wave theory is the fact that the principal of superposition can be applied. Therefore, this wave theory is often used for the assessment of fatigue loads due to irregular waves.

As the wave steepness increases or the depth changes, other wave theories give a better approximation of the actual wave. A frequently used method to visualise the applicability of various wave theories is Figure 2.4. In this figure the regions of applicability of various wave theories are shown as functions of the non-dimensionalised wave height $\frac{H}{gT^2}$ and water depth $\frac{d}{gT^2}$. Rienecker and Fenton (1981) aimed to develop a wave model that could describe every type of wave on irrotational flow

over a horizontal sea bed. This so-called fully nonlinear stream function has been used throughout the work presented in this report. It relies on a finite Fourier series describing the surface elevation and uses Newton's method in order solve the Fourier coefficients.

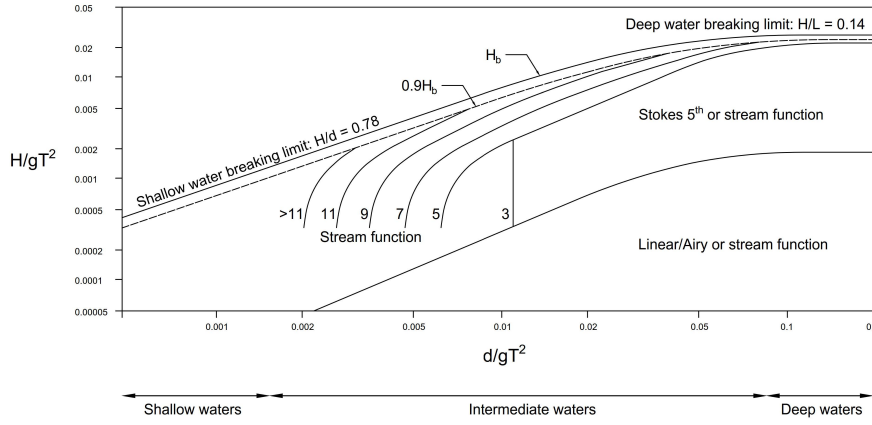


Figure 2.4: Limit of application for various wave theories, based on the non-dimensionalised wave height and water depth, H/gT^2 and d/gT^2 respectively (DNV, 2013).

2.3. Navier-Stokes equation

A way to mathematically express the behaviour of flows is through the Navier-Stokes equations, which is named after the a French engineer and an English mathematician who both developed this equation independently of each other (Cengel and Cimbala, 2017). The Navier-Stokes equations can be derived from Newton's second law. Assuming incompressible flow with constant viscosity the Navier-Stokes equations are defined as:

$$\nabla \cdot \vec{V} = 0 \quad (2.5)$$

$$\rho \frac{D\vec{V}}{Dt} = -\vec{\nabla}P + \rho \vec{g} + \mu \nabla^2 \vec{V} \quad (2.6)$$

where \vec{V} , is the velocity vector; ρ , is the fluid density; t , represents the time; $\vec{\nabla}P$, is the pressure gradient; \vec{g} , is the vector of gravitational acceleration; and μ represents the dynamic viscosity.

Solving the Navier-Stokes equation analytically has so far proven impossible. It is an unsteady, non-linear, second-order, partial differential equation that has been subject of research for many years by many scientists. However, under specific assumptions and with help of numerical solvers, the Navier-Stokes equation can be used to obtain valuable results of flows.

Both computational fluid dynamics (CFD) models and potential flow theory models make use of the Navier-Stokes equations to obtain the velocity and pressure in a flow field. The main assumption of potential flow theory is that the vorticity within the flow is negligibly small. In other words: the flow is irrotational. Another important assumption in potential flow theory is the assumption that the fluid is inviscid. Both these assumptions simplify the Navier-Stokes equations to such extent that they can be solved analytically. On the other hand, CFD models are able to solve the Navier-Stokes equations numerically. However, this remains a challenging task. Specifically, for turbulent models. In order to check whether the output from CFD models makes sense, experiments are performed. Often, experimental results are used to obtain global properties of the flow, whereas CFD is used to obtain a more detailed picture of the flow field (Cengel and Cimbala, 2017). In the following the

basic principles of potential flow theory and the governing equations for the Navier Stokes solver are discussed.

2.4. Potential Flow Theory

Potential flow theory is based on the Navier-Stokes equation, however a number of assumptions are made in order to solve the Navier-Stokes equation analytically. In this section the governing equations for potential flow theory are discussed. Potential flow models are usually made up out of *building blocks*. The most widely used building blocks in potential flow models are also discussed in this section.

2.4.1. Governing Equations for Potential Flow Theory

Solving the Navier-Stokes equation (Equation 2.6) is analytically not feasible. However, under specific assumptions it is possible to obtain a solution for the Navier-Stokes equation. Firstly, it is assumed that the flow under consideration is incompressible. For most marine applications this is a fair assumption as the fluid being considered (sea water) has a very high resistance against compression (Fine and Millero, 1973). From the conservation of mass the incompressible continuity equation can be derived (Cengel and Cimbala, 2017):

$$\vec{\nabla} \cdot \vec{V} = 0 \quad (2.7)$$

Furthermore in potential flow theory only *irrotational* flows are considered. This is the main assumption of potential flow theory. It makes it possible to solve the Navier-Stokes equation for regions of potential flow. If a flow is irrotational, it means that its vorticity Ω is (approximately) zero:

$$\vec{\Omega} = \vec{\nabla} \times \vec{V} \cong 0 \quad (2.8)$$

The velocity vector \vec{V} used above can also be described as the gradient of the scalar ϕ : the velocity potential function. Mathematically, this yields:

$$\vec{V} = \vec{\nabla} \phi \quad (2.9)$$

Combining the Equation 2.9 and Equation 2.7 one can find a relation for the potential flow function for incompressible flows, often referred to as the *Laplace equation*:

$$\nabla^2 \phi = 0 \quad (2.10)$$

The Navier-Stokes equation (Equation 2.6) reduces to the following under the assumption of inviscid flow ($\mu = 0$) or using $(\vec{\nabla})^2 \vec{V} = 0$:

$$\rho \frac{\partial \vec{V}}{\partial t} = -\vec{\nabla} P + \rho \vec{g} \quad (2.11)$$

This equation is usually referred to as the *Euler equation*.

Also, the well-known Bernoulli equation (Equation 2.14) can be derived from the Navier-Stokes equations by substituting Equation 2.13 into Equation 2.6 and using the fact that if the gradient of a function is zero, the function itself should be a constant:

$$\rho \left[\frac{\partial \vec{V}}{\partial t} + (\vec{V} \cdot \nabla) \vec{V} \right] = -\nabla P + \rho \vec{g} \quad (2.12)$$

$$(\vec{V} \cdot \nabla) \vec{V} = \nabla \phi \cdot \nabla^2 \phi = \frac{1}{2} \nabla (\nabla \phi)^2 \quad (2.13)$$

$$\frac{P}{\rho} + \frac{V^2}{2} + gz = C = \text{constant everywhere} \quad (2.14)$$

Finally, apart from the potential velocity function ϕ it is useful to define another parameter: the stream function ψ (Lagrange, 1868). This function can be used to plot the trajectory of a particle in the flow and is for a 2-dimensional flow defined as:

$$u = \frac{\partial \psi}{\partial y} \quad v = -\frac{\partial \psi}{\partial x} \quad (2.15)$$

where u and v represent the velocity in x- and y-direction respectively.

2.4.2. Potential Flow Building Blocks

Due to the homogeneous and linear nature of the Laplace equation, it is possible apply the principle of superposition to it. In other words, the combination of two potential velocity functions can simply be described as the sum of the two functions: $\phi = \phi_1 + \phi_2$. Analogously, the principal of superposition can also be applied to the velocity ($\vec{V} = \vec{V}_1 + \vec{V}_2$) and the stream function ($\psi = \psi_1 + \psi_2$).

In fluid mechanics a number of elementary *building blocks* are developed. Thanks to the fact that superposition can be used for potential theory flows, a combination of those elementary building blocks can be used to describe a large variety of irrotational flows. Frequently used building blocks are for example (Cengel and Cimbala, 2017):

- uniform stream building block;
- line source or sink building block; and
- line vortex building block (also called circulation building block).

Each of those building blocks are illustrated in Figure 2.5.

2.4.3. Panel Method for Potential Flow Theory

For more complicated types of geometries, the sink-source method does not suffice the modelling needs. Instead, the panel method is used. For the results presented in Chapter 4 a software package is used that makes use of the panel method as well.

For application of the panel method, the wetted surface of the body is divided into a number of panels. At each of those panels the flow properties are assumed to be constant (Rivera-Arreba, 2017). Green's theorem (Lee and Newman, 1991) is used to obtain the radiation and diffraction velocity potentials on the boundary of the body.

In a 2D application of the panel method, the velocity \vec{V} at any point the the flow, is given by:

$$\vec{V} = \vec{U} + \vec{v} \quad (2.16)$$

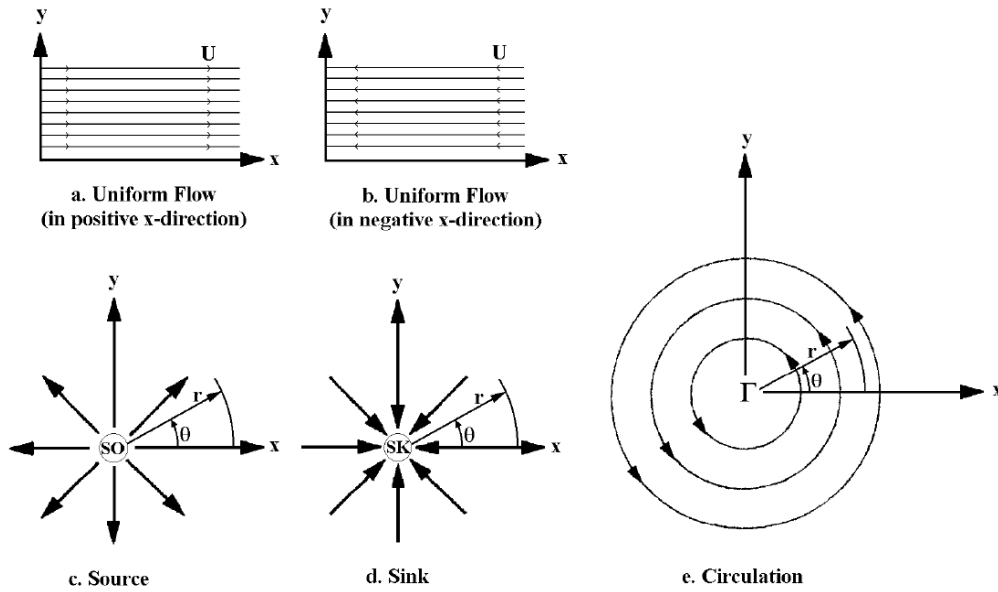


Figure 2.5: Potential flow building blocks (Journée and Massie, 2001).

where \vec{U} represents the uniform flow velocity at infinity and \vec{v} "is the disturbance field due to the body which is represented by two elementary flows corresponding to source and vortex flows." (Cebeci et al., 2005) On the center of each of the panels either a source or a vortex is placed. It is these source and vortex flows that \vec{v} is affected by. The disturbance field due to the presence of the body is then given as the integral of all induced source velocities \vec{v}_s and all vortex velocities \vec{v}_v over the body's surface (Cebeci et al., 2005):

$$\vec{v}(x, y) = \int \vec{v}_s q_j(s) ds_j + \int \vec{v}_v \tau_j(s) ds_j \quad (2.17)$$

where $q_j ds_j$, represents the the source strength for element ds_j on the j -th panel; and $\tau_j ds_j$ represents the vorticity strength for element ds_j on the j -th panel.

As described by Cebeci et al. (2005), no flow should go through the body surface, or analogously: it should be made sure that "the surface of the body is a streamline of the flow" (Cebeci et al., 2005). Mathematically these boundary conditions can be described as:

$$\psi = \text{constant} \quad \text{or} \quad \frac{\partial \phi}{\partial n} = 0 \quad (2.18)$$

where n , is the direction normal to the body's surface.

Also, other boundary conditions, like the boundary conditions at the boundaries of the flow, should be met. After discretisation of the problem, the potential flow can be resolved numerically.

2.5. Governing Equations Navier-Stokes Solver

All CFD calculations are based on three "fundamental physical principles" (Anderson et al., 2009):

1. mass is conserved;
2. Newton's second law ($F = m \cdot a$); and

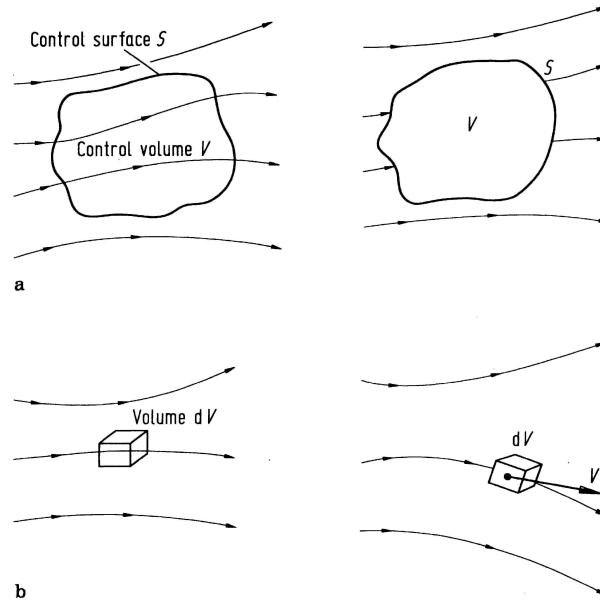


Figure 2.6: (a) Finite control volume approach. (b) Infinitesimal fluid element approach. Figures on the left indicate the conservative approach, whereas the figures on the right indicate the non-conservative approach with regards to the control volume moving in the fluid. (Anderson et al., 2009)

3. energy is conserved.

These physical principles can be elaborated on in mathematical form, which will lead to a set of three equations: which together constitute the Navier-Stokes equations. These three equations are, listed in the same order as the physical principals above on which they rely, listed below:

1. continuity equation;
2. momentum equation; and
3. energy equation.

These equations can be derived in two forms: the conservative and the non-conservative form. In the first form a control volume is used that does not move with the fluid, whereas in the second form the equations are derived based on a control volume that moves along with the flow. Another distinction that can be made in how the governing equations are derived, has to do with the size of the control volume. A finite control volume is a "reasonable large, finite region of the flow" (Anderson et al., 2009), in which flow physics is only applied to fluid inside the control volume or crossing the control volume surface. Alternatively, an infinitesimally small fluid element can be considered. Even though it is smaller than the finite control volume it is "large enough to contain a huge number of molecules so that it can be viewed as a continuous medium" (Anderson et al., 2009). Whereas in the case of a finite control volume the fluid flow equations are obtained in integral form (i.e. integrated around the finite control volume surface), the fluid flow equations derived with an infinitesimally small fluid element are directly in partial differential equation form. Figure 2.6 illustrates each of the control volume classifications previously discussed.

The momentum equation is derived from Newton's second law. This equation can, under the assumption of incompressible flow with constant viscosity, be expressed as:

$$\rho \frac{D\mathbf{u}}{Dt} = -\nabla P + \rho \mathbf{g} + \mu \nabla^2 \mathbf{u} \quad (2.19)$$

where \mathbf{u} , is the velocity vector; ρ , is the fluid density; t , represents the time; ∇P , is the pressure gradient; \mathbf{g} , is the vector of gravitational acceleration; μ represents the dynamic viscosity and $\nabla = (\partial_x, \partial_y, \partial_z)$ is the three-dimensional gradient operator.

The continuity equation follows from the principal that mass is conserved. For an infinitesimally small moving fluid element, the continuity equation in non-conservation form can be derived (Anderson et al., 2009):

$$\frac{D\rho}{Dt} + \rho \nabla \cdot \mathbf{u} = 0$$

which, under the assumption of constant density (incompressible flow), simplifies to:

$$\nabla \cdot \mathbf{u} = 0 \quad (2.20)$$

The energy equation is of less importance in the context of this thesis, since heat transfer is out of the scope of this work. Only relatively small temperature differences are assumed. Therefore, the author would like to refer to Anderson et al. (2009) for the derivation of the energy equation.

2.6. Heave Plates

An important aspect of the design of offshore floating wind turbines is limiting the the motions of the structure, because most components of the wind turbine, such as the drive train, can only withstand a limited amount of accelerations. Therefore, one particular concern with the DeepCwind floater is the heave motion. Heave plates are used in order to reduce the heave motion. These horizontal circular plates on the bottom of each floater column are supposed to increase damping due to vortex formation in the vertical direction (Thiagarajan Sharman et al., 2019). In addition to this, heave plates increase the added mass of the structure, increasing the natural period of the structure. However, capturing the effect of heave plates using numerical modelling tools is a challenging task. Floating structures subjected to large period waves can experience heave resonance: the structure is excited at its natural period. Under these circumstances, even small exciting forces can induce a large response of the system.

In industry, usually potential flow models are used to assess the response of floating structures. Viscous damping is usually empirically determined (Garrido-Mendoza, 2015). As a consequence, the exact response of a structure due to heave resonance is often hard to predict. Also for the DeepCwind floater it has been recommended to investigate the effects of heave plates under heave resonance conditions on a more detailed level (Rivera-Arreba, 2017).

As stated by Haslum and Faltinsen (1999) there are three ways to reduce the response of the system:

1. increasing the damping of the system;
2. increasing the natural heave period of the system, such that it is out of the range of the wave energy; and
3. reducing the heave excitation forces.

By changing the heave plate geometry all of the aforementioned parameters are affected to some extent. Clearly, the added mass and damping are affected by heave plates. Changes in added mass and damping indirectly induce changes in the natural heave period of the system. However, also the excitation forces are affected due to changes in the submerged part of the geometry of the structure. In the following section, the influence of heave plates on added mass, damping and the natural heave period of the system are discussed.

2.7. Damping and Added Mass of Heave Plates

Damping on floating structures is usually categorized into two types of damping: viscous damping (also referred to as hydrodynamic damping) and radiation damping (Sarpkaya, 2010). Viscous damping is the process where energy from an oscillatory movement is dissipated through processes such as flow separation and the creation of vortices (Steidel, 1989). The fluid near the wall of the structure consists of a very thin boundary layer in which skin friction, normal pressure and boundary layer instabilities cause forces in anti-phase with the velocity of the structure (Sarpkaya, 2010). As a result viscous damping can be observed as a decrease of the amplitude of oscillation from cycle to cycle. On the other hand, damping can occur due to radiation damping of a structure. Radiation damping is the result from energy that propagates away from the structure by motion-induced waves (Dunwoody and Vandiver, 1987).

Like the damping, also *added mass* is initiated due to disturbances of a moving body in a fluid. These disturbances induce a hydrodynamic pressure, which after integration over the body surface gives forces which are mathematically represented as added mass. Sarpkaya (2010) prefers to refer to added mass with the term *added inertia*, since the term added mass implies that the "mass of a solid body has literally increased by some miraculous means".

2.8. Simplified Analytical Solution for Wave Structure Interaction Analysis

The flow around heave plates is typically turbulent. The damping is highly influenced by flow separation, as described by Molin (2001): "the flow separates at the edge, inducing drag forces and energy dissipation." A visualisation of flow separation at the edge of a heave plate is provided in Figure 2.8. Due to the turbulent flow characteristics for heave plates, finding the added mass, damping and system response on floating structures with heave plates, is a challenging task, which often involves advanced computational models such as OpenFOAM. Nevertheless, simplified analytical solutions can be of great value in order to obtain more insight into the basic wave structure interaction. Therefore, this section discusses a highly simplified analytical solution for the wave structure interaction of a vertical floating cylinder, as depicted in Figure 2.7.

When the system from Figure 2.7 is assumed to be linear, the principal of superposition can be applied. This means the response of the floating body can be described by the summation of (Journée and Massie, 2001):

- the hydromechanical forces F_h , induced by the harmonic oscillations of the rigid body in still water; and
- the wave excitation forces F_w , produced by the incoming waves on the restrained body.

Note that in order for these assumptions to remain valid, linear wave theory is used and potential flow theory is assumed to accurately describe the flow. Furthermore, the amplitude of the oscillations and the diameter of the body with respect to the wave length are assumed to be small.

The equation of motion describing the response of the structure from Figure 2.7 is then, using Newton's second law, defined as:

$$\frac{d}{dt}(m \cdot \dot{z}) = m \cdot \ddot{z} = F_h + F_w \quad (2.21)$$

where t , is the time; z , is the location of the body in heave direction; and m , refers to the mass of the structure.

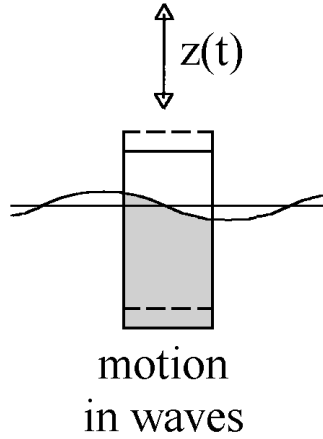


Figure 2.7: Schematic overview of a vertical floating cylinder such as discussed in this section (Journée and Massie, 2001).

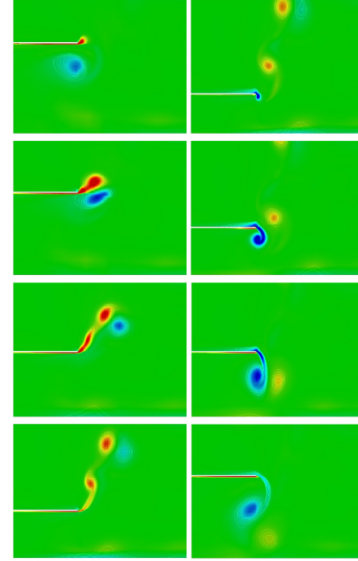


Figure 2.8: Visualisation of the flow separation around the edge of a heave plate (Garrido-Mendoza et al., 2014). The colors indicate the vorticity of the flow (scale varies from 100[1/s] (blue) to 100[1/s] (red)).

The hydromechanical forces on the body F_h can then be described as:

$$F_h = -a\ddot{z} - b\dot{z} - cz \quad (2.22)$$

where, a , is the added mass of the body; b , is the hydrodynamic damping coefficient; and c , is the restoring spring coefficient, which can be determined based on the water plane area A_w : $c = \rho g A_w$.

By using a numerical model or performing experiments the hydrodynamic damping and added mass can be obtained. Assuming the added mass and damping coefficients are known, the equation of motion, Equation 2.21, becomes:

$$(m + a)\ddot{z} + b\dot{z} + cz = F_w \quad (2.23)$$

The vertical wave loads on the restrained cylinder, F_w , can be calculated based on the wave potential and wave elevation for deep water waves as (by using Airy wave theory):

$$\begin{aligned} \text{wave potential:} \quad \phi &= \frac{\zeta_a g}{\omega} e^{kz} \sin(\omega t - kx) \\ \text{wave elevation:} \quad \zeta &= \zeta_a \cos(\omega t - kx) \end{aligned} \quad (2.24)$$

where x , represents the direction in which the waves travel; ζ , is the wave elevation; and ζ_a is the wave amplitude.

The vertical load on the cylinder from Figure 2.7 is given by the water pressure on the bottom of the cylinder. Using the Bernoulli equation for potential flow, one can obtain the pressure at the bottom of the cylinder by substituting Equation 2.24:

$$\begin{aligned}
p &= -\rho \frac{\partial \Phi}{\partial t} - \rho g z \\
&= \rho g \zeta_a e^{kz} \cos(\omega t - kx) - \rho g z \\
&= \rho g \zeta_a e^{-kT} \cos(\omega t - kx) + \rho g T
\end{aligned} \tag{2.25}$$

$$\text{for small diameter } (kD \approx 0): \quad \approx \rho g \zeta_a e^{-kT} \cos(\omega t) + \rho g T$$

where T , is the draft of the cylinder. Also, note that the linearized form of the Bernoulli equation has been used here, meaning that higher order terms of the velocity potential are assumed to be zero, $|\nabla\phi|^2 = 0$.

The hydrostatic part of the force, $\rho g T$, drops against the gravity of the structure mg . For this reason, usually only the harmonic part of pressure is considered. Under the assumption that the pressure is equal across the cylinder's bottom surface, the vertical force becomes:

$$F_{FK} = \rho g \zeta_a e^{-kT} \cos(\omega t) \cdot \frac{\pi}{4} D^2 \tag{2.26}$$

This force, which results from integrating the pressure over the surface of the body in an undisturbed wave, is referred to as the Froude-Krilov force F_{FK} . It is also commonly written as a function of

- the restoring spring coefficient $c = \rho g \frac{\pi}{4} D^2$, where D is the cylinder diameter; and
- the reduced (or effective) wave elevation $\zeta^* = \zeta_a e^{-kT} \cos(\omega t)$:

$$F_{FK} = c \cdot \zeta^* \tag{2.27}$$

The total wave force on a floating structure consists of both a viscous and a non-viscous part. In potential flow theory - and in this section - the viscous part of the wave force is neglected. The non-viscous part of the wave force consists of two parts. The Froude-Krylov force is derived under the assumption that that the body is sufficiently small not to affect the pressure field of the incident wave. However, in reality the pressure field is affected by the structure. This effect - the disturbance of the wave field by the structure - is referred to as wave diffraction. A second part therefore needs to be added to the total wave force.

In order to take into account the wave diffraction, two terms are added to the wave force equation: $a\ddot{\zeta}^*$ and $b\dot{\zeta}^*$, which are proportional to the vertical accelerations and the vertical velocities of the wave particles respectively. Thus, the total wave force becomes:

$$\begin{aligned}
F_w &= a\ddot{\zeta}^* + b\dot{\zeta}^* + c\zeta^* \\
&= \zeta_a e^{-kT} (c - a\omega^2) \cos(\omega t) - \zeta_a e^{-kT} b\omega \sin(\omega t)
\end{aligned} \tag{2.28}$$

Substituting the wave force F_w into the equation of motion (Equation 2.23) gives:

$$(m + a)\ddot{z} + b\dot{z} + cz = a\ddot{\zeta}^* + b\dot{\zeta}^* + c\zeta^* \tag{2.29}$$

The heave response of the cylinder to regular wave excitation can be expressed as a harmonic oscillation with a phase difference $\epsilon_{z\zeta}$ with respect to the surface elevation:

$$\begin{aligned}
z &= z_a \cos(\omega t + \epsilon_{z\zeta}) \\
\dot{z} &= -z_a \omega \sin(\omega t + \epsilon_{z\zeta}) \\
\ddot{z} &= -z_a \omega^2 \cos(\omega t + \epsilon_{z\zeta})
\end{aligned} \tag{2.30}$$

Substituting this along in the equation of motion gives:

$$\begin{aligned} & z_a(c - (m + a)\omega^2) \cos(\omega t + \varepsilon_{z\zeta}) - z_a b\omega \sin(\omega t + \varepsilon_{z\zeta}) = \\ & = \zeta_a e^{-kT} (c - a\omega^2) \cos(\omega t) - \zeta_a e^{-kT} b\omega \sin(\omega t) \end{aligned} \quad (2.31)$$

By splitting the in-phase and out-of-phase (cosine and sine) parts of this equation and rewriting, one can find the

In order to obtain a more in-depth understanding of the influence of the damping on the reponse of floating structures, the RAO for a simple floating cylinder is examined. The RAO can mathematically be defined as:

$$\text{RAO}(\omega) = \frac{z_a}{\zeta_a} \quad (2.32a)$$

by splitting the in phase and out-of-phase (cosine and sine) parts of Equation 2.31 and rewriting, one can find that the RAO for a cylinder can be expressed as:

$$\text{RAO}(\omega) = e^{-kT} \sqrt{\frac{\{c - a\omega^2\}^2 + \{b\omega\}^2}{\{c - (m + a)\omega^2\}^2 + \{b\omega\}^2}} \quad (2.32b)$$

where z_a , is the amplitude of the response of the structure in heave direction; and ζ_a , is the amplitude of the wave elevation.

Furthermore, the phase shift of the heave response with respect to the surface elevation, which is referred to as the phase characteristic, can be obtained from Equation 2.31:

$$\varepsilon_{z\zeta} = \arctan \left\{ \frac{-mb\omega^3}{(c - a\omega^2) \{c - (m + a)\omega^2\} + \{b\omega\}^2} \right\} \quad \text{with } : 0 \leq \varepsilon_{z\zeta} \leq 2\pi \quad (2.33)$$

It is important to realize that in practice the added mass a , damping b and the restoring spring coefficient c are also dependent of wave frequency ω . Furthermore, potential flow theory, which was used for this analysis, assumes no vorticity in the flow. Consequently, the damping is likely to be underestimated for relatively large motion amplitudes. Especially around the natural frequency of the structure, where the amplitudes are usually relatively high, this leads to unrealistic values of the RAO.

2.9. Simplified Solution for Cylinder with Heave Plate and Cancellation Frequency

The equation of motion, RAO and phase characteristics from Section 2.8 are derived for a cylinder without any appendages. This report, however, looks into the effects of heave plates. Therefore, this section analyses a simplified analytical solution for a cylinder with heave plate. Also, the so-called cancellation frequency is obtained.

Equation 2.25 gives the pressure p based on linear potential flow deep water waves at the bottom of a cylinder with draft T , recall:

$$p \approx \rho g \zeta_a e^{-kT} \cos(\omega t) + \rho g T \quad (2.34)$$

Integrating the hydrodynamic part of the pressure over the surface of the top and bottom of the heave plate, gives the vertical wave force exerted on a cylinder with heave plate:

$$F_{FK} = \rho g \zeta_a \cos(\omega t) A_{hp} e^{kz_B} - \rho g \zeta_a \cos(\omega t) (A_{hp} - A_{col}) e^{kz_T} \quad (2.35)$$

where A_{hp} , is surface area of the heave plate; A_{col} , is the surface area of the column; z_T , is the height in z -direction of the top of the heave plate; and z_B , is the height in z -direction of the bottom of the heave plate.

This can be rewritten in terms of the z -coordinate of the middle of the heave plate z_m , using the heave plate height h :

$$F_{FK} = \rho g \zeta_a \cos(\omega t) A_{hp} \left[e^{k(z_m - \frac{h}{2})} - e^{k(z_m + \frac{h}{2})} \right] + \rho g \zeta_a \cos(\omega t) A_{col} e^{k(z_m + \frac{h}{2})}$$

Since $kh \ll 1$, the term e^{kh} can be rewritten, using the Taylor expansion, as $1 + kh$:

$$\begin{aligned} F_{FK} &= \rho g \zeta_a \cos(\omega t) A_{hp} \left[1 - \frac{kh}{2} e^{kz_m} - \left(1 + \frac{kh}{2} e^{kz_m}\right) \right] + \rho g \zeta_a \cos(\omega t) A_{col} e^{kz_m} \left(1 + \frac{kh}{2}\right) \\ &= \rho g \zeta_a \cos(\omega t) A_{hp} (-kh) e^{kz_m} + \rho g \zeta_a \cos(\omega t) A_{col} e^{kz_m} \left(1 + \frac{kh}{2}\right) \end{aligned}$$

As deep water is assumed, the deep water dispersion relation can be used: $\omega^2 = gk$, which gives:

$$F_{FK} = \rho \zeta_a \cos(\omega t) e^{kz_m} \left[g A_{col} + \frac{h}{2} A_{col} \omega^2 - h A_{hp} \omega^2 \right]$$

Using the fact that $h = z_T - z_m$ and the fact that the mass of the total mass of the structure is given by the mass of its submerged volume, this can finally be written as:

$$F_{FK} = \zeta_a \cos(\omega t) e^{kz_m} \left[-m\omega^2 + \rho g A_{col} - \omega^2 z_m \rho A_{col} \right] \quad (2.36)$$

The total wave excitation force is given by the Equation 2.28. Since the damping $b = 0$ at the cancellation frequency (no waves are radiated at the cancellation frequency), the total wave excitation force becomes:

$$F_w = \zeta_a \cos(\omega t) e^{kz_m} \left[-(m + a)\omega^2 + \rho g A_{col} - \omega^2 z_m \rho A_{col} \right] \quad (2.37)$$

The cancellation frequency can now be obtained by finding where $F_w = 0$, which comes down to setting the part within the square brackets equal to zero. Using the natural frequency for an undamped system,

$$\omega_n^2 = \frac{c}{m + a} = \frac{\rho g A_{col}}{m + a}, \quad (2.38)$$

the cancellation frequency ω_c is found as:

$$\omega_c = \sqrt{\frac{g}{z_m + \frac{g}{\omega_n^2}}} \quad (2.39)$$

Note that z_m , indicating the middle of the heave plate in z -direction, is a negative number as the z -coordinate is defined starting at the water surface. Furthermore, it can be seen that for any case the cancellation frequency $\omega_c > \omega_n$.

At the wave cancellation frequency, the hydrodynamic part of the wave force is such, that the heave force on the top and bottom of the heave plate are exactly equal and opposite in direction. The

surface area of the bottom of the heave plate is larger than the top of the heave plate (where part of the surface is covered up with the column), whereas the hydrodynamic pressure on the top heave plate is larger than at the bottom. Consequently, the wave excitation force is zero at the cancellation frequency. Also, the radiation damping decreases to zero, as the ability of the structure to generate waves is cancelled out. Note that in practice, the viscous damping, which is not included in potential flow theory, will remain and will start dominating the damping and wave excitation forces.

2.10. Decay Test

In order to obtain more insight into the natural frequency of the structure and the damping a heave decay test has been carried out, the results of which are discussed in Chapter 5. This section describes the method that was used to obtain the damping coefficients. Two methods have been used to quantify the damping and both methods are briefly discussed in this section.

The first method that can be used in order to quantify the damping at the (damped) natural frequency uses only a linear damping coefficient κ (Journée and Massie, 2001). This method is based on the equation of motion Equation 2.23, where the wave force $F_w = 0$ since the decay test is carried out in still water. The equation of motion is then rewritten as:

$$\ddot{z} + 2\kappa\omega_0 \cdot \dot{z} + \omega_0^2 \cdot z = 0 \quad (2.40)$$

where ω_0 , is the undamped natural frequency in z -direction; and κ , is the non-dimensional damping coefficient, defined as a ratio between the damping coefficient b and critical damping $b_{cr} = 2\sqrt{(m+a) \cdot c}$.

Since the system is assumed to be lightly damped, the undamped natural frequency ω_0 is assumed to be equal to the damped natural frequency: $\omega_z \approx \omega_0$.

The solution of the equation of motion from Equation 2.40 with initial displacement z_0 is described as:

$$z = z_a e^{-\kappa\omega_0 t} (\cos \omega_0 t + \kappa \sin \omega_0 t) \quad (2.41)$$

The $z_a e^{-\kappa\omega_0 t}$ term describes the decrease of the motion amplitude. Using the values of the peaks of the heave decay time series, values for the damping coefficient κ and motion amplitude z_a are obtained based on a least square estimation.

Another way to quantify the damping based on a (heave) decay test is by the use of the linear and quadratic damping coefficients, b_1 and b_2 respectively. As explained by Roberts (1985), who first presented this method, this method is based on the following equation of motion:

$$\ddot{z} + b_1 \dot{z} + b_2 |\dot{\eta}| \dot{z} + \omega_0^2 z = 0 \quad (2.42)$$

Also in this case the undamped natural frequency ω_0 is assumed to be equal to the damped natural frequency. The energy per mass of the system at any given time can then be written as:

$$V(t) = \frac{1}{2} \dot{z}^2 + \frac{1}{2} \omega_0^2 z^2 \quad (2.43)$$

The linear and quadratic damping coefficients are then calculated based on the loss of energy over each cycle $L(V)$, which can be calculated based on the time derivative of the energy $V(t)$:

$$L(V) = -\frac{d}{dt} V(t), \quad (2.44)$$

which can finally be rewritten as:

$$L(V) = b_1 V + b_2 \frac{8}{3} 2\sqrt{2} V^{3/2}. \quad (2.45)$$

At the peaks and troughs of z at time t_n the velocity $\dot{z} = 0$. Therefore, V can easily be calculated from the peak and trough values z_n using:

$$V(t_n) = \frac{1}{2} \omega_0^2 z_n^2 \quad (2.46)$$

The linear and quadratic damping coefficients b_1 and b_2 are then obtained by applying a least-square fit that matches the decay dV/dt .

3

Numerical Tools

Several approaches exist that can be used to assess loads on structures in a flow. An important distinction between methods to assess loads on structures can be made between theoretical models on one hand and experimental methods on the other hand. However, it should be noticed that in practice both methods go hand in hand. Experiments are used to verify theoretical models, whereas theoretical models are used to reduce the amount and complexity of required experiments.

The Navier-Stokes equation is the theoretical basis for all theoretical models. Solving this equation analytically is generally not possible as it is an unsteady, non-linear, second-order, partial differential equation. However, under specific assumptions the Navier-Stokes equation can be reduced in complexity and can be evaluated analytically as explained in Section 2.4. This method is referred to as potential flow theory. Throughout this work the potential flow based software package WAMIT (Wamit Inc., 2006) has been used to evaluate the loads on the column with(out) heave plate. This tool is described in Section 3.2.

Furthermore, the loads on the structure have been assessed using a tool which solves the Navier-Stokes equation numerically. This technique is usually referred to as Computational Fluid Dynamics (CFD). The CFD software package used throughout this work is OpenFOAM®. More specifically, the interDyMFoam solver coupled to the waveFoam solver from the waves2Foam toolbox has been used. This solver is referred to as the waveDyMFoam solver. In Section 3.1 the working principles of CFD are elaborated on. The governing equations are discussed in Section 2.5.

3.1. Navier Stokes Solver

This section elaborates on the basic working principles of some important features of the waveDyMFoam solver, which is a coupling of the standard OpenFOAM interDyMFoam solver and the waveFoam solver from the waves2Foam toolbox. The set-up of the numerical wave tank in OpenFOAM was largely based on work by Bruinsma (2016) and Rivera-Arreba (2017) as they performed similar simulations.

3.1.1. WaveDyMFoam Solver

The waveDyMFoam solver, which is used throughout this work, can work with two different fluids, in this case air and water. The fluids are assumed to be isothermal, incompressible and immiscible. As a consequence, the density ρ and the dynamic viscosity μ are constant for water and air. Consequently, the continuity equation and the momentum equation (Navier-Stokes equation) solved by

the `waveDyMFoam` solver, are used in the previously mentioned forms (Equation 2.20 and Equation 2.19).

The spatial domain is divided into small 3D volumetric cells. Within each cell the VOF (volume of fluid) phase-fraction based interface capturing approach, developed by Hirt and Nichols (1981), is used to take into account the volumetric fraction of water and air in each cell. The scalar $\alpha \in [0, 1]$ is used to represent the fraction of air ($\alpha = 0$) and water ($\alpha = 1$). Thus, the *local* pressure and dynamic viscosity can be obtained using the volume fraction parameter α :

$$\begin{aligned}\rho &= \alpha\rho_w + \rho_a(1 - \alpha) \\ \mu &= \alpha\mu_w + \mu_a(1 - \alpha)\end{aligned}\tag{3.1}$$

As described in Rusche (2002) the VOF method is used to advance the α field in time. In order to reduce smearing of the interface over a large area, an interface compression term is used, as discussed by Berberović et al. (2009). This leads to the following equation, where the last term on the left hand side is used to reduce the smearing effect of the water-air interface:

$$\frac{\partial\alpha}{\partial t} + \nabla \cdot \mathbf{u}\alpha + \nabla \cdot \mathbf{u}_r\alpha(1 - \alpha) = 0\tag{3.2}$$

3.1.2. Discretisation

In order to solve the governing equations numerically, the hydrodynamic problem is discretised. Both spatial discretisation and temporal discretisation have been used.

Throughout this work the discretisation of the spatial domain is performed using the finite volume method in OpenFOAM. Using this technique the flow domain is subdivided into small contiguous cells of finite volume (control-volumes). The local and global mass conservation can be implemented in a straight-forward manner with this method. Also, boundary conditions can more easily be taken into account, in comparison to other discretisation techniques.

Apart from discretisation of the flow domain, numerical approximations for the differential terms in the momentum and continuity equation shall be found. Throughout this work the same discretisation schemes as used in Bruinsma (2016) are applied, since tests with these schemes have shown good results in related studies by Bruinsma (2016) and Rivera-Arreba (2017). All discretisation schemes can be found in Table 3.1. However, the author wants to draw special attention to the discretisation schemes used for the advective term ($\mathbf{u} \cdot \nabla$) of the continuity and momentum equation. Using Gauss's theorem the volume integral can be rewritten as a surface integral. Then the question remains which discretisation scheme should be used to obtain the values at the control-volume surface. Bruinsma (2016) tested both a first-order Upwind and a second-order MUSCL scheme. The latter indicated an unsteady convergence rate, which led to the choice of using the first-order Upwind scheme.

3.1.3. Pressure Velocity Coupling

The continuity equation and the momentum equation are coupled in OpenFOAM using the PIMPLE algorithm. This algorithm is a combination of both the PISO (Pressure-Implicit with Splitting of Operators) and the SIMPLE (Semi-Implicit Method for Pressure Linked Equations) algorithm. The PIMPLE algorithm searches for a steady-state solution of the governing equations in every time step. This is an iterative process, where the maximum number of times that the equations are solved before moving on to the next time step is specified by the number of Outer Correctors. Throughout this work the number of Outer Correctors has been slightly varied between three and six, depending on whether issues with convergence arose.

	Term	Discretisation
Spatial domain		Finite Volume (FV) Method
Temporal derivative	$(\nabla \mathbf{u}, \nabla \alpha)$	Euler. Second-order
Gradient	$\nabla \cdot (\rho \phi \mathbf{u})$	Gauss linear. First-order
Divergence	$\nabla \cdot (\phi \alpha)$	Gauss upwind. First-order
	$\nabla \cdot (\rho \phi_{rb} \alpha)$	Gauss upwind. First-order
	∇^2	Gauss interface compression. First-order
Laplacian	$\frac{d}{dt}$	Gauss linear corrected. First-order

Table 3.1: Numerical discretization schemes used throughout this work.

Another possibility for this iterative process to continue to the next time step - apart from reaching the maximum number of iterations - is when the solution of the governing equations has sufficiently converged. This is measured based on the *residuals*. When the calculated solution is substituted into the governing equations, the magnitude of the difference between the left and the right hand side indicates the residual. The smaller the residual, the better the solution has converged. In other words, if the system of equations to be solved is:

$$A\mathbf{x} = \mathbf{b},$$

then the residual is defined as:

$$\mathbf{r} = \mathbf{b} - A\mathbf{x}$$

Furthermore, the residual can be normalized using the normalization parameter n , which is based on the average of the solution vector $\bar{\mathbf{x}}$:

$$n = \sum (|A\mathbf{x} - A\bar{\mathbf{x}}| + |\mathbf{b} - A\bar{\mathbf{x}}|), \quad (3.3)$$

the normalized residual then becomes:

$$r = \frac{1}{n} \sum |\mathbf{b} - A\mathbf{x}|. \quad (3.4)$$

Furthermore, an under-relaxation strategy is used for the calculation of the pressure field. This implies that the pressure is corrected a number of times within one time-step iteration. These iterations are referred to as the Inner Correctors. The under-relaxation factor f_p determines the extent to which the under-relaxation strategy is applied, according to the following equation:

$$p_i^* = f_p p_i + (1 - f_p) p_{i-1}^* \quad (3.5)$$

where p_i^* , is the under-relaxed pressure in the new inner corrector iteration; p_i , is the calculated pressure in the new inner corrector iteration; and p_{i-1}^* , is the under-relaxed pressure of the previous inner corrector iteration. Note that for the final inner corrector loop a corrector factor $f_p = 1$ is used (which implies no relaxation), whereas for other iterations the value $f_p = 0.5$ was used. Throughout this work the number of Inner Correctors was set to three.

For a more detailed and in-depth explanation of the PIMPLE algorithm, the author refers to other literature, such as Holzmann (2019) and Ferziger and Perić (2002). For the the exact settings of the PIMPLE algorithm, such as the residual control, that have been used, the author refers to Appendix B.

3.1.4. Relaxation Zone and Boundary Conditions

The wavesDyMFoam solver makes use of the so-called *relaxation zones*. These are areas within the flow domain where the waves are generated or dampened out in order to remove spurious reflection from numerical simulations. This technique is based on a target solution and the computed solution of the velocity field (Jacobsen, 2017). Using a weighting between these two solutions, the actual solution for the flow field is obtained. Each time step the values of volume fraction parameter α and the velocity field \mathbf{u} are adjusted accordingly. Relaxation zones can make use of either explicit or implicit time integration. Throughout this work the explicit method is used. The solution is then given by the following equation (Jacobsen, 2017, Jacobsen et al., 2012):

$$\phi = (1 - w_R) \phi_{\text{target}} + w_R \phi_{\text{computed}} \quad (3.6)$$

where $w_R \in [0, 1]$, is the weighting function; ϕ_{target} , represents the pre-defined target solution; and ϕ_{computed} , represents the computed solution of the velocity field.

The waves2Foam toolbox offers a number of available weighting functions w_R . Throughout this work the exponential weight distribution, developed by Fuhrman et al. (2006), is used:

$$w_R = 1 - \frac{\exp \sigma^\beta - 1}{\exp 1 - 1} \quad (3.7)$$

where $\sigma \in [0, 1]$, is the local coordinate within the relaxation zone such that $w_R(\sigma = 1) = 0$ and $w_R(\sigma = 0) = 1$; and β , is the shape parameter, which is set to its default value of $\beta = 3.5$ (Jacobsen, 2017).

A schematic overview of the flow domain is depicted in Figure 3.1. The relaxation zones are referred to as *inlet* and *outlet*. In the inlet the waves are generated according to the stream function wave theory described by Fenton (1988) and Rienecker and Fenton (1981) (see Section 2.2). Within the outlet relaxation zone the target solution is set to a current of zero velocity that is constant over depth (referred to as potentialCurrent type waves) in order to dampen out the waves.

To all outer boundaries of the fluid domain boundary conditions have been applied for the phase fraction parameter α , the velocity field \mathbf{u} and the pressure (excluding the hydrostatic pressure) p_{rgh} . All boundary conditions are listed in Table 3.2.

3.1.5. Motion of the Structure (Fluid Structure Interaction)

The flow around the structure to be studied has been assessed in three different ways:

1. the structure has a fixed position;

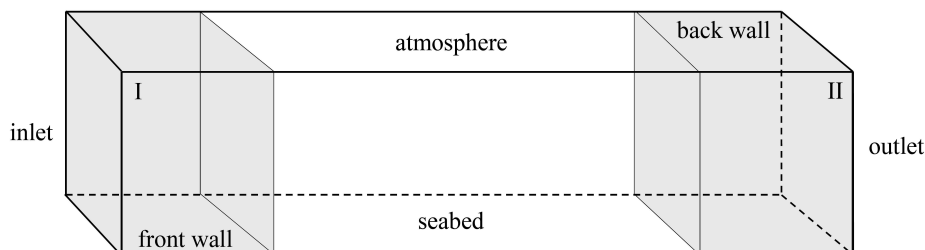


Figure 3.1: A schematic overview of the flow domain indicating the relaxation zones (inlet and outlet) and the boundary surfaces. (Bruinsma, 2016)

	phase fraction α	velocity U	pressure p_{rgh}
atmosphere	outflow of water and air possible, return flow can only be air	velocity matches pressure boundary condition, in and outflow is possible	total pressure is constant, static pressure is computed
seabed	zero gradient*	slip	zero gradient*
front wall	zero gradient*	slip	zero gradient*
back wall	zero gradient*	slip	zero gradient*
inlet	zero gradient*	zero gradient*	zero gradient*
outlet	zero gradient*	zero gradient*	zero gradient*
structure	zero gradient*	no flux through the moving structure	pressure is set such that the flux meets the velocity boundary condition

Table 3.2: An overview of the boundary conditions for the patches depicted in Figure 3.1. *Zero gradient means that the patch value is extrapolated to the nearest cell value.

2. a predefined motion is imposed on the structure; and
3. the structure can freely move in one or more directions.

In the latter two cases the mesh deforms along with the moving structure. All cells within a certain distance from the structure deform slightly in order to move the structure to the wanted position. Whereas the predefined motion works relatively straight-forward, the motion becomes more complicated when the structure can move freely as at this point the fluid starts to interact with the movement of the structure. Throughout this work the `sixDoFRigidBodyMotion` solver has been used to determine the movement of the freely moving structure. It should be noted that the structure is assumed to be completely rigid in all cases. In the following the main working principles of the `sixDoFRigidBodyMotion` solver are elaborated on.

The movement of the structure can be affected by a number of circumstances:

- action of the fluid;
- external forces (e.g. gravity force or restraints such as mooring lines);
- constraints to the movement; and
- structural properties of the body (mass, moment of inertia).

The fluid forces on the body can be categorized into two groups: loads due to the pressure integrated over the body's surface and viscous forces. The fluid forces \mathbf{F}_k and moments \mathbf{M}_k due to the pressure are obtained by integrating the pressure p over the body's outer surface S_{oB} :

$$\begin{bmatrix} \mathbf{F}_k \\ \mathbf{M}_k \end{bmatrix} = \int_{S_{oB}} p \begin{bmatrix} \mathbf{n} \\ \mathbf{r} \times \mathbf{n} \end{bmatrix} dS_{oB}, \quad (3.8)$$

where \mathbf{n} , represents the surface normal; and \mathbf{r} , is the distance from the infinitesimal fluid force to the body's centre of mass.

Throughout this work the Newmark-beta solver has been used to solve the fluid-structure interaction problem (Newmark, 1959). The implicit form of this second order method has been applied

using the average constant acceleration (mid point rule) assumption, for which the default values for the velocity and position integration coefficients, $\gamma = 0.5$ and $\beta = 0.25$ respectively, are used.

Furthermore, in some cases the *under-relaxation method* can be used in order to counteract stability issues. The under-relaxation method, which was presented by Ferziger and Perić (2002), adjusts the acceleration of the body's center of mass with a factor f_a : the *acceleration relaxation* factor. The 'relaxed' acceleration a_i^* of the body at time step i is then computed based on the calculated acceleration a_i as:

$$a_i^* = f_a a_i + (1 - f_a) a_{i-1}^* \quad (3.9)$$

where a_{i-1}^* , represents the 'relaxed' acceleration at the previous time step.

It should be noted that this method can give unrealistic results for small factors f_a as it directly adjusts the acceleration. Divergence might occur if there is too much discrepancy with the calculated fluid forces and the resulting motion of the body. Therefore, for the final work that is presented in this report an acceleration factor of $f_a = 1$ has been used.

3.1.6. Mesh Generation

The mesh in OpenFOAM was generated using the blockMesh utility in order to create a so-called background mesh. The simpleGrading technique was used to refine the mesh around the water surface. In the case for the longest wave ($T = 17.4$ s, see Chapter 5) this utility was also used in the horizontal x -direction.

After generating the background mesh with the blockMesh utility, the snappyHexMesh tool was used in order to 'cut out' the geometry of the column from the background mesh. Close to the structure, the cell size was refined up to level three, which means that the cell length is $2^3 = 8$ times as small as the regular background cells. The snappyHexMesh settings were chosen in accordance the work from Rivera-Arreba (2017) and Bruinsma (2016).

3.1.7. Force and Wave Gauge Functions

Throughout this work the OpenFOAM 'forces' function has been used in order to extract the loads exerted by the fluid on the structure. As discussed in Section 3.1.5 the fluid exerts forces on the structure either through pressure (Equation 3.8) or viscous forces. The OpenFOAM algorithm calculates both of these forces separately. The viscous forces F_v are obtained by means of Equation 3.10:

$$\mathbf{F}_v = \int_{S_{oB}} \mu \mathbf{R}_{dev} dS_{oB}, \quad (3.10)$$

where S_{oB} , represents the body's outer surface; μ , is the dynamic viscosity; and \mathbf{R}_{dev} is the deviatoric stress tensor. This force acts tangential to the body's surface. A more in-depth explanation on how the forces are calculated is provided in Holzmann (2019).

Note that in the CFD model used in this work the pressure is also affected by the viscosity of the fluid, whereas in potential flow theory the fluids are assumed to be completely inviscid. In practice, this means that even though the viscous forces might be low, the total viscous effects of the flow on the fluid forces can be much higher.

Another function that has been used throughout this work is the so-called 'waveGauges' function, which is part of the waves2Foam toolbox. Using this function, wave gauges can be placed at various points in the domain. The output of these wave gauges gives a time series of the surface elevation at the specified location. The surface elevation is based on the volumetric water fraction α and is

calculated based on the following equation:

$$\eta = \int_{z_0}^{z_1} \alpha dz - d \quad (3.11)$$

where z_0 and z_1 , define the top and bottom of the wave gauge in the vertical direction; d , is the initial still water position; and η , is the surface elevation.

3.2. Potential Flow Model: WAMIT

The potential flow model that has been used in this work is the software package WAMIT (Wamit Inc., 2006). WAMIT makes use of the panel method, discussed in Section 2.4.3. A mesh of the structure was made with Genie and converted to the right format using HydroD (DNV Software SESAM, 2013). Through numerical integration of the radiation pressure around the wetted surface of the column, WAMIT calculates the added mass and damping of the structure for a number of wave periods.

In the context of the Offshore Code Comparison Collaboration Continuation (OC4) project the added mass and hydrodynamic damping of the full DeepCwind floater have been calculated with WAMIT as well. The mesh resolution used in this report has been verified by running simulations of the full deepCwind floater. The two data sets were practically identical, which is an indication that the WAMIT model has been used correctly. Since the focus of this report is on the heave plates of a single column, the results presented in Chapter 5 are all based on a single column with and without heave plate.

WAMIT evaluates the unsteady hydrodynamic pressure on the body, loads and motions of the body. Also, the induced pressure and velocity in the fluid domain are evaluated. Furthermore, linearization of the free-surface and body-boundary conditions is applied Lee (1995). Within WAMIT, first the linear problem for a specific incident wave is solved. Then, the rigid body motions and hydrodynamic forces are derived using the perturbation method. It is important to note that due to the potential flow assumptions, neither separation nor lifting effects are taken into account.

4

Potential Flow Results

The potential flow model WAMIT was used in order to obtain insight into the RAO, damping, added mass and wave excitation forces on the DeepCwind-like column with and without heave plate under potential flow assumptions. The workflow of the potential flow model has been discussed under Section 3.2 and the potential flow theory is discussed in Section 2.4. In this section the results of the potential flow model are presented.

4.1. Added Mass

The damping, added mass and wave excitation forces of both the column with and without heave plate have been calculated using the potential flow package WAMIT. The results of this analysis are presented in Figure 4.1 and Figure 4.2. Note that in these figures the added mass in heave direction A_{33} has been nondimensionalised with the mass of the structure m . Finally, note that the results presented in this chapter are based on a freely floating structure.

As one can see in Figure 4.1 and Figure 4.2 the added mass remains relatively constant for the various wave periods. The addition of a heave plate to the column induces an extra local maximum in the added mass plot. When comparing the added mass for the column with and without heave plate, one can see that the addition of the heave plate increases the added mass per unit mass of the structure with approximately a factor 4. In absolute terms the added mass at the heave natural period increases with a factor 6.55.

It can be useful to compare these values with the added mass approximation given by Tao et al. (2007). For this theoretical approximation of the added mass, it is assumed that the fluid moves "as an attached homogeneous mass" (Tao et al., 2007), which implies that no turbulent flow phenomena can be assessed with this approximation. The added mass in heave A_{33} is given by Tao et al. (2007) as:

$$A_{33} = \frac{1}{12} \rho \left(2D_{hp}^3 + 3\pi D_{hp}^2 z - \pi^3 z^3 - 3\pi D_c^2 z \right) \quad (4.1)$$

where D_c , is the diameter of the column (to which the disk is attached); D_{hp} , is the diameter of the heave plate; and $z = \frac{1}{\pi} \sqrt{D_{hp}^2 - D_c^2}$.

For the present column with heave plate, the added mass based on the approximation from Tao et al. (2007) is $A_{33}/m = 0.27$ normalized by the structures mass, which is significantly lower than the added mass found by WAMIT: $A_{33}/m \approx 0.87$.

Another approximation for the added mass is the mass of the displaced volume by half a sphere with the diameter of the heave plate: $A_{33} = \rho \frac{1}{2} \frac{\pi}{6} D_{hp}^3$. This results in an overestimation of the added mass by approximately 70% compared to the potential flow solution.

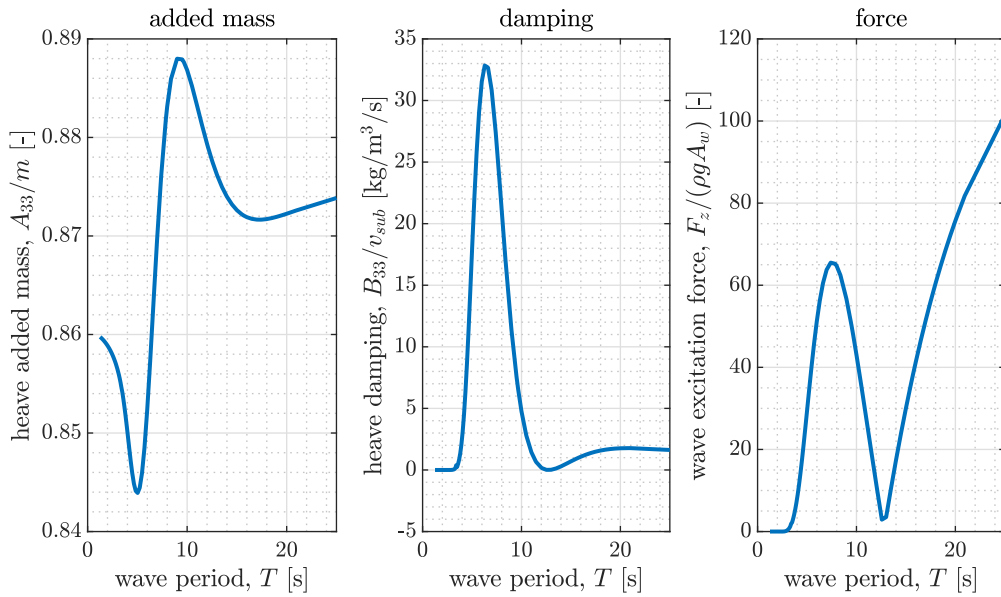


Figure 4.1: Added mass, damping and wave excitation force for the DeepCwind column with heave plate. The results are obtained from the potential flow model WAMIT. Note that the values on the vertical axes have been normalized. A_w is the wave amplitude; v_{sub} is the submerged volume of the floater; ρ , is the water density; and g , is the gravitational acceleration.

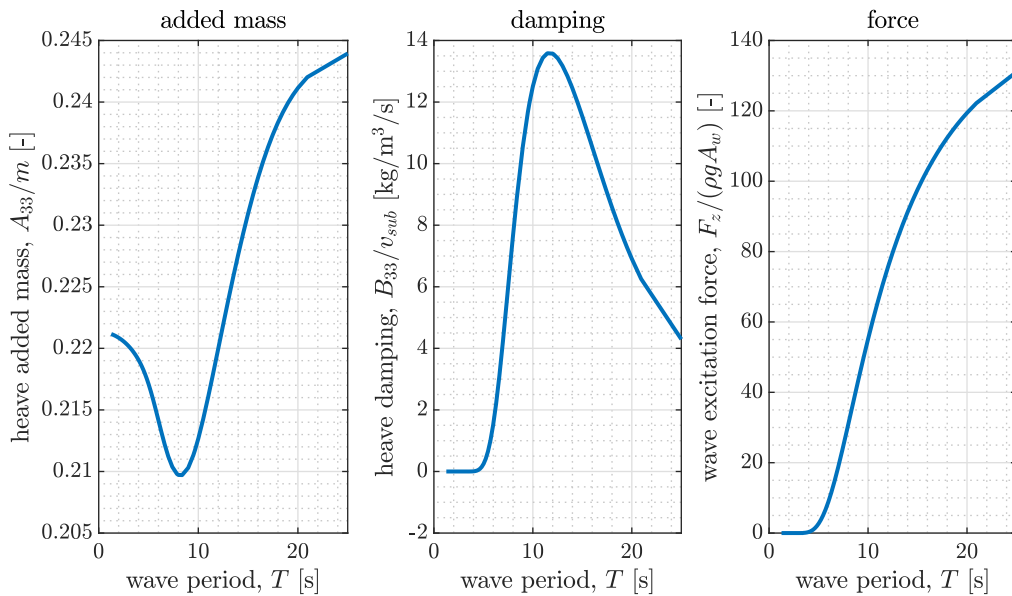


Figure 4.2: Added mass, damping and wave excitation force for the DeepCwind column without heave plate. The results are obtained from the potential flow model WAMIT. Note that the values on the vertical axes have been normalized. A_w is the wave amplitude; v_{sub} is the submerged volume of the floater; ρ , is the water density; and g , is the gravitational acceleration.

4.2. Damping

The potential damping calculated with WAMIT is also shown in Figure 4.1 and Figure 4.2. As one can see in these two figures, the damping varies much more than the added mass. In both cases a clear peak can be identified at wave period $T = 6.3$ s and $T = 11.5$ s for the column with and without heave plate respectively. In potential flow theory, the structure's ability to generate waves is the cause for the radiation damping. Therefore, the damping decreases towards zero for both very short waves and very long waves. In between these two areas, the peaks in the damping can be distinguished.

In addition to the wave length, the wave cancellation frequency (or period) plays an important role for the column with heave plate. As explained in Section 2.9, the wave cancellation period is the wave period at which the wave excitation heave force is zero, due to the force at the top and the bottom of the heave plate cancelling out. Due to this phenomenon, the heave radiation damping goes to zero at the wave cancellation frequency. In Figure 4.1, the local minimum in the damping at $T_c \approx 12.7$ s indicates wave cancellation. This wave cancellation period is in agreement with the analytical solution presented in Section 2.9, where the wave cancellation frequency ω_c was given as (Equation 2.39):

$$\omega_c = \sqrt{\frac{g}{z_m + \frac{g}{\omega_n^2}}}$$

For the heave plate geometry, the wave cancellation frequency can simply be found as $\omega_c = 0.492$ rad/s, meaning that the wave cancellation period is $T_c = \frac{2\pi}{\omega_c} = 12.75$ s.

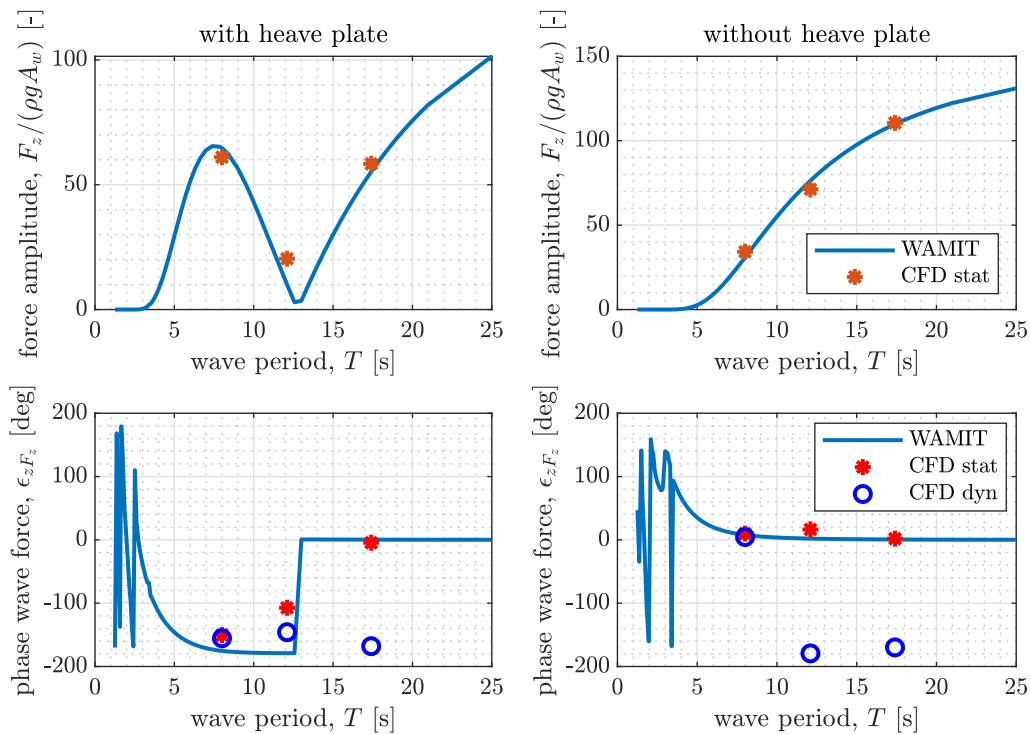


Figure 4.3: Wave excitation force amplitude and wave excitation force phase. The WAMIT results are obtained directly from the potential flow model WAMIT, whereas the CFD-results are obtained from the results presented in Chapter 5. Note that the 'static' case refers to a fixed body, whereas the 'dyn[amic]' case refers to a moving body in heave. The CFD-results have been scaled to full-scale size and non-dimensionalised with the wave amplitude A_w , water density ρ and gravitational acceleration g .

The addition of the heave plate seems to increase the damping per unit submerged volume significantly. The peak of the damping of the column with heave plate is almost twice as high as the peak of the heave plate without column. On the other hand, the damping increases steeply at relatively smaller wave periods for the column with heave plate as the wave period approaches the wave cancellation period.

4.3. Wave Excitation Forces

Finally, the heave wave excitation forces calculated with the potential flow model WAMIT are shown in Figure 4.1 and Figure 4.2. The wave excitation force for the column with heave plate (Figure 4.1) shows a local maximum and minimum, whereas the excitation force for the column without heave plate gradually approaches a constant value for high wave periods. The local maxima and minima are, again, caused by the wave cancellation period, which is derived in Section 2.9.

Also, the phase of the wave excitation forces has been plotted in Figure 4.3. Note that this figure also contains the results from the CFD model. In Chapter 6 an in-depth comparison of the potential flow results and the CFD results is given.

4.4. Response Amplitude Operator

The Response Amplitude Operator (RAO) obtained with WAMIT is shown in Figure 4.4 and Figure 4.5. Note that these figures also include the CFD results. A comparison of the CFD results and potential flow results is included in Chapter 6.

For the column with heave plate, the RAO goes to zero at the wave cancellation period $T_c \approx 12.75$ s, as discussed in Section 2.9. For very short waves (small wave period) the structure is also not excited by the waves, as the wave length is well below diameter of the column and heave plate. Consequently, multiple wave crests and troughs fit within one column diameter. Furthermore, the natural period of the structure in heave is clearly visible in Figure 4.4. Around natural period $T_n \approx 15.2$ s the response drastically increases due to resonance. For this wave period, the vertical motions are dominated by the damping term. However, it should be noted that at the natural period, potential

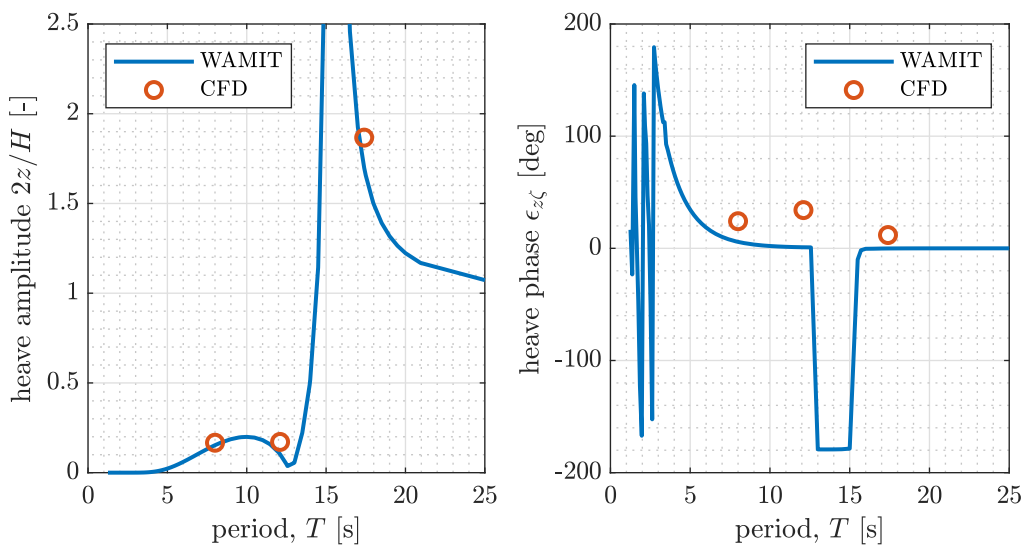


Figure 4.4: Response Amplitude Operator (RAO) and phase characteristic for the DeepCwind column with heave plate.

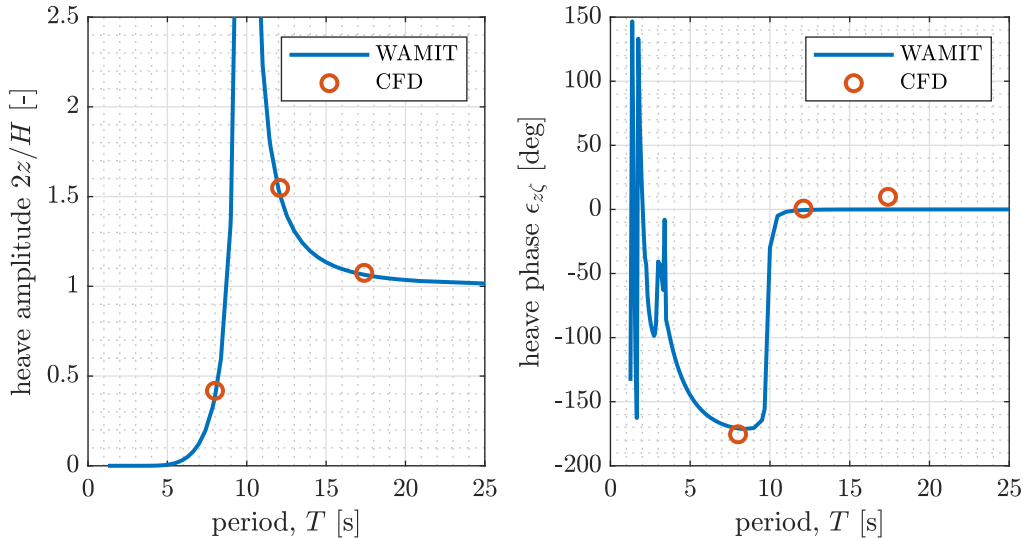


Figure 4.5: Response Amplitude Operator (RAO) and phase characteristic for the DeepCwind column without heave plate.

flow theory does not give realistic RAO values, as for large amplitudes viscous damping becomes more important, which is not taken into account in potential flow theory. As expected, the RAO approaches one for long (high period) waves; the structure tends to 'follow' the waves for these high period waves.

The RAO of the column without heave plate shows a similar trend as the column with heave plate. However, with the lack of a heave plate, the effect of the wave cancellation period can not be seen as this is a heave plate specific feature. Also, the peak of the RAO is shifted towards lower wave periods. This is due to the natural period in heave of the structure without heave plate being lower.

The phase characteristics of the two columns are also depicted in Figure 4.4 and Figure 4.5. For a column without heave plate, the phase characteristic is theoretically expected to be close to zero for small wave periods T . This is expected because for short waves the Froude-Krylov force becomes relatively small. Consequently, the wave force becomes dominated by the out-of-phase diffraction force, pushing the phase of the response of the structure towards zero. As one can see in Figure 4.5, this effect can not be distinguished in the phase characteristic obtained with WAMIT. Instead, the phase characteristic shows many local peaks for small wave periods for both columns (with and without heave plate). This is likely due to the fact that the damping at these frequencies is very low and the motions are calculated at discrete frequencies. This gives sort of an arbitrary behaviour of the wave excitation forces around the small wave periods.

For long waves relative to the size of the structure, the structure tends to 'follow' the wave. Therefore, both phase characteristics for the column with and without heave plate, are zero for high wave periods T . Going from the high period waves towards the lower wave period regime, a sudden phase change of -180° around the natural period of both columns can be observed. Whereas the motion is dominated by the spring terms for high period waves, the motion is dominated by the damping terms around its natural period. Consequently, the phase of the response of the structure shifts in order to align with the damping terms, which scale with the out-of-phase velocity.

The phase characteristic of the column with heave plate remains low until after it reached the wave cancellation period at $T_c \approx 12.75$ s, where the wave excitation forces are cancelled out. The phase changes suddenly at the wave cancellation period, due to a sign change of the wave force amplitude,

which is shown in section 4.6. At this point the diffraction force and the Froude-Krylov force are equal in magnitude but opposite in direction. For lower wave periods (below the wave cancellation period T_c), the structure follows the phase of the wave excitation force which still has a negative sign (see Figure 4.3), and therefore slowly increases towards 180° , before the arbitrary behaviour discussed above starts.

Finally, the phase characteristic of the column without heave plate approaches zero for small wave periods for reasons mentioned above: the wave length becomes very small with respect to the diameter of the structure.

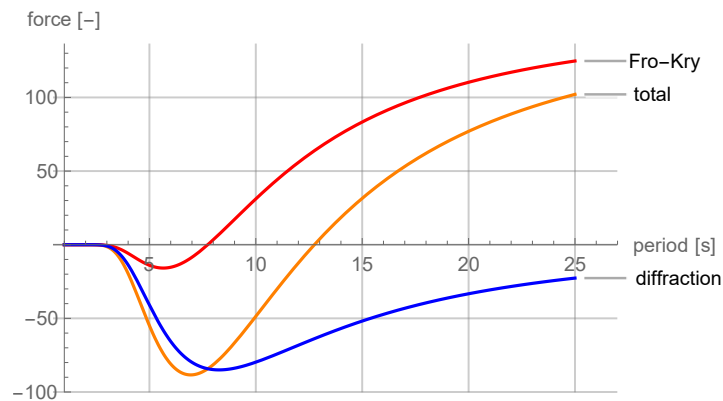


Figure 4.6: The wave excitation force amplitude, calculated based on the analytical solution from Equation 2.37. The Froude-Krylov force, diffraction force and the total force are all plotted separately. The force has been scaled with the water density and the gravitational acceleration: $F_w / (\rho g)$. Note that damping $b = 0$ has been assumed. The sum of the mass and added mass have been calculated based on Equation 2.38 and the added mass has been assumed to be 87% of the mass.

5

Case Study Column With and Without Heave Plate

In order to obtain more insight into the effects of the heave plate on the hydrodynamic behaviour of a vertically floating column, a column similar to the DeepCwind geometry is analysed using CFD simulations. As discussed in Chapter 3 the open source software package OpenFOAM has been used throughout this work. In particular, the waves2Foam toolbox (Jacobsen, 2017) has been used.

The main focus of this study is the heave plate and its effects on the hydrodynamic response of the structure. Therefore, the case study of the DeepCwind floater consists of two kinds of test, focused on the response in heave direction:

- heave decay tests;
- freely moving structure in heave direction under wave loading; and
- constrained structure in all directions under wave loading.

The author of this work has chosen to align the properties of the waves that have been analysed with work carried out by Rivera-Arreba (2017). In the following the numerical set-up of all tests is discussed and the results are presented.

5.1. Heave Decay Test

In order to obtain insight into the hydrodynamic damping of the columns with and without a heave plate, a heave decay test has been carried out, both with and without heave plate. This section describes the spatial domain, the set-up of the experiment and the results of the heave decay test.

The spatial domain that has been used, is based on the domain used in Bruinsma (2016), where a heave decay test with the full DeepCwind floater was carried out, including a mesh convergence study. The total size of the domain is $4 \text{ m} \times 4 \text{ m} \times 4.624 \text{ m}$ in x-, y- and z-direction respectively. The water depth was 4 m, meaning that the air gap on top of the water was 0.624 m. The model scale diameter of the heave plate is $D_{hp} = 0.48 \text{ m}$ and the draft of the structure is 0.4 m.

The blockMesh utility was used in order to construct a background mesh, whereas the snappy-HexMesh utility was used to 'cut out' the shape of the structure from the background mesh. Using the simpleGrading technique, the background mesh was refined around the water surface. The

Direction	Domain length	Number of cells	Cell size Δ
x, y	4 m	84	4.76 cm
z	4.624	54	water surf.: 4.63 cm other: 9.51 cm

Table 5.1: Mesh size for the heave decay test. Around the water surface, the mesh was refined in z-direction, whereas outside this area, the mesh size was increased, following suggestions from Bruinsma (2016).

mesh size of the background mesh is presented in Table 5.1. As a 'rule of thumb' 5 p.p.c.d. (points per cylinder diameter) was used for the size of the background mesh, as suggested by Bruinsma (2016).

The column was lifted 0.02 m (1 m in full-scale) from its initial position and released at time $t = 0$ s. Movements of the column were restricted in all directions except for heave direction. The discretization schemes as described in Section 3.1.2 were used and no relaxation scheme for the mesh motion was applied. As described above, the width of the domain was chosen as 4 m, in order to be consistent with other literature. However, this also means that the decay test will suffer from significant wave reflections, which disturb the measurements. Therefore, only data from the first 5.5 oscillation periods was used to calculate the damping. It was determined empirically that after ca. 6 oscillations the reflected waves started dominating the response of the structure, especially in the case without heave plate.

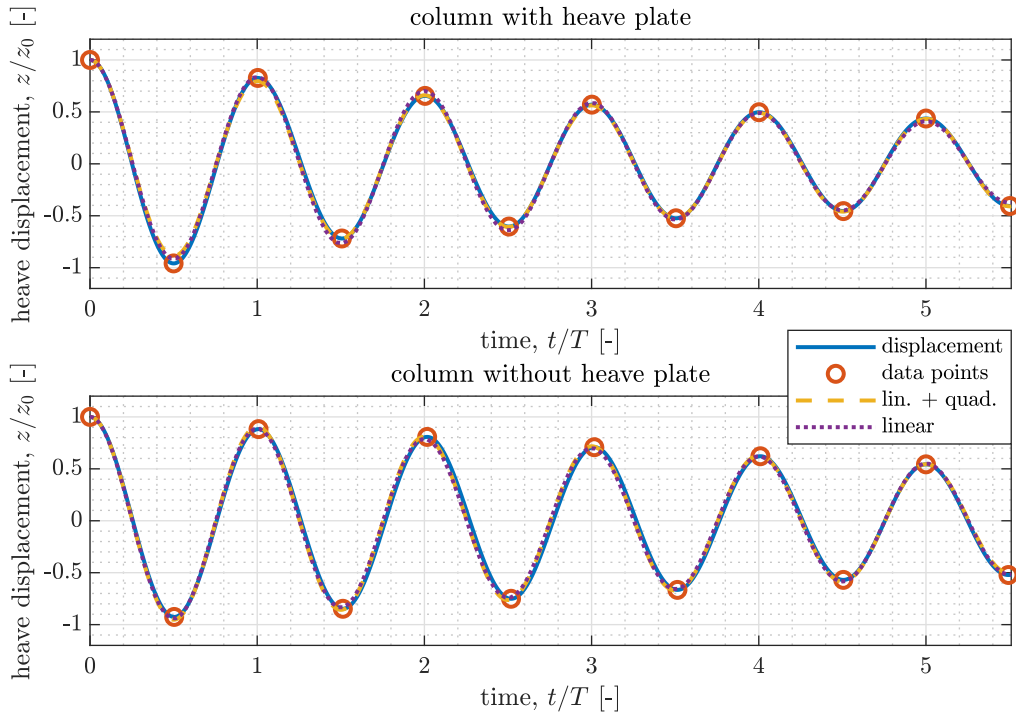


Figure 5.1: Time series of heave decay test. Heave displacement has been normalised by the initial displacement z_0 and the time has been normalised by the damped natural period T , $T = 15.2$ s and $T = 9.83$ s for the column with and without heave plate respectively (full scale). The line referred to as 'displacement' in the legend is the raw data, the 'data points' represent the points that have been used in order to calculate the damping coefficients, 'lin. + quad.' refers to the reproduced solution obtained with the method presented by (Roberts, 1985) using both linear and quadratic damping coefficients b_1 and b_2 and the line 'linear' refers to the reproduced solution based on the linear damping coefficient κ .

	Initial displacement [m]	b_1 [1/s]	b_2 [1/m]	κ [-]
without heave plate	1	$4.31 \cdot 10^{-2}$	$-4.41 \cdot 10^{-2}$	$1.89 \cdot 10^{-2}$
with heave plate	1	$1.48 \cdot 10^{-3}$	$9.11 \cdot 10^{-2}$	$2.82 \cdot 10^{-2}$
full floater (Rivera-Arreba, 2017)	1	$4 \cdot 10^{-3}$	$1.6 \cdot 10^{-1}$	$4.81 \cdot 10^{-2}$

Table 5.2: Linear and quadratic damping coefficients (b_1 and b_2 respectively) from the heave decay test. The values are calculated for the full size structure. Also the linear damping coefficient κ is presented.

A time series of the decay test of the column with and without heave plate can be seen in Figure 5.1. Based on this data the linear and quadratic damping coefficients, b_1 and b_2 respectively, have been calculated based on the energy conservation method, developed by Roberts (1985). The values for b_1 and b_2 are listed in Table 5.2. Note that these values are based on the full size column.

As explained in Section 2.10 the linear and quadratic damping coefficients are based on the following equation of motion:

$$\ddot{z} + b_1 \dot{z} + b_2 |\dot{z}| \dot{z} + \omega_n^2 z = 0 \quad (5.1)$$

where z , is the location of the structure in heave direction; b_1 and b_2 , represent the linear and quadratic damping coefficients; and ω_n , is the damped natural frequency of the structure in heave direction (since this is a lightly damped system, the natural frequency is approximated with the damped natural frequency $\omega_0 \approx \omega_n$).

This equation has been solved numerically using the b_1 and b_2 values from Table 5.2 and the result is plotted along with the original data in Figure 5.1. As one can see from this figure, the energy conservation method manages to reproduce the behaviour of the column during the decay test rather accurate. Furthermore, the data points that were used for the calculation of the damping coefficients are highlighted in this figure.

A second method has been used to quantify the damping in the heave decay test. This method is based on solely a linear damping coefficient κ . As discussed in Section 2.10 the linear damping coefficient κ is defined as the ratio between the actual damping and the critical damping. This method makes use of the following equation of motion:

$$\ddot{z} + 2\kappa\omega_0 \cdot \dot{z} + \omega_0^2 \cdot z = 0 \quad (5.2)$$

The damping coefficients κ were found by fitting the decay of the motion amplitude with a simple exponential decay function using a nonlinear least-squares regression algorithm, as described in Section 2.10. The results of this analysis are presented in Table 5.2. Also, the results of this method were reproduced based on the equation of motion above and are shown in Figure 5.1.

From a comparison of the damping coefficients in Table 5.2 one can conclude that the quadratic damping coefficient increases significantly due to the addition of the heave plate. Remarkably, in the case without heave plate the quadratic damping coefficient b_2 has a negative value. In reality, this is an unphysical value. It could be the result of either a small deviation of the rest position of the column or reflections at the boundary of the numerical domain.

The interpretation of the linear damping coefficient κ is more straight forward. In addition, Figure 5.1 indicates that this damping coefficient manages to reproduce the actual solution fairly accurate. The linear damping coefficient κ increases with almost 50% due to the addition of the heave plate. The full floater has an even higher damping coefficient: ca. 70% above the damping coefficient of a single column with heave plate.

For the calculation of the damping coefficients, the natural frequency ω_0 in heave direction of the structure needs to be assessed. For lightly damped systems, the natural frequency can be approximated using the damped natural frequency ω_n , which can be obtained from the heave decay test. Two different approaches have been used in order to determine the natural frequency:

- Fourier Transform Analysis; and
- average period in between peaks in time series.

For the first method, the total length of the time series, determines the accuracy of the natural frequency. Therefore, for the Fourier Transform analysis, the full length of the time series (45 seconds) is used. However, it should be noted that reflections at the boundaries of the spatial domain have likely affected the oscillation period to a certain extent. Nevertheless, this method gives a good idea of the damped natural period T_n : $T_n = 15.15$ s for the column with heave plate and $T_n = 9.64$ s for the column without heave plate.

The second method is in this case more accurate, since the accuracy does not depend on the length of the time signal and the part of the signal that is expected to be least disturbed by reflections can be used. The first five to six oscillation periods the oscillation amplitude decays steadily. However, later on in the time series the oscillation amplitude increases due to the reflected waves. Therefore, only the first part of the time series, up to 5.5 oscillation periods, has been used for the calculation of the damped natural frequency. The average time between the peaks in the heave oscillation has been calculated and was found to be $T_n = 15.24$ s for the column with heave plate and $T_n = 9.83$ s for the column without heave plate.

5.1.1. Quantification of Viscous Damping

The damping measured during the heave decay test consists of two components: radiation damping b_r and viscous damping b_v (McCormick, 2009). Since potential flow theory does not take into account the vorticity and viscosity of the fluid, the potential flow model results (see Chapter 4) give only the radiation damping. Thus, by subtracting the damping from the potential flow results from the damping measured with the CFD model, the viscous damping b_v can be obtained. The damping coefficient κ , which was calculated for the CFD heave decay test, is defined as the ratio between the damping b and the critical damping b_{cr} . Since the potential flow model gives both the added mass and the damping of the structure, the damping ratio κ_r from only the radiation damping can be calculated as follows:

$$\kappa_r = \frac{b_r}{b_{cr}} = \frac{b_r}{2\sqrt{(m+a)} \cdot c} \quad (5.3)$$

Using the potential flow model results, the damping ratios that were obtained are presented in Table 5.3. Note that the added mass and damping are frequency dependent. The values presented in Table 5.3 are obtained for the damped natural frequency of the structure in heave direction. Also,

structure	κ [%]	κ_r [%]	κ_v [%]
column with heave plate	2.82	0.0520	2.77
column without heave plate	1.89	0.787	1.10

Table 5.3: Damping coefficients κ for the column with and without heave plate at damped natural period. The values κ refer to the total damping coefficient, obtained from the CFD heave decay test. The values κ_r refer to the damping due to radiation and are determined based on the potential flow model. Finally, κ_v refers to the viscous damping and is based on the difference between κ and κ_r .

	f [Hz]	T[s]	H[m]	λ [m]	$\frac{d}{gT^2}$	$\frac{H}{gT^2}$	Wave theory CFD
full-scale	0.08	12.1	7.1	231.0	0.139	0.005	Stream function
model scale	0.584	1.71	0.142	4.61	idem	idem	Stream function

Table 5.4: Wave properties for regular wave with period $T = 12.1$ s (full-scale).

one should consider the fact that the potential flow model assumes an infinite domain size, whereas the width and length of the CFD model is limited. Nonetheless, it is expected that the values from the potential flow model and the CFD model can be compared and combined sufficiently adequate.

From the interpretation of the data in Table 5.3, one can conclude that the radiation damping at the heave natural frequency of the structure is dominated by the viscous damping. Especially for the structure with heave plate, the radiation damping plays a minor role. It is worth noting that the radiation damping for the column with heave plate at the heave natural period is especially low compared to the radiation damping at lower periods (see Figure 4.1). Finally, one should bear in mind that since an unresolved DNS approach has been used throughout this work, the viscous sublayer is not completely resolved by the CFD model and therefore the viscous damping is likely underestimated.

5.2. Response Under Wave Loads

The performance of the heave plate is assessed under different wave loads from regular waves. The wave period has been varied from $T = 8$ s, $T = 12$ s and $T = 17.4$ s. In the following the response of the floater in heave direction is discussed for all three wave periods. However, first the set-up of the numerical experiments and the measured data is discussed.

The set-up of the experiments was based on Bruinsma (2016) and Rivera-Arreba (2017). A spatial domain with both a width and a water depth of 4 meters was used. This was chosen in order to align with the previously mentioned work, which was based on the size of a wave basin of which experimental test results were used for verification. Note that the total height of the numerical domain exceeds 4 meter since an air gap on top of the water is also included in the numerical domain. The domain length was varied depending on the wave length, in order for the relaxation and wave generation zone to have sufficient length. The same principle applies for the cell size. This was also chosen based on the wave length and largely based on Rivera-Arreba (2017), who performed convergence studies for each wave period.

For each wave period the response of the structure was assessed while it was free to move in heave and while all movements of the structure were restrained. Within OpenFOAM both the force and the surface elevation at specific points were measured (see Section 3.1.7).

5.3. Wave Period $T = 12.1$ s

The first wave period under which the behaviour of the column is assessed is a wave with wave period $T = 12.1$ s (full-scale). All wave parameters are listed in Table 5.4. As described in Section 2.2 the Fenton Stream Function was used to generate the incoming waves.

5.3.1. Spatial Domain

The main mesh parameters are listed in Table 5.6. In order to confirm that the mesh captures all flow phenomena sufficiently accurate, a mesh convergence study can be carried out. In this

case	length inlet [m]	length outlet [m]	total length [m]
$T = 17.4$ s	2.2	10	22
$T = 12.1$ s	4.7	4.7	13
$T = 8$ s	2.2	4.4	9.2

Table 5.5: The length of the spatial domain for each of the cases with regular waves.

	Domain length	Number of cells	Cell size δ
x: w/ heave plate	13 m	282	4.61 cm (~ 100 p.p.w.l.)
x: w/o heave plate	13 m	141	9.22 cm (~ 50 p.p.w.l.)
y: w/ heave plate	4 m	86	4.65 cm (~ 100 p.p.w.l.)
y: w/o heave plate	4 m	43	9.30 cm (~ 50 p.p.w.l.)
z: w/ heave plate	4.5 m	106	water surf.: 2.35 cm (~ 6 p.p.w.h.) other: 4.62 cm (~ 100 p.p.w.l.)
z: w/o heave plate	4.5 m	76	water surf.: 1.50 cm (~ 10 p.p.w.h.) other: 9.43 cm (~ 50 p.p.w.l.)

Table 5.6: Size of the background mesh for wave period $T = 12.1$ s. Cell size is expressed both in centimeter (cm) and in points per wave length (p.p.w.l.) or points per wave height (p.p.w.h.)

type of study the same set-up is simulated with different mesh coarsenesses. Both the response of the structure and the surface elevation should be sufficiently converged for the chosen mesh resolution. Based on a convergence study by Rivera-Arreba (2017) applied to the full DeepCwind floater, the cell size for the background mesh was chosen as 50 p.p.w.l. (points per wave length) was used. In the study by Rivera-Arreba (2017), a 2% difference between the highest and the lowest grid refinements in average crest-to-trough amplitude was found for the response of the structure in heave direction. Rivera-Arreba (2017) used a mesh refinement around the water surface of ca. 3.5 p.p.w.h. (points per wave height). However, throughout the course of this work the column with heave plate was simulated with two types of meshes: 50 p.p.w.l. with refinement of 3 p.p.w.h. around the water surface and 100 p.p.w.l. with refinement of 6 p.p.w.h. around the water surface. A significant difference was noted between these two simulations. Both the wave height close to the structure and the heave response of the structure increased for the finer mesh with ca. 20%. The difference in wave height and response indicates that the initial mesh size was not sufficiently fine in order capture the development of the wave height sufficiently accurate. On the other hand, the linear response of the structure with the wave height (both the wave height and the heave response amplitude increased with 20%) indicates that the normalised results might still give reliable results. Finally, a comparison between a mesh with 50 p.p.w.l. with refinement of 10 p.p.w.h. and a mesh with 100 p.p.w.l. with refinement of 6 p.p.w.h. indicated that it is mostly the refinement around the water surface that affects the wave height.

For the results presented in this section, the simulations with the finest mesh resolutions have been used. However, due to limitations in computational time and resources the mesh resolution for the static and dynamic case differs. The mesh resolution that was used is presented in Table 5.6

The length of the domain was chosen based on the wave length, as the absorption zone (outlet) should be at least one wave length, in order to prevent reflection of the wave. The total length of the domain and the length of the inlet - where the waves are generated, and the outlet - the absorption zone - is given in Table 5.5.

wave period	heave plate	fixed/free	wave height, H/H_{input} [%]
$T = 17.4$ s	with	fixed	114
		free	173*
	without	fixed	116
		free	173
$T = 12.1$ s	with	fixed	114
		free	110
	without	fixed	111
		free	100
$T = 8$ s	with	fixed	80
		free	71
	without	fixed	79
		free	71*

Table 5.7: Measured mean wave height at $x = 0$ m and $y = 1.5$ m. Note that in two cases problems occurred with the waveGauges utility in OpenFOAM. As a consequence no (or not enough) wave height data was available in these cases. Therefore, the numbers marked with a star (*) are copied from the same wave period and the same fixed/free condition.

5.3.2. Wave Height and Transient Regime

The wave height during the simulation has been measured on a number of locations indicated in Figure A.2. In this figure one can clearly distinguish the interaction of the structure with the wave height. As the distance to the structure decreases, the wave height is clearly more affected by the structure. Even though the the effect of the structure on the wave height varies from case to case, there is a clear overall trend indicated by Figure A.1. Close to the structure the wave height tends to increase, whereas further away from the structure, especially further downstream, the wave height decreases. Since the wave height is not constant over the length of the wave basin, the input wave height from Table 5.4 can not be used in order to scale the obtained data. Instead, the mean wave height at $x = 0$ m and $y = 1.5$ m (wave gauge 8, Figure A.2) has been used. Note that this is true for any wave period that was used throughout this work. The actual measured wave height for each of the simulations is therefore listed in Table 5.7.

Over the course of one wave period, the wave height in the inlet relaxation zone steadily increases. Due to the changing wave height, the force on the structure initially shows unsteady behaviour. After circa seven wave periods T the force has become relatively stable and a steady-state regime has been reached. This is indicated in Figure 5.2 and Figure 5.3, which show the 'moving mean' and the heave force amplitude that converge to relatively constant values after seven periods T . Therefore the first seven wave periods were chosen as the transient regime and were not used for the analysis. From Figure 5.2 it can also be seen that the total simulated time differs per case. This is due to limited available time for carrying out the simulations.

5.3.3. Force and Displacement of the Structure

The force and the displacement has been measured (the latter only for the cases where the structure could freely move in heave). In Figure 5.5 a time series of the displacement for the the DeepCwind column both with and without heave plate is shown. It can be seen that the addition of the heave plate has affected the response significantly at the present wave period. The excitation of the structure with heave plate is approximately a factor 10 lower than the excitation of the structure with heave plate. However, one should be cautious with addressing this change only to the increased

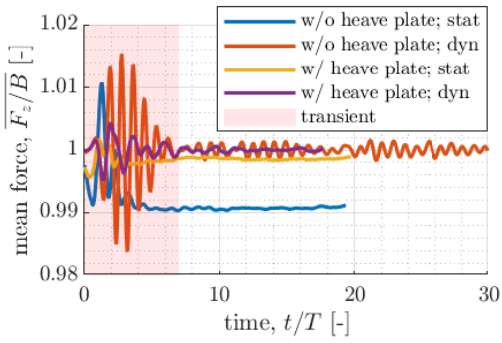


Figure 5.2: Moving mean of the heave force normalized by the buoyancy for wave period $T = 12.1$ s. Width of the window over which the mean was calculated is equal to wave period.

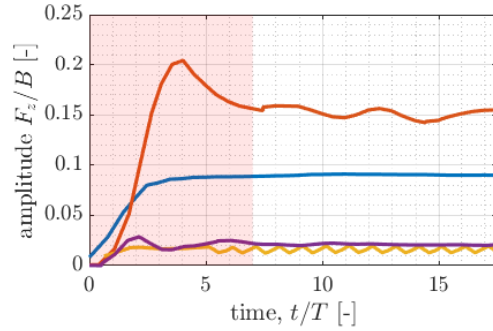


Figure 5.3: Time series of the amplitude of the heave force F_z on the structure normalized by the buoyancy B for wave period $T = 12.1$ s. For the legend refer to Figure 5.2.

damping of the structure. After all, the response of the structure highly depends on the wave period. The difference in response for the 12.1 s wave discussed in this section, can be explained based on the natural period of both structures. Since the 12.1 s wave is relatively close to the natural period of the structure without heave plate, this response is much higher than the response for the column without heave plate (see Figure 4.4 and Figure 4.5).

Processing Force and Motion Cycles

The motion cycles of the structure are not independent of each other. As a consequence, the possibilities for quantifying the statistical meaning of the obtained data are rather limited. Nevertheless, gathering the force and motion cycles gives insightful information. The result of this procedure for the 12.1 s wave can be seen in Figure 5.6 and Figure 5.4. Below the procedure for obtaining this data is explained, after which the results are analysed. Note that for other wave periods a similar procedure for processing the force and displacement data is followed.

In Figure 5.6 and Figure 5.4 the thin grey lines indicate the individual cycles from the time series with length of one wave period. These cycles have been obtained by identifying the first peak in the surface elevation time series after the transient zone from the wave gauge parallel to the structure (wave gauges 7 or 8, Figure A.2). From this point onward the motion and force time series of the column have been split up into sections of length of one wave period. Thus, the time $t = 0$ in Figure 5.6 and Figure 5.4 corresponds with a wave crest.

Note that the time step of the CFD data varies. Thus, for a proper analysis the force and motion data has been turned into a regularly spaced signal with constant time step $\Delta t = 0.001$ s using linear interpolation. Next, the mean heave motion and force of structure have been calculated at all time instances, the result of which is the red line. Furthermore, the standard deviation (std) has been obtained and can be identified by the blue color. At some instances one can see extremely high peaks in the standard deviation. These sharp peaks are due to the solution of the algorithm that solves the Navier-Stokes equations not being properly converged yet before proceeding to the next time step. Refer to Section 3.1 for a more in-depth discussion of this phenomenon.

Finally, the time series of the motion and force signals have been converted to the frequency domain using an FFT algorithm. The wave frequency has been filtered out from the frequency domain data and has been converted back to the time domain. Thus, the green curve in Figure 5.6 and Figure 5.4 was obtained. Note that in order to make sure that the filtered frequency was sufficiently close to the wave frequency, the length of the time series that was given as input to the FFT algorithm, was

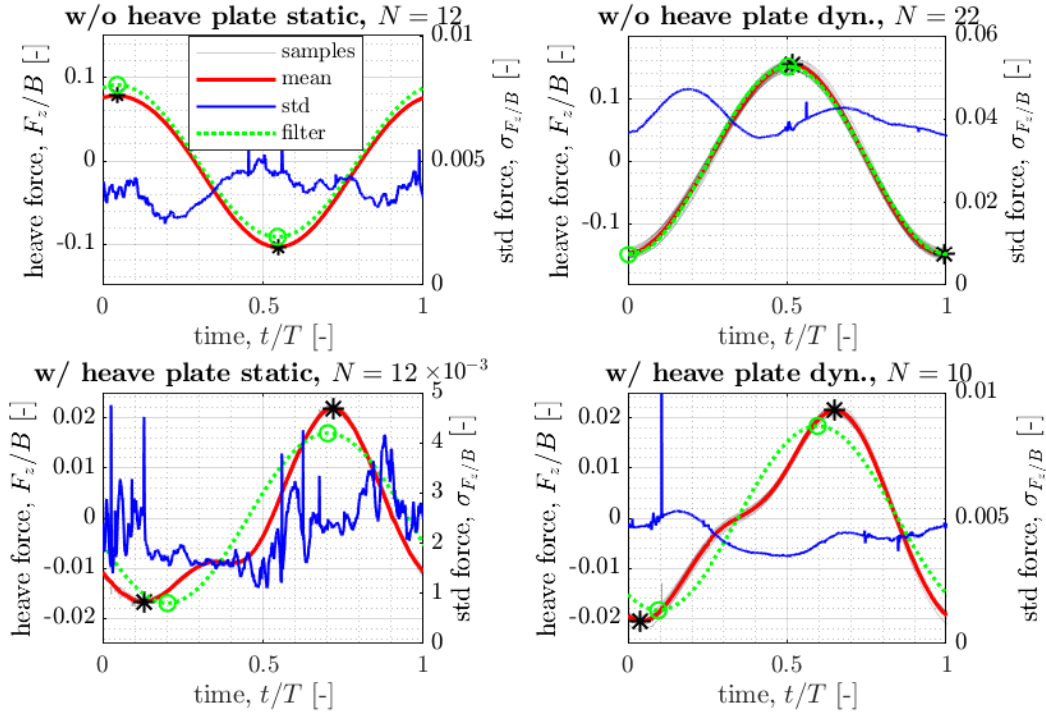


Figure 5.4: Average heave force cycles for the DeepCwind column with and without heave plate, subjected to a wave with period $T = 12.1$ s. The heave force cycles are averaged and normalized by the buoyancy B of the structure. The time is normalized by the wave period. The number of cycles (samples) that was available for the analysis is denoted by the symbol N . The words 'static' and 'dyn.' refer to the fixed and moving column respectively. The black star and green circle indicate the maximum and minimum of the 'mean' and 'filtered' signals respectively.

cut-off at a length of an integer number of wave periods T . The benefit of filtering out the wave frequency from the motion and force time series is that it allows for a better comparison with the results from the potential flow model, which assumes monochromatic force and motion signals. Note that this does change the fact that the CFD results could be very dependent on the wave amplitude, whereas the potential flow model assumes linear theory.

Analysis

It can clearly be seen that heave motion shows a high degree of repeatability. Figure 5.6 has been included in this report in order to prove this point. The average amplitude of the heave displacement without heave plate is 1.55 wave amplitudes, whereas for the column with heave plate this is only 0.174. Something else that can be learned from Figure 5.6 is that the standard deviation of the heave displacement is lower for the case with heave plate, even though the number of cycles N that was available for analysis is greater for the case without heave plate.

A time series of the heave force exerted by the flow is shown in Figure A.3 for simulations both with and without heave plate, and with a fixed structure and a freely moving structure in heave direction. When looking at the force for the simulation without heave plate, an interesting phenomenon can be pointed out. These two time series have a phase difference of ca. $0.5T$, which is not the case for the simulation with the column that does have a heave plate. This can be explained based on the motion of the column. When the column is free to move in heave, the motion of the column - and the resulting buoyancy force - dominates the wave force. Whereas when the column is fixed, the motion of the column does not affect the wave force. Consequently, in the dynamic cases (where

the structure is free to move in heave) the phase of the wave force follows the same trend as the phase of the RAO (Figure 4.4 and Figure 4.5). On the other hand, when the structure is fixed, the wave force is not affected by the motion of the structure itself. In this case, it is purely the waves that determine the phase of the wave force. As can be seen in Figure 4.3, the phase of the 'static' cases follows the same trend as the potential flow solution for the wave excitation force. Note that these results are in line with what can be expected based on potential flow theory; the 'static' case represents the diffraction problem with an incident wave on a fixed structure.

In Figure 5.4 the average heave force cycle is shown for each case: with and without heave plate, and fixed and moving. In this figure two interesting phenomena can be discovered. The first thing that can be noted, is that the amplitude of the heave force for both cases with heave plate is much smaller than for the cases without heave plate. The difference amounts a factor 4.7 and 7.3 for the fixed and moving column respectively. This significant difference is consistent with the displacement of the heave plate which is also much larger for the case without heave plate and can be related to the natural period of the structure, as discussed before.

The second phenomenon that can be noted, is the local maximum and minimum in the heave force for the cases with heave plate. Especially for the fixed structure, two very distinct local peaks can be seen around two thirds of the period T . In Figure A.4, which shows the power spectral density of the heave force, this local peak can also be noted, and is indicated by the peak at $0.5T$. In order to interpret this event, it is helpful to understand wave cancellation, described in Section 2.9. The $T = 12.1$ s wave is relatively close to the wave cancellation frequency of ca. 12.75 s (see Section 4.2). At the wave cancellation period, the wave excitation forces on the top and the bottom of the heave plate cancel each other out, resulting in a net excitation force of zero. However, this is the case under the potential flow theory assumptions. In reality and also in the CFD model, viscous drag forces on the heave plate are taken into account. As the non-viscous inertia forces are cancelled out, the viscous forces become (relatively) more important. Since the latter are out-of-phase with the inertia forces, the total wave force is no longer purely sinusoidal.

5.4. Wave Period $T = 8$ s

Another wave period under which the behaviour of the column with and without heave plate was assessed is a wave with wave period $T = 8$ s. All wave properties in model scale and full-scale are listed in Table 5.8. Note that the wave steepness of this wave is relatively high (see Table 5.9). As described in Section 2.2 the Fenton Stream Function was used to generate the incoming waves.

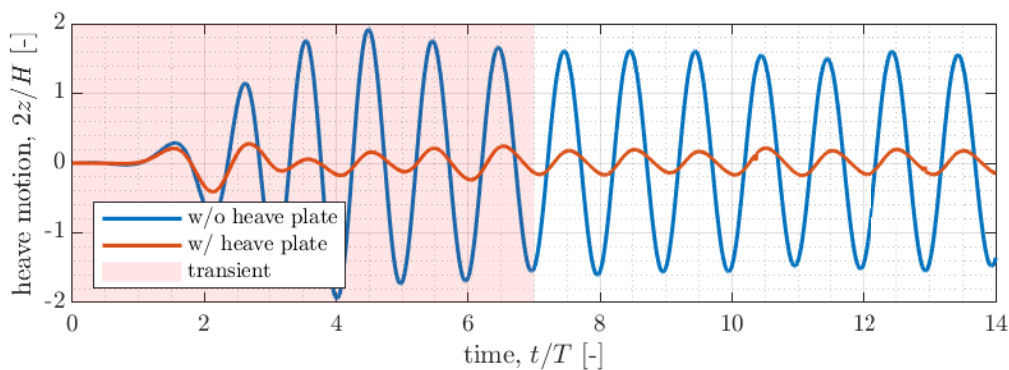


Figure 5.5: Heave motion for the DeepCwind column with and without heave plate, subjected to a wave with period $T = 12.1$ s. The heave motion is normalized by the wave height and the time is normalized by the wave period.

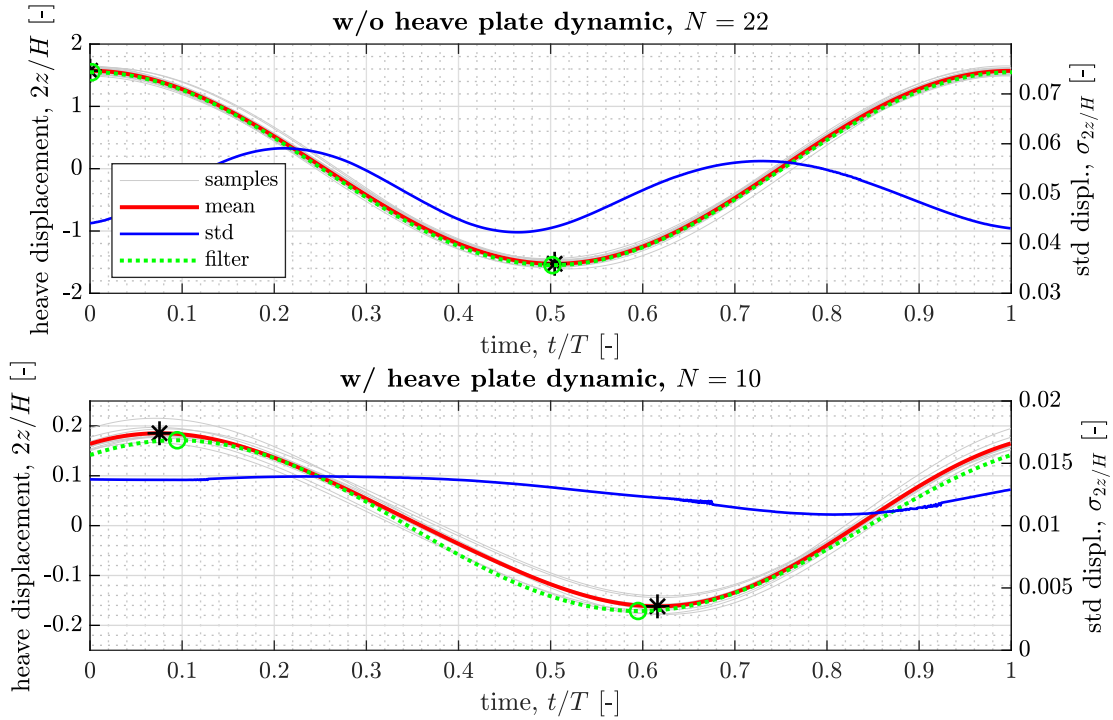


Figure 5.6: Average heave motion cycles for the DeepCwind column with and without heave plate, subjected to a wave with period $T = 12.1$ s. The heave motion cycles are averaged and normalized by the wave height. The time is normalized by the wave period. The number of cycles (samples) that was available for the analysis is denoted by the symbol N .

	f [Hz]	T [s]	H [m]	λ [m]	$\frac{d}{gT^2}$	$\frac{H}{gT^2}$	Wave theory CFD
full-scale	0.125	8	8.45	105.9	0.319	0.0135	Stream function
model scale	0.884	1.13	0.169	2.12	idem	idem	Stream function

Table 5.8: Wave properties for regular wave with period $T = 8$ s (full-scale).

wave period, T [s]	wave steepness, kA [-]
8	0.251
12.1	0.0966
17.4	0.0201

Table 5.9: Wave steepness kA for all wave periods. k represents the wave number and A the wave amplitude.

5.4.1. Spatial Domain

The width and height of the domain were similar to those in previous cases that were discussed. However, the length of the domain was different, since the domain length depends on the wave length. As described in Table 5.5 the total length was 9.2 m. For the construction of the background mesh, again the rule of thumb of 50 p.p.w.l. was used (Rivera-Arreba et al., 2019). Based on this rule of thumb the size of the background mesh that was used is as described in Table 5.10.

From this table it becomes clear that the number of points per wave height around the water surface is smaller than in the case for wave period $T = 12.1$ s, for the current case it is 6 p.p.w.h. compared to 10 p.p.w.h. in the $T = 12.1$ s case. This limited number of cells around the water surface may compromise the results of this simulation. Especially one should be careful for numerical dissipation

Direction	Domain length	Number of cells	Cell size δ
x	9.2 m	212	4.34 cm (~50 p.p.w.l)
y	4 m	92	4.34 cm (~50 p.p.w.l)
z	5 m	120	water surf.: 2.78 cm (~6 p.p.w.h.) other: 4.34 cm (~50 p.p.w.l)

Table 5.10: Size of the background mesh for wave period $T = 8$ s. Cell size is expressed both in centimeter (cm) and in points per wave length (p.p.w.l.) or points per wave height (p.p.w.h.)

of the wave height. Therefore, ideally a mesh convergence study for each wave period case shall be carried out, but due to the restricted time that was available, the author leaves this for future investigations.

5.4.2. Wave Height and Transient Regime

As indicated in Figure A.6 the wave height, like the case with wave period $T = 12.1$ s, builds up as one approaches the location of the structure in x-direction. Close to the structure, the wave height exceeds the initial wave height H_0 by more than 30%. Hereafter, the wave height rapidly decreases. Thus, the effect of the structure on the surface elevation is clearly visible.

As the wave height starts at zero at time $t = 0$ s, the first part of the time series can not be used for analysis. It is considered the 'transient' part of the signal. Using Figure A.8 and Figure A.9, one can see that after circa 12 wave periods T the force of the fluid on the structure has more or less converged to a steady-state. Therefore region before $t = 12T$ has been chosen as the transient part of the time series.

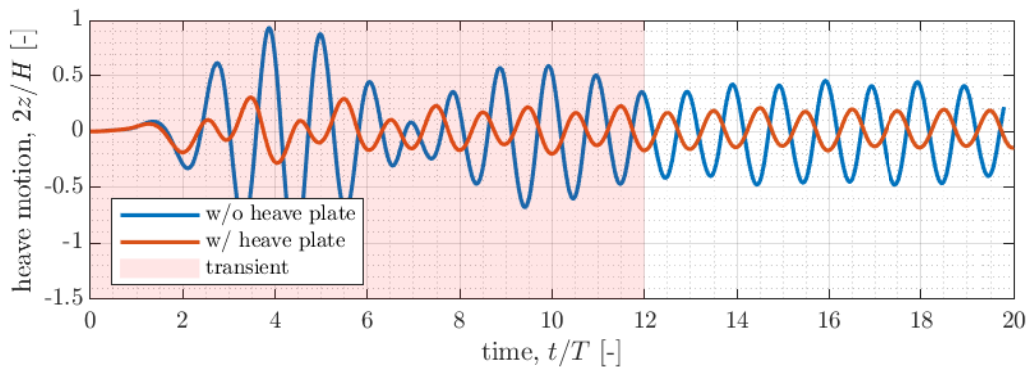


Figure 5.7: Heave motion for the DeepCwind column with and without heave plate, subjected to a wave with period $T = 8$ s. The heave motion is normalized by the wave height and the time is normalized by the wave period.

5.4.3. Force and Displacement of the Structure

From the time series of the heave motion of the column with and without heave plate in Figure 5.7 it becomes apparent that the heave plate reduces the oscillation amplitude of the structure significantly. The average amplitude of the heave motion of the column without heave plate is 2.5 times as high as the average amplitude of the column with heave plate, as indicated by Figure A.10. Even though this is a large difference, the difference is smaller than for the $T = 12.1$ s case. In the latter case, the motion amplitude for the column without heave plate also exceeded the wave amplitude. For the current case with wave period $T = 8$ s, the motion amplitude remains well below the wave amplitude. After comparison with the potential flow RAO from Figure 4.4 and Figure 4.5 one can

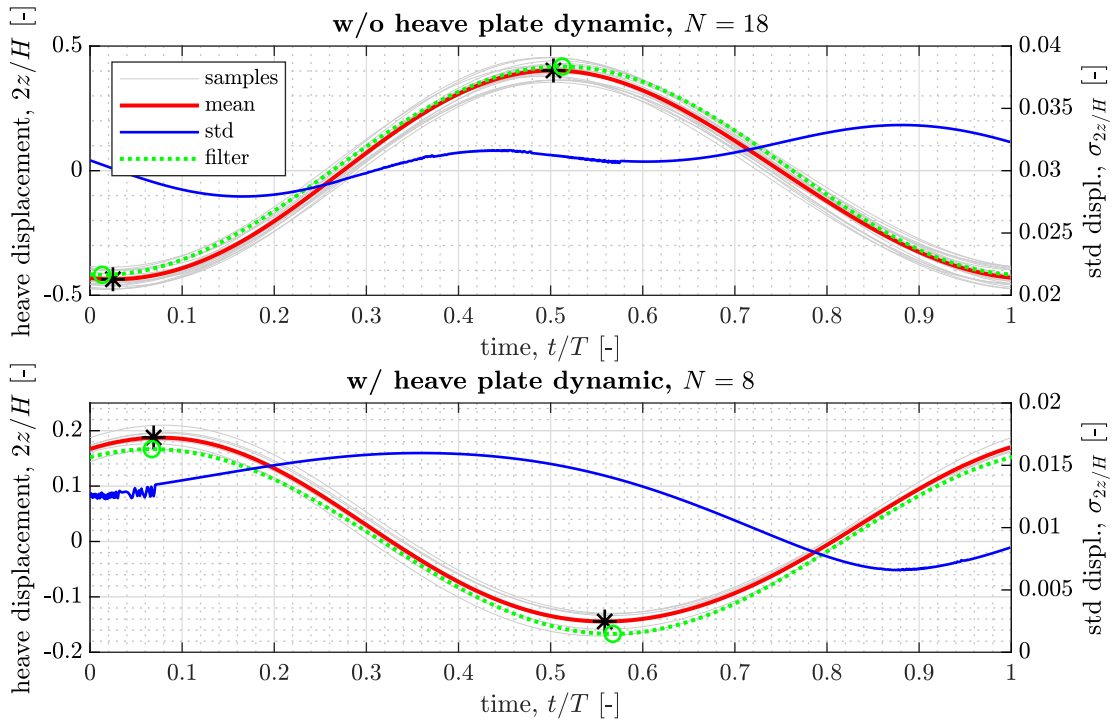


Figure 5.8: Average heave motion cycles for the DeepCwind column with and without heave plate, subjected to a wave with period $T = 8$ s. The heave motion cycles are averaged and normalized by the wave height. The time is normalized by the wave period. The number of cycles (samples) that was available for the analysis is denoted by the symbol N .

conclude that these results are in line with what would be expected based on potential flow theory. Due to the increased added mass, the natural period of the column with heave plate is significantly further away from the 8 s wave period, which causes a smaller response amplitude.

Similar to the $T = 12.1$ s case, the heave force of the column with heave plate is not purely sinusoidal; again local maxima and minima can be distinguished. Two mechanisms seem to contribute to this. However, firstly it is essential to note that the Froude-Krylov force is close to zero around the wave period $T = 8$ s (see section 4.6). This allows for other parts of the wave force to dominate the heave force. Also, this explains the phase shift of ca. $0.5T$ of the heave force on the column with heave plate.

The first mechanism that contributes to the heave force is the diffraction part of the wave force. Since the wave force has become negative, due to the Froude-Krylov force being very small and the diffraction force being relatively high (see section 4.6), the phase of the wave excitation force shifts with half a period, causing a peak in the heave force around $t = 0.5T$. This is similar to the $T = 12.1$ s case.

The second mechanism that can cause local a peak in the heave force is the drag force. Since the drag force scales with the velocity it is expected to have a phase difference of a quarter period with the wave height. The relatively high wave steepness makes that the vertical wave particle velocities are relatively high. As a consequence, it is expected that the drag force becomes more important. Thus, this is a possible explanation for the second local maximum.

Finally, Figure A.12 and Figure A.13 indicate the intuitive result that the heave force oscillates at the wave frequency. The local peak in the heave force, that is clearly visible in Figure A.10 is also visible in the power spectral density of the column with heave plate (Figure A.4). This is illustrated by the

small peak at $t = 0.5T$.

5.5. Wave Period $T = 17.4$ s

Finally, the response of the structure under a wave with period $T = 17.4$ s is assessed. This wave period was chosen since it coincides with the natural frequency of the full floater (with all three columns) in heave direction (Rivera-Arreba, 2017). All relevant wave parameters are listed in Table 5.11. As described in section 2.2 the wave theory that was used to generate the waves is the Fenton Stream Function.

	f [Hz]	T[s]	H[m]	λ [m]	$\frac{d}{gT^2}$	$\frac{H}{gT^2}$	Wave theory CFD
full-scale	0.0575	17.4	3	468.4	0.0673	0.00101	Stream function
model scale	0.406	2.46	0.06	9.37	idem	idem	Stream function

Table 5.11: Wave properties for regular wave with period $T = 17.4$ s (full-scale).

5.5.1. Spatial Domain

In order to prevent significant effects from wave reflections, the length of the domain in x-direction has been increased up to 22 m (see Table 5.5). Note that this is significantly longer than the domain length for smaller wave periods. Since the wave height also increased significantly compared to the previous cases that were discussed, the number of cells per wave length was increased from 50 to 100 p.p.w.l. In order to reduce the computational effort, the cell size increases linearly in the x-direction up to twice its original size after 1.12 m downstream the center of the structure. The cell size of the background mesh is stated in Table 5.12

Furthermore, it should be noted that for the case with heave plate and without movement of the structure, the mesh refinement around the water surface was 6 instead of 10 p.p.w.h.

Direction	Domain length	Number of cells	Cell size δ
x	22 m	171	9.28 cm (~ 100 p.p.w.l, increasing downstream structure)
y	4 m	43	9.30 cm (~ 50 p.p.w.l.)
z	5 m	115	water surf.: 0.060 cm (~ 10 p.p.w.h.) other: 9.44 cm (~ 100 p.p.w.l.)

Table 5.12: Size of the background mesh for wave period $T = 17.4$ s. Cell size is expressed both in centimeter (cm) and in points per wave length (p.p.w.l.) or points per wave height (p.p.w.h.)

5.5.2. Wave Height and Transient Regime

Like in the before mentioned case studies, the wave height increases closer to the structure. As illustrated by Figure A.14, the wave height increases by more than 70%. However, it should be noted that the increases in wave height is significantly smaller for the case where the structure is fixed.

As illustrated by Figure A.16 and Figure A.17, showing the moving mean and the amplitude of the force over time, the simulations tend to reach a relatively steady-state after circa $8t/T$, therefore the transient zone was defined up to this point.

5.5.3. Force and Displacement of the Structure

The heave displacement in Figure 5.9 and Figure 5.10 clearly indicates that the displacement of the structure, both with and without heave plate, is relatively high for the $T = 17.4$ s wave. The column without heave plate oscillates with an amplitude approximately equal to the wave amplitude since it is sufficiently far away from the natural period. However, for the structure with heave plate the 17.4 s wave is relatively close to the natural period, which explains why this structure is excited more heavily.

From the time series of the heave force (Figure A.19), one can see that the heave force for both structures, with and without heave plate, has a phase difference of $0.5t/T$ between the static and the dynamic case. Also in Figure 4.3 it can be seen that the phase of the dynamic cases are in anti-phase with the static cases. As the oscillation amplitude of wave increases, the change in draft of the body starts dominating the wave excitation force and the response of the structure. Both structures (with and without heave plate) have large heave amplitudes, which causes the difference between the static and dynamic cases.

Finally, another remarkable fact when it comes to the heave force, is the small disturbance in the heave force around $t = 0.4T$ and $t = -0.9T$ in the cases where the structure is fixed. This disturbance is clearly visible in both static cases and is consistently measured in all samples, as depicted in Figure A.20. The cause for this has not yet been identified, but could be related to wave splashing as the wave crest or trough hits the structure.

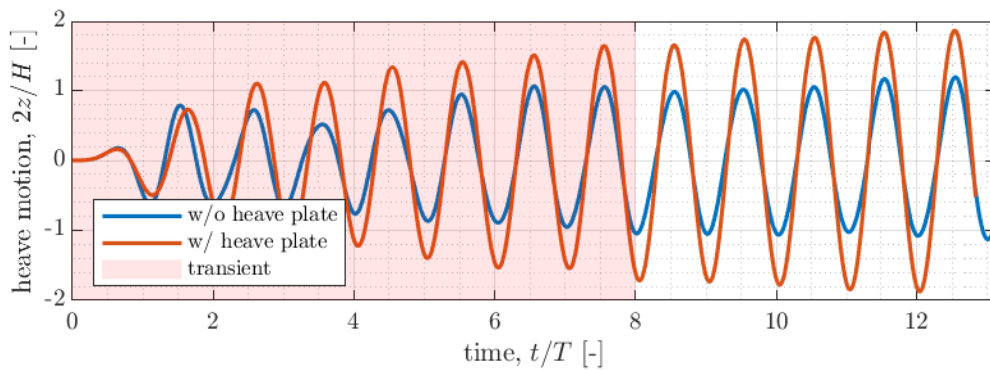


Figure 5.9: Heave motion for the DeepCwind column with and without heave plate, subjected to a wave with period $T = 17.4$ s. The heave motion is normalized by the wave height and the time is normalized by the wave period.

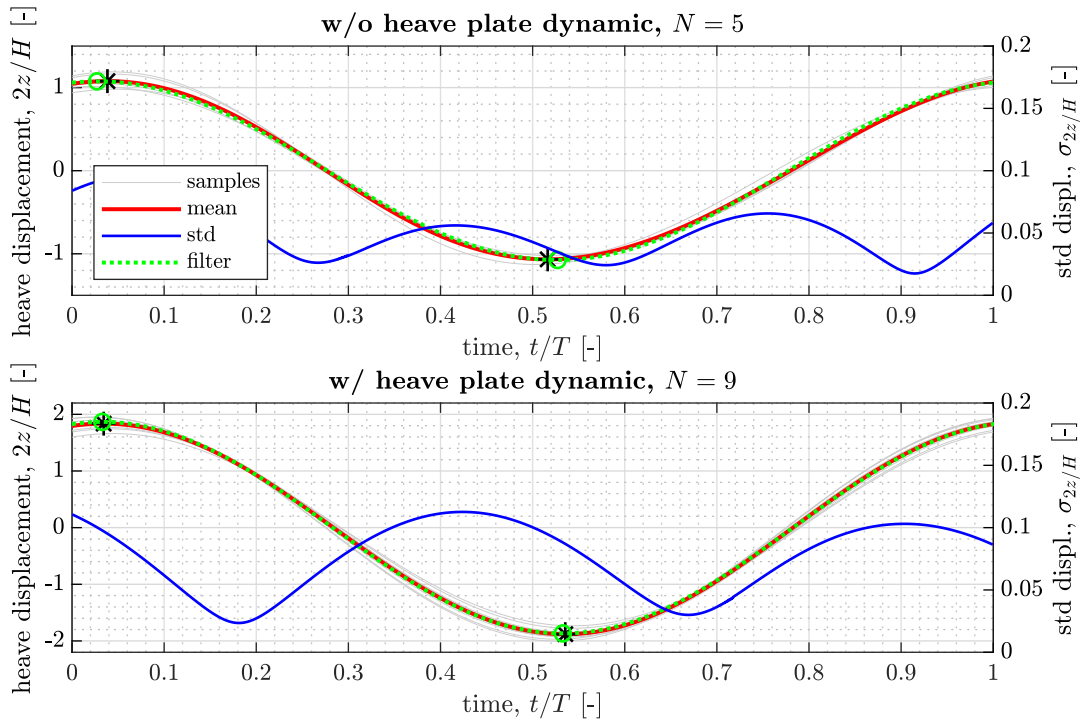


Figure 5.10: Average heave motion cycles for the DeepCwind column with and without heave plate, subjected to a wave with period $T = 17.4$ s. The heave motion cycles are averaged and normalized by the wave height. The time is normalized by the wave period. The number of cycles (samples) that was available for the analysis is denoted by the symbol N .

5.6. Visualisation Vorticity and y^+ -Values

As discussed before, an important difference between the potential flow model and the CFD model is the vorticity, which is not taken into account in the potential flow model. Furthermore, the size of the mesh affects the quality of the simulations significantly, especially close to the structure. Since an unresolved DNS approach has been used throughout this work, the y^+ -value can be used in order to get an impression of to what extent the viscous forces are resolved. Therefore, this section presents visualisations of both the vorticity and the y^+ -values. For the sake of conciseness only a selected number of cases has been visualised. Cases with high RAO values have been chosen to visualise as well as instances in time with relatively high vorticity and y^+ -values.

The vorticity of the flow can play an important role in increasing the drag of the structure. It is therefore relevant to study the vorticity of the flow. The vorticity for a selected number of cases is shown in Figure 5.12, Figure 5.11, Figure 5.13 and Figure 5.14. Note that these figures mainly serve as an illustration of the theoretical differences, if one wants to study the forces on the structure more quantitatively, the previous sections are of more use.

In these figures one can clearly see that the vorticity magnitude is relatively high around the edges of the heave plate or column. This probably increases the drag on the structure. The flow of the water is also affected by the incoming waves, which also affects the vorticity. As a consequence, the propagation of the vorticity to areas further away from the structure can not easily be distinguished. Further away from the structure the vorticity effects from the incoming waves start dominating the vorticity values. Also, mixing of the flow induced or affected by the structure and the flow field from the incoming waves occurs.

Furthermore, it can be seen that the vorticity around the water surface tends to be high as well as

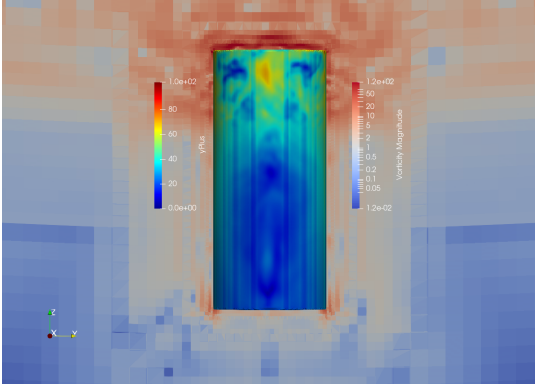


Figure 5.11: Visualisation of the vorticity magnitude and y^+ -values (at the structure's surface). Case: moving column without heave plate with 8 s wave, the snapshot was taken at $t = 29.5T$. The y^+ -colorbar is shown on the left and ranges from 0 to 100, whereas the vorticity colorbar on right ranges from 0 to 120 Hz (model-scale).

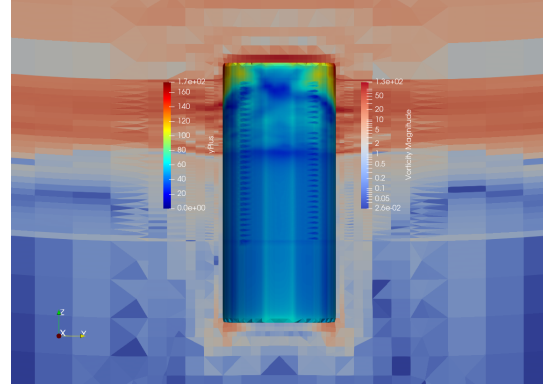


Figure 5.12: Visualisation of the vorticity magnitude and y^+ -values (at the structure's surface). Case: moving column without heave plate with 12.1 s wave, the snapshot was taken at $t = 27.1T$. The y^+ -colorbar is shown on the left and ranges from 0 to 170, whereas the vorticity colorbar on right ranges from 0 to 130 Hz (model-scale).

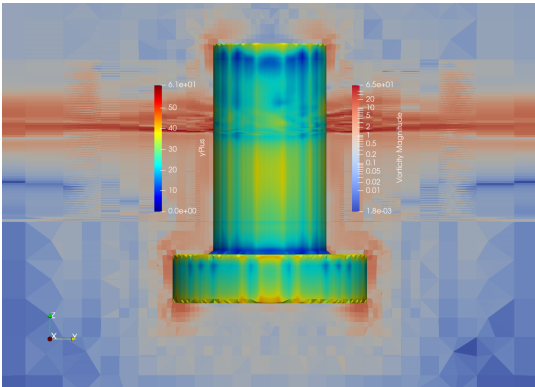


Figure 5.13: Visualisation of the vorticity magnitude and y^+ -values (at the structure's surface). Case: moving column with heave plate with 17.4 s wave, the snapshot was taken at $t = 15.3T$. The y^+ -colorbar is shown on the left and ranges from 0 to 61, whereas the vorticity colorbar on right ranges from 0 to 65 Hz (model-scale).

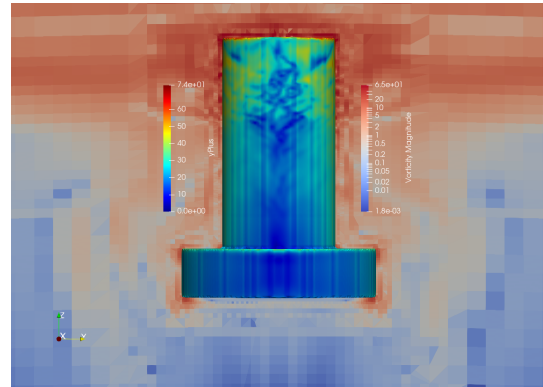


Figure 5.14: Visualisation of the vorticity magnitude and y^+ -values (at the structure's surface). Case: moving column with heave plate with 12.1 s wave, the snapshot was taken at $t = 13.55T$. The y^+ -colorbar is shown on the left and ranges from 0 to 74, whereas the vorticity colorbar on right ranges from 0 to 65 Hz (model-scale).

the area filled with air (on top of the water). Around the water surface kinetic energy is transferred from the waves to the air. Due to the fact that the waveDyMFoam solver assumes the air to be incompressible, the velocities of the air are relatively high. As a consequence the vorticity in this region also tends to be relatively high. In Section 5.8 this is discussed more thoroughly. However, since the mass density of air is much lower (almost 1,000 times lower) than the mass density of the water, the latter dominates the loads on the structure. The vorticity of the air is therefore not a primary concern.

Figure 5.12, Figure 5.11, Figure 5.13 and Figure 5.14 also show the y^+ -values at the structure's surface. The y^+ -value is a non-dimensional number which indicates the size of the cells relative to the size of the viscous sublayer. It is defined as:

$$y^+ = \frac{y u_\tau}{\mu} \quad (5.4)$$

where y , is the absolute distance from the wall; u_τ , is the friction velocity; and μ , is the dynamic viscosity of the fluid.

Generally, if one wants to solve the viscous sublayer the y^+ -value should be $y^+ \ll 5$. Throughout this work however, an unresolved DNS approach has been used, meaning that the viscous sublayer is not completely resolved. As can be seen in the flow visualisations, the the y^+ -values ranged from 0 to ca. 50 for the submerged part of the structure, with a mean around ~ 20 .

It is important to note that the y^+ -values on the top of the structure, where the structure is surrounded by air, are not accurate. Since the yPlus utility in OpenFOAM only accepted the properties of one fluid, the y^+ -values of the air are calculated based on the properties of the water. Consequently, the y^+ -values of the air are highly overestimated.

5.7. Viscous Forces and Pressure Forces

As stated before in Section 3.1.7 the pressure forces and viscous forces have been calculated separately. Throughout this chapter no distinction was made between the pressure forces and viscous forces. All forces that have been presented in this chapter are the total forces. The reason for this is because the viscous forces are virtually negligibly small compared to the pressure forces; the difference in amplitude between these two force components is in the order of a factor $\sim 10^3$.

The fact that an unresolved DNS approach has been used throughout this work, likely caused an underestimation of the viscous forces. The relatively high y^+ -values indicate that the viscous sublayer is not fully resolved. Consequently, the viscous forces can not be computed accurately. This problem can be alleviated by either decreasing the cell size, the downside of which is the fact that it will increase computational time, or by using a turbulence model. Nevertheless, it is expected that the total force from the fluid on the structure is captured sufficiently well. Since the direction of the flow is perpendicular to the heave plate and bottom of the column, it is expected that the pressure component will dominate the fluid forces. Thus, the results are expected to be rather insensitive to the viscous forces. Further research in this field, for example by implementing a turbulence model, could affirm or reject this claim.

5.8. Difficulties and Pitfalls With the Numerical Wave Tank

This section does not present any new results, but instead focuses on difficulties and potential pitfalls that might be relevant for future users of the numerical wave tank. Also, issues mentioned in this section might be helpful while interpreting the presented results. The issues that are covered in this section are in consecutive order:

- wave height-structure interaction;
- reflections;
- poor convergence; and
- air gap.

Firstly, the wave height turned out to be highly affected by the structure. In Rivera-Arreba (2017) a study was performed in order to asses the mesh size that was required in order to capture the wave height sufficiently accurately over the length (x -direction) of the domain. Numerical dissipation can cause the wave height to decrease over domain length. However, using the mesh resolution suggested in Rivera-Arreba (2017) (which in the mesh study lead to difference in wave height of ca. 2% at the x -coordinate of the structure) it was found through the course this work that the measured wave height was differing significantly from the input wave height (see for example Figure A.14.

The presence of the structure seems to affect the wave height in the wave tank itself significantly, especially close to the structure itself. To a certain extent, disturbance of the wave field would be expected. After all, the structure diffracts the wave field. However, also on a fairly large distance (more than five column diameters) parallel to the structure (at $x = 0$ m, $y = 1.5$ m) the wave height was in many cases very much different from the input wave height. This causes problems when the data of the CFD model has to be compared with data from the potential flow model, since this requires scaling by wave height. In this report the author has chosen to use the average wave height obtained from the wave gauge parallel to the structure at $y = 0$ m in order to scale the CFD data. As can be seen from (a.o.) Figure 4.4 and Figure 4.5, which depicts the RAO, this gives data points are very close to the potential flow solution. Therefore, this method for obtaining the wave height seems to give reliable results. Nevertheless, it is obviously unwanted to base the correctness of this method on a comparison with a model that shall be compared with the same data. It is likely that the limited width (y -direction) of the domain causes the disturbances in the wave height, even at fairly large distances from the structure. Therefore, it would be recommended to carry out an analysis of the development of the wave height using a potential flow model with limited domain with as well. A comparison with such a model would give more insight into the disturbance of the wave height in the numerical wave tank. On a side note, the reader shall be informed that the wave gauge utility of the waves2Foam toolbox turned out to be very sensitive to problems with the moving mesh. As a consequence, no wave height data could be obtained for two simulations that were carried out (see Table 5.7).

Secondly, issues with wave reflections were discovered. Especially in the heave decay tests this caused disturbance of the data. The inlet and outlet (see Figure 3.1) of the domain were equipped with a relaxation zone, highly reducing the effect of reflections. However, for waves traveling in y -direction no relaxation zone was provided. Consequently, the motion amplitude of the heave decay test was affected. For the simulations with incident waves, a similar effect from the reflective boundaries is to be expected. However, in these cases the incident wave dominates the surface elevation.

Another issue that occurred was poor convergence of the PIMPLE algorithm. At some instances one can see spikes in the data that was presented in this section. Even though most of the spikes were filtered out while processing the data, some still remain. These spikes are due to bad convergence at some time instances whereas the settings of the PIMPLE algorithm forced the calculation to continue nevertheless (see Section 3.1.3). In all instances presented in this report, the software overcame this issue by reducing the time step and having better convergence performance in the following time steps. However, throughout the course of this work, it was discovered that the software is quite sensitive to small changes in the case settings. Many times the simulations had to be changed slightly in order to improve convergence performance.

Furthermore, the air on top of the water can cause problems. Firstly, the waveDyMFoam solver assumes incompressible fluids. This causes relatively high velocities in the air, induced by the incoming waves. The time steps in OpenFOAM were automatically adjusted based on the Courant–Friedrichs–Lewy condition:

$$CFL = \frac{u\Delta t}{\Delta x} \leq CFL_{max}, \quad (5.5)$$

where u , is the velocity of the fluid; Δt , is the time step; and Δx is the cell size in the direction under consideration.

Due to the relatively high air velocities, in some cases the air was the limiting factor for the time step. This slows down the simulation, whereas the forces of the air on the body are not that interesting, as they are much smaller than the forces from the water (low mass density of air). Secondly, one should take into account that the movement of the mesh causes the cells around the structure to deform. The air gap should be sufficiently high in order for the cells not to deform too much.

6

Comparison Potential Flow and CFD Results

In this chapter the results from the potential flow theory model (WAMIT) and the Navier-Stokes solver (OpenFOAM CFD model) are compared. Some of the figures in this chapter have previously been shown in Chapter 4 and are again included in this chapter in order to improve the ease of reading.

6.1. RAO and Wave Excitation Forces

The first thing that can be noticed when comparing the potential flow (WAMIT) data with the Navier-Stokes solver (CFD) data, is that the RAO values are very similar. As can be seen in Figure 6.1 and Figure 6.2 this is especially the case when it comes to the heave amplitude. In Chapter 4 and Chapter 5 it was explained that the wave cancellation period around $T = 12.75$ s causes a minimum in the RAO of the column with heave plate around this period. It was also mentioned that the drag forces which are, in contrast to the potential flow model, taken into account in the CFD model cause a slightly higher heave amplitude for the CFD case.

The heave phase $\epsilon_{z\zeta}$ is slightly more off, but nevertheless very similar to the potential flow results. The drag force, which is in anti-phase with the displacement could push the phase somewhat towards a higher value and might be a possible explanation for the offset of the heave phase.

The wave excitation forces, for the CFD simulations determined based on the so-called 'static' simulations, are also fairly similar (see Figure 6.3). The most significant difference in wave excitation force is found for the column with heave plate and wave period $T = 12.1$ s. where the wave excitation force from the CFD model is approximately double the value obtained with the potential flow model. However, a logical explanation for this difference can be found based on the wave cancellation period (Section 2.9). For the wave period $T = 17.4$ s the potential flow and CFD results are at most 6% off. In the case of $T = 8$ s wave the differences are similar to the 17.4 s wave for the column without heave plate: the CFD data gives a force amplitude almost 6% higher than the potential flow model.

Figure 6.3 also indicates that the phase of the wave excitation force calculated with CFD (CFD stat) for the column with heave plate deviate significantly from the potential flow phase. It is exactly these data points that belong to the cases where it was found that the heave force has local maxima and minima. As explained in Chapter 5 wave cancellation allows for the drag loads to dominate the

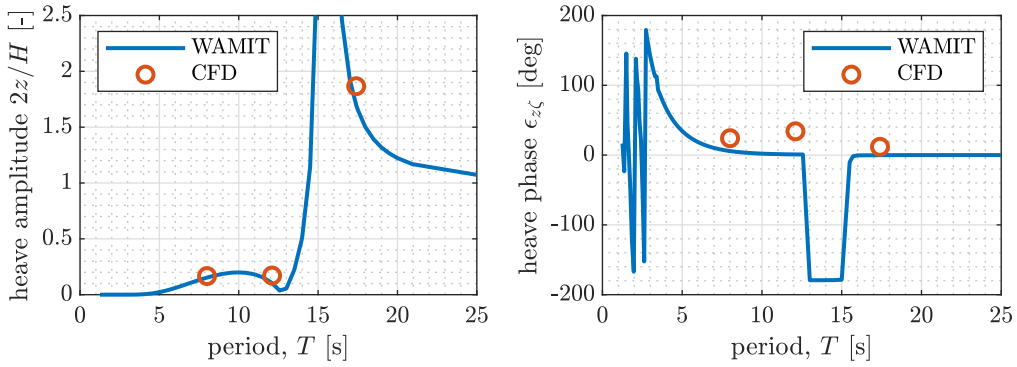


Figure 6.1: Response Amplitude Operator (RAO) and phase characteristic for the DeepCwind column with heave plate.

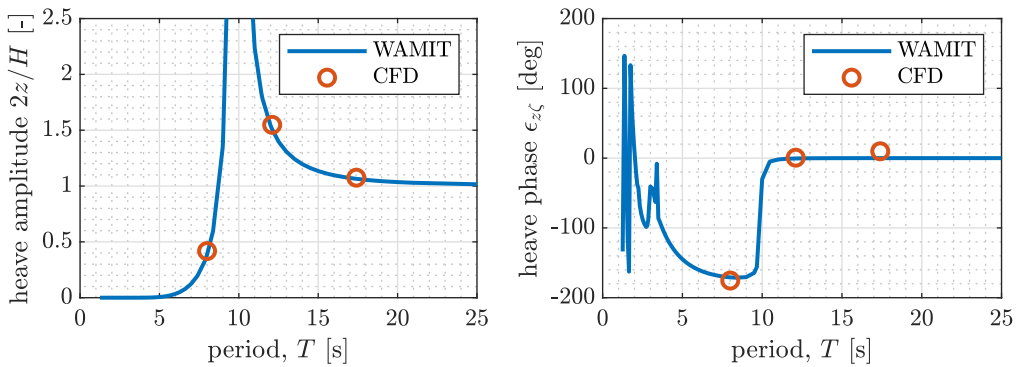


Figure 6.2: Response Amplitude Operator (RAO) and phase characteristic for the DeepCwind column without heave plate.

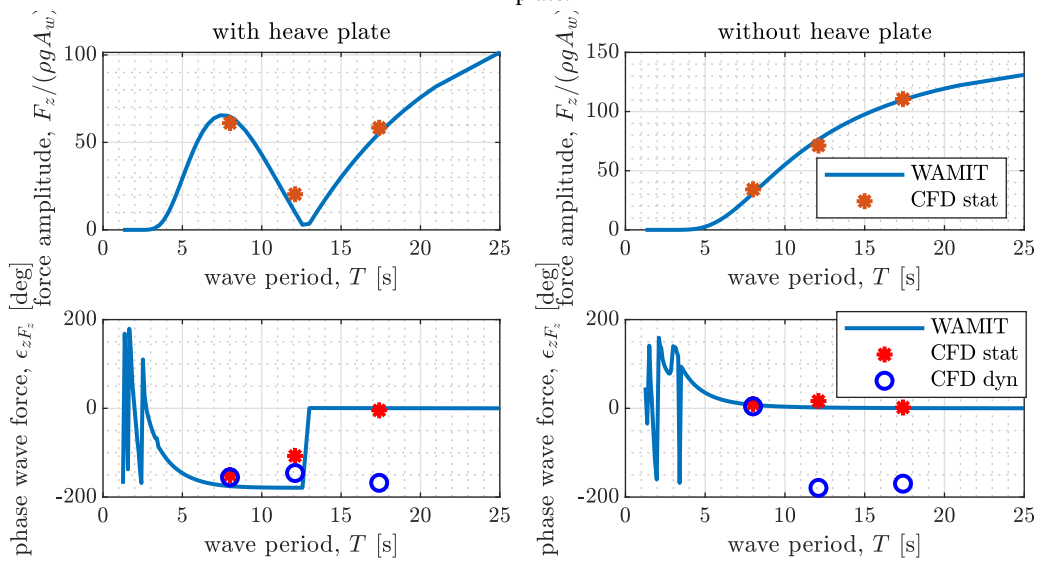


Figure 6.3: Wave excitation force amplitude and wave excitation force phase. The WAMIT results are obtained with directly from the potential flow model WAMIT, whereas the CFD-results are obtained from the results presented in Chapter 5. Note that the 'static' case refers to a fixed body, whereas the 'dyn' case refers to a moving body in heave. The CFD-results have been scaled to full-scale size and non-dimensionalised with the wave amplitude A_w , water density ρ and gravitational acceleration g .

wave force at $T = 12.1$ s, causing a phase shift. At the $T = 8$ s wave the wave force has two peaks that are almost equal to each other with the lower one around $0.5T$, yielding a phase shift of 180° (see Figure A.10). As stated in Section 5.4, the two peaks are caused probably by the negative amplitude

of the wave force on one hand and the drag force on the other hand. A more in-depth analysis on the cause for these local maxima and minima is provided in Chapter 5.

6.2. Natural Period

The CFD model indicated an increase of the natural period from $T_n = 9.8$ s to $T_n = 15.2$ s due to the addition of the heave plate. This yields a 55% increase. Based on the increased mass and added mass obtained with the potential flow model, the expected increase of the heave natural period can be calculated based on the natural frequency $\omega_n = \sqrt{\frac{c}{m+a}}$. Since the restoring spring coefficient c remains unaffected by the addition of the heave plate, the expected change in natural period can be calculated based on the change in mass and added mass $m + a$. Thus, the potential flow model indicates a 56% increase of the natural period. As one can see in Figure 6.2 and Figure 6.1 the RAO shows a similar increase of the natural period. Note that it has been assumed that the system is lightly damped and therefore the damped natural frequency $\omega_0 \approx \omega_n$.

As mentioned in Section 5.1, the damping at the natural period is dominated by the viscous damping. Especially for the column with heave plate, where the viscous damping takes up about 98% of the damping coefficient κ .

7

Conclusions and Recommendations

In this thesis, the hydrodynamic response of a single column of similar to the DeepCwind floater has been studied. The results from a fully nonlinear Navier-Stokes solver (CFD) at specific wave periods have been compared with the results from a potential flow theory model. The response of the column has been studied both with and without heave plate. Furthermore, the CFD model was used in order to simulate the column under wave loads while it was able to move freely in heave direction and while it was constrained in all degrees of freedom. Thus, the wave excitation forces, the response amplitude operator (RAO) and the phase characteristics have been obtained, both based on the CFD model and the potential flow model. In the following the conclusions and recommendations from this study are presented.

7.1. Conclusions

In order to answer the two main research questions, four sub-questions have been defined:

1. *How is the wave field in the numerical wave tank affected by the presence of the structure?*
2. *How do the wave excitation forces of a column with and without heave plate obtained with a potential flow theory based model compare to the wave excitation forces obtained with a fully nonlinear Navier-Stokes numerical wave tank?*
3. *How does the Response Amplitude Operator (RAO) of a column with and without heave plate obtained with a potential flow theory based model compare to the RAO obtained with a fully nonlinear Navier-Stokes numerical wave tank?*
4. *How much does the heave damping at the natural period increase due to the addition of a heave plate to the single column?*

The latter two sub-questions have been extensively discussed in Chapter 6, where the CFD results are compared with the results from the potential flow model. Based on this comparison the following conclusions can be drawn:

- the wave field of the numerical wave tank is affected significantly by the presence of the structure, the wave height at 1.5 m parallel to the structure seems to be a good prediction of the 'actual' wave height experienced by the structure;

- the wave excitation forces obtained with the potential flow model and the CFD model are both in agreement with each other;
- the response amplitude operator obtained with the potential flow model and the CFD model are both in agreement with each other;
- close to the wave cancellation period, the potential flow model tends to underestimate the response amplitude and the wave excitation forces;
- the (damped) natural period obtained with the CFD model and the potential flow model are in agreement with each other;
- the damping at the natural period is dominated by the viscous damping, especially for the column with heave plate; and
- the amplitude and phase of the wave excitation force obtained with the CFD model and the potential flow model follow the same trend, deviations can be explained based on assumptions in the potential flow model.

The effect of the structure on the wave field is addressed in Chapter 5. As mentioned in Section 5.8, the presence of the structure seems to affect the wave height significantly. For future studies in this field it would be recommended to investigate the effect of the limited domain width and the presence of the structure using a potential flow model or a CFD model with the same mesh, but without the structure.

Using these insights, the main research questions can be answered:

- **How does a potential flow theory based model compare to a fully nonlinear Navier-Stokes numerical wave tank when applied to a single column with and without heave plate?**
 - The RAO, phase characteristic and wave excitation forces from the potential flow model and the CFD model are generally in agreement with each other.
- **How do the heave plates affect the (heave) dynamics of single column?**
 - The linear damping coefficient is increased by a factor 1.5 due to addition of the heave plate.
 - The (damped) natural period of the floater increases from ca. $T_n = 9.8$ s to $T_n = 15.2$ s due to addition of the heave plate. A similar increase is estimated based on the potential flow model's increases in mass and added mass.
 - Wave cancellation effects can be distinguished around $T_c = 12.25$ s due to addition of the heave plate.

In other words, based on the results presented in this report, valuable insights have been obtained into the hydrodynamic response of a column with heave plate. Moreover, based on a comparison between a potential flow model and a CFD model, the added value of CFD in the design process of similar structures is evaluated.

The main effect from the heave plate on the dynamic response of the structure is the increase of the heave natural period. This increase follows from the increase of the mass of the structure (by ca. 58%), but also from the increase of the added mass. The latter increased by a factor 6.55 at the heave natural period. The effect from the heave plate on the radiation damping is less apparent, since

the damping plays a minor role in the structure's response. At the natural period of the structure the linear damping coefficient ($\kappa = \frac{b}{b_{cr}}$) increases with approximately 50%. The viscous damping plays an important role in the damping at this wave period. Due to the higher damping ratio for the structure with heave plate, a lower excitation due to waves at the natural period is expected. Finally, heave cancellation effects were observed for the column with heave plate around $T_c \approx 12.75$ s.

In this report it is shown that the potential flow model gives an accurate idea of the response of the column with and without heave plate. Even though viscous effects of the flow contribute significantly to the damping of both structures, the response is hardly affected as the total damping remains relatively low. Under specific circumstance, however, the damping is expected to play a more dominant role in the response of the structure. Therefore, Section 7.2 discusses a number of recommendations for circumstances under which the added value of the CFD model is expected to be higher. Nevertheless, for a more general idea of the response of the column with and without heave plate, a potential flow model is recommended due to its significantly lower computational costs.

7.2. Recommendations

For future research, a number of recommendations are presented in the following. These recommendations can be categorized into two groups: recommendations aimed at further investigating or improving the validity of the CFD model used throughout this work and recommendations for simulations where the added value of the CFD model is expected to be higher.

With regards to the first category of recommendations, it is recommended to *implement a turbulence model* in the CFD model. Since the unresolved DNS approach does not fully resolve the viscous sublayer, the viscous forces are currently underestimated. As explained in Section 5.7, it is expected that the pressure forces will remain the dominating force. Nevertheless, implementation of a turbulence model could help to verify this statement. Another possibility for calculating the viscous forces more accurately is to decrease the cell size below $y^+ < 5$. However, this will increase the computational time significantly, implementation of a turbulence model is therefore recommended.

Furthermore, it is recommended to investigate the *effect of the domain size* of the CFD model, especially since the potential flow model that was used assumed an infinite domain size. It is recommended to either increase the width of the CFD domain and investigate any differences in the results or to use a potential flow model with a similar width as the CFD model. Using the latter approach will also allow for a *comparison of the wave height* at various points in the domain, which is also a topic which deserves extra attention. As was shown in Chapter 5, the wave height varies quite significantly over the length of the domain. It is expected that, amongst others, the limited domain width has affected the wave height significantly.

Something else that could be done in order to verify the validity of the CFD model is a *mesh convergence study*. As mentioned before, the mesh size used throughout this work was based on Rivera-Arreba (2017) and Bruinsma (2016) who performed a mesh convergence study for similar type of structure. However, as indicated in Section 5.4, the suggested refinement around the water surface was increased throughout this work, since the suggested mesh size seemed to be insufficient. Therefore, a mesh convergence study focusing on the mesh size around the water surface specifically is recommended.

With regards to the second category of recommendations, it is recommended to investigate the response of the column with(out) heave plate under other conditions. As concluded in this report, the potential flow model describes the response of the column with and without heave plate rather well

due to the minor effect of the damping on the structure's response. However, under some circumstances the effect of the damping is expected to be more important. Consequently, the results from the potential flow model and the CFD model are expected to be higher. This is expected to be the case for the following conditions:

- regular waves at heave natural period;
When the incoming waves have a period equal to the heave natural period of the structure, heave resonance will occur. In this case the damping will dominate the excitation of the structure. Potential flow theory does not give a reasonable estimate of the excitation of the structure under heave resonance conditions.
- regular waves at heave cancellation period; and
At the heave cancellation period, the wave excitation forces are zero according to the potential flow model (only applicable for the column with heave plate). However, taking into account the viscous effects of the flow, the wave excitation forces are not expected to be zero in the CFD model. Therefore, it would be interesting to investigate the difference between the potential flow and CFD model at this wave period. The 12.1 s wave, which was part of the analysis of this work, is close to but not exactly at the wave cancellation period.
- extremely steep or breaking waves.
For very steep waves the velocities are expected to be higher, which will likely increase the drag forces on the structure. Potential flow theory does not take into account the steepness of the waves. In general, as the wave becomes more steep, the linearity assumption from the potential wave theory model becomes more problematic and the CFD model is expected to give more trustworthy results. Note that the 8 s wave used throughout this work is already relatively steep. While increasing the wave steepness, the waves will eventually reach the breaking limit. The potential flow model is not able to assess breaking waves, whereas the CFD model is.

Furthermore, it was demonstrated in Section 5.1 that the viscous effects dominate the response during the heave decay test. For even higher initial displacements, the importance of the viscous effects will likely increase even further.

Bibliography

- Anderson, J. D., Degroote, J., Degrez, G., Dick, E., Grundmann, R., and Vierendeels, J. *Computational fluid dynamics: An introduction*. Springer Berlin Heidelberg, 2009. ISBN 9783540850557. doi: 10.1007/978-3-540-85056-4.
- Bachynski, E. E. Fixed and Floating Offshore Wind Turbine Support Structures. In *Offshore Wind Energy Technology*, pages 103–142. John Wiley & Sons Ltd, 2018.
- Berberović, E., Van Hinsberg, N. P., Jakirlić, S., Roisman, I. V., and Tropea, C. Drop impact onto a liquid layer of finite thickness: Dynamics of the cavity evolution. *Physical Review E - Statistical, Nonlinear, and Soft Matter Physics*, 79(3):036306, 3 2009. ISSN 15393755. doi: 10.1103/PhysRevE.79.036306.
- Bruinsma, N. *Validation and Application of a Fully Nonlinear Numerical Wave Tank (MSc thesis)*. 2016.
- Cebeci, T., Platzer, M., Chen, H., Chang, K.-C., and Shao, J. P. Panel Methods. In *Analysis of Low-Speed Unsteady Airfoil Flows*, chapter Panel Meth, pages 31–48. Springer Berlin Heidelberg, Berlin, Heidelberg, 2005. doi: 10.1007/3-540-27361-1_{_}3. URL http://link.springer.com/10.1007/3-540-27361-1_3.
- Cengel, Y. A. and Cimbala, J. M. *Fluid mechanics : fundamentals and applications*. McGraw-Hill Education, New York, NY, 4th editio edition, 2017. ISBN 1259696537.
- Danko, P. First US Floating Wind Turbine Launches In Maine | EarthTechling, 2013. URL <https://earthtechling.com/2013/05/maine-floating-turbine-in-the-water/>.
- DNV. Design of Floating Wind Turbine Structures. Technical report, Det Norske Veritas, 2013.
- DNV Software SESAM. Wadam (version V4.6-03), 2013. URL <https://www.dnvgl.com/services/frequency-domain-hydrodynamic-analysis-of-stationary-vessels-wadam-2412>.
- Dunwoody, A. and Vandiver, J. Wave-Induced Damping of Offshore Structures. In *Offshore Technology Conference*. Offshore Technology Conference, 4 1987. doi: 10.4043/5412-MS. URL <http://www.onepetro.org/doi/10.4043/5412-MS>.
- Equinor. Hywind Scotland - the world's first floating wind farm - YouTube, 2017. URL <https://www.youtube.com/watch?v=vKHJfuuYi0k>.
- Fenton, J. D. The numerical solution of steady water wave problems. *Computers and Geosciences*, 14(3):357–368, 1988. ISSN 00983004. doi: 10.1016/0098-3004(88)90066-0.
- Fenton, J. D. Nonlinear Wave Theories. *The Sea*, 9: Ocean E:Edited by B. Le Méhauté and D.M. Hanes, Wiley, New, 1990.
- Fenton, J. D. A FIFTH-ORDER STOKES THEORY FOR STEADY WAVES. *Journal of Waterway, Port, Coastal and Ocean Engineering*, 111(2):216–234, 1985.

- Ferziger, J. H. and Perić, M. *Computational Methods for Fluid Dynamics*. Springer Berlin Heidelberg, 2002. doi: 10.1007/978-3-642-56026-2.
- Fine, R. A. and Millero, F. J. Compressibility of water as a function of temperature and pressure. *The Journal of Chemical Physics*, 59(10):5529–5536, 1973. ISSN 00219606. doi: 10.1063/1.1679903.
- Fuhrman, D. R., Madsen, P. A., and Bingham, H. B. Numerical simulation of lowest-order short-crested wave instabilities. *Journal of Fluid Mechanics*, 563:415–441, 9 2006. ISSN 00221120. doi: 10.1017/S0022112006001236.
- Garrido-Mendoza, C. A. *Hydrodynamic forces on heave plates for offshore systems oscillating close to the seabed or the free surface*. PhD thesis, 2015.
- Garrido-Mendoza, C. A., Thiagarajan, K. P., Souto-Iglesias, A., Bouscasse, B., and Colagrossi, A. Numerical investigation of the flow features around heave plates oscillating close to a free surface or seabed. In *Proceedings of the International Conference on Offshore Mechanics and Arctic Engineering - OMAE*, volume 7. American Society of Mechanical Engineers (ASME), 2014. ISBN 9780791845493. doi: 10.1115/OMAE2014-23818.
- Haslum, H. A. and Faltinsen, O. M. Alternative shape of spar platforms for use in hostile areas. *Proceedings of the Annual Offshore Technology Conference*, 2, 1999. ISSN 01603663. doi: 10.4043/10953-ms.
- Henderson, A. R. and Witcher, D. Floating Offshore Wind Energy — A Review of the Current Status and an Assessment of the Prospects. *Wind Engineering*, 34(1):1–16, 1 2010. ISSN 0309-524X. doi: 10.1260/0309-524X.34.1.1. URL <http://journals.sagepub.com/doi/10.1260/0309-524X.34.1.1>.
- Hirt, C. W. and Nichols, B. D. Volume of fluid (VOF) method for the dynamics of free boundaries. *Journal of Computational Physics*, 39(1):201–225, 1 1981. ISSN 10902716. doi: 10.1016/0021-9991(81)90145-5.
- Holzmann, T. *Mathematics, Numerics, Derivations and OpenFOAM (R)*. Holzmann CFD, release 7. edition, 2019. doi: 10.13140/RG.2.2.27193.36960. URL <https://holzmann-cfd.de/>.
- Jacobsen, N. G. waves2Foam Manual. 9(August):1–74, 2017. URL https://www.researchgate.net/profile/Niels_Jacobsen3/publication/319160515_waves2Foam_Manual/links/5995c1e7aca27283b11b21a2/waves2Foam-Manual.pdf.
- Jacobsen, N. G., Fuhrman, D. R., and Fredsøe, J. A wave generation toolbox for the open-source CFD library: OpenFoam®. *International Journal for Numerical Methods in Fluids*, 70(9):1073–1088, 11 2012. ISSN 02712091. doi: 10.1002/flid.2726. URL <http://doi.wiley.com/10.1002/flid.2726>.
- Journée, J. M. J. and Massie, W. W. *Offshore Hydromechanics*. First edition, 2001.
- Lagrange, J.-L. Mémoire sur la théorie du mouvement des fluides. In *Oeuvres de Lagrange*, chapter Mémoire su, pages 695–748. 1868. URL <http://gallica.bnf.fr/ark:/12148/bpt6k229223s/f697.image>.
- Lee, C.-H. WAMIT Theory Manual. Technical report, Massachusetts Institute of Technology, 1995.
- Lee, C. H. and Newman, J. N. First- and Second-Order Wave Effects on a Submerged Spheroid. *Journal of Ship Research*, 35(3):183, 1991.

- McCormick, M. E. *Ocean engineering mechanics: With applications*, volume 9780521859. Cambridge University Press, 1 2009. ISBN 9780511812309. doi: 10.1017/CBO9780511812309. URL /core/books/ocean-engineering-mechanics/02903943F9E4B09A41640170F2233778.
- Molin, B. On the added mass and damping of periodic arrays of fully or partially porous disks. *Journal of Fluids and Structures*, 15(2):275–290, 2001. ISSN 08899746. doi: 10.1006/jfls.2000.0338.
- Newmark, N. M. A method of computation for structural dynamics. *Journal of the Engineering Mechanics Division*, 85 (EM3):67–94, 1959.
- Rienecker, M. M. and Fenton, J. D. A Fourier approximation method for steady water waves. *Journal of Fluid Mechanics*, 104:119–137, 1981.
- Rivera-Arreba, I. *Computation of Nonlinear Wave Loads on Floating Structures (MSc thesis)*. Number August. 2017.
- Rivera-Arreba, I., Bruinsma, N., Bachynski, E. E., Viré, A., Paulsen, B. T., and Jacobsen, N. G. Modeling of a Semisubmersible Floating Offshore Wind Platform in Severe Waves. *Journal of Offshore Mechanics and Arctic Engineering*, 141(6), 12 2019. ISSN 1528896X. doi: 10.1115/1.4043942.
- Roberts, J. B. Estimation of Nonlinear Ship Roll Damping From Free-Decay Data. *Journal of Ship Research*, 29(2):127–138, 1985. ISSN 00224502.
- Robertson, A., Jonkman, J., Wendt, F., Goupee, A., and Dagher, H. Definition of the OC5 DeepCwind Semisubmersible Floating System. Technical report, 2016.
- Rusche, H. *Computational Fluid Dynamics of Dispersed Two-Phase Flows at High Phase Fractions*. PhD thesis, Imperial College of Science, Technology & Medicine, 2002.
- Sarpkaya, T. S. *Wave forces on offshore structures*, volume 9780521896. Cambridge University Press, 2010. ISBN 9781139195898. doi: 10.1017/CBO9781139195898.
- Selot, F., Fraile, D., and Brindley, G. Offshore Wind in Europe: Key trends and statistics 2018. Technical report, Brussels, Belgium, 2019.
- Steidel, R. F. *An introduction to mechanical vibrations*. Wiley, 1989. ISBN 9780471845454.
- Tao, L., Molin, B., Scolan, Y. M., and Thiagarajan, K. Spacing effects on hydrodynamics of heave plates on offshore structures. *Journal of Fluids and Structures*, 23(8):1119–1136, 11 2007. ISSN 08899746. doi: 10.1016/j.jfluidstructs.2007.03.004.
- Thiagarajan Sharman, K., Robertson, A., and Jared Lewis, N. Heave plate hydrodynamics for offshore wind turbine applications. Technical report, 2019.
- United Nations. The Paris Agreement. URL <https://unfccc.int/process-and-meetings/the-paris-agreement/the-paris-agreement>.
- Wamit Inc. WAMIT (version 6.4), 2006. URL <http://wamit.com/license.htm>.
- WindEurope. FLOATING OFFSHORE WIND ENERGY-A POLICY BLUEPRINT FOR EUROPE FLOATING OFFSHORE WIND ENERGY. Technical report.

A

Results OpenFOAM Simulations

A.1. Wave Period $T = 12.1$ s

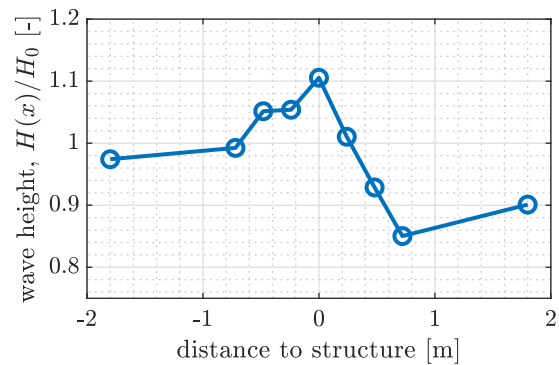


Figure A.1: The average wave height over position in x -direction for wave period $T = 12.1$ s, cell size is 50 p.p.w.l. with refinement of ca. 10 p.p.w.h. around the water surface. The column without heave plate is present and the structure can move freely in heave direction. The wave height is normalized by the prescribed wave height from Table 5.4.

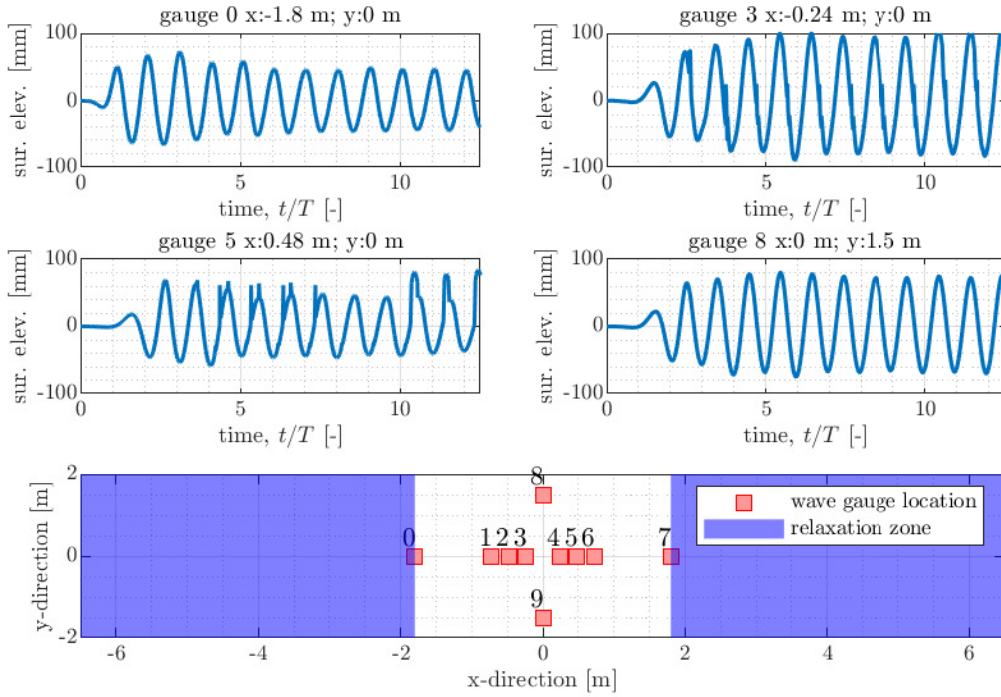


Figure A.2: The wave height at a number of locations in the flow domain for wave period $T = 12.1$ s, cell size is 50 p.p.w.l., without heave plate and the structure moving freely in heave direction. The locations of the wave gauges are indicated in the lowest figure, where the point (0,0) indicates the location of the structure.

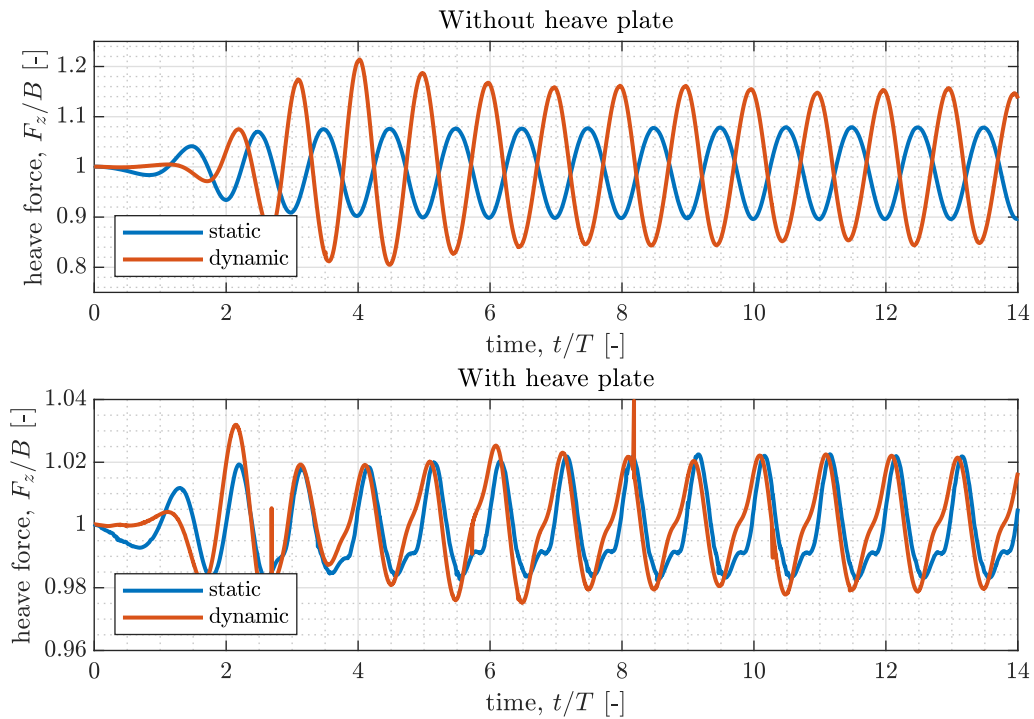


Figure A.3: Heave force time series for the DeepCwind column with and without heave plate, subjected to a wave with period $T = 12.1$ s. The heave force is normalized by the buoyancy and the time is normalized by the wave period.

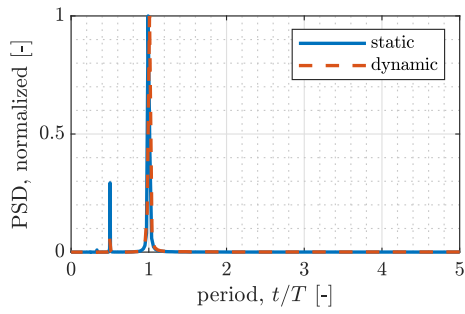


Figure A.4: Power spectral density of the heave force for the column with heave plate subject to a wave period $T = 12.1$ s as a function the period. The power spectral density has been normalized by its maximum value, whereas the period has been normalized by the wave period.

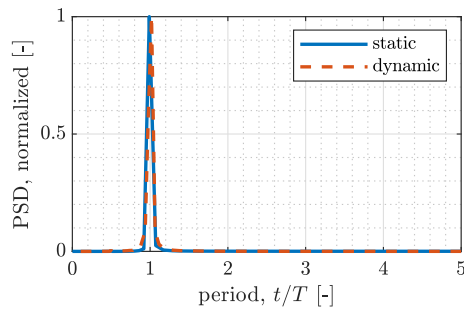


Figure A.5: Power spectral density of the heave force for the column without heave plate subject to a wave period $T = 12.1$ s as a function the period. The power spectral density has been normalized by its maximum value, whereas the period has been normalized by the wave period.

A.2. Wave Period $T = 8$ s

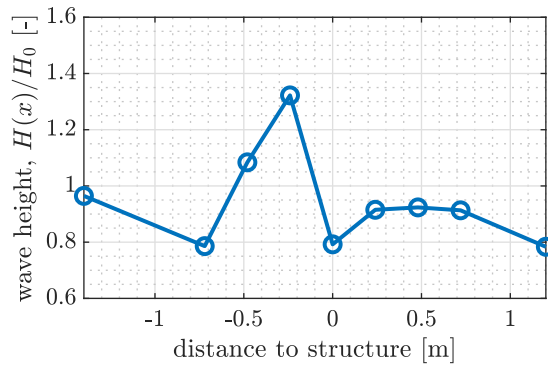


Figure A.6: The average wave height over position in x-direction for wave period $T = 8$ s, cell size is 50 p.p.w.l., without heave plate and the structure moving freely in heave direction. The wave height is normalized by the prescribed wave height H_0 from Table 5.8.

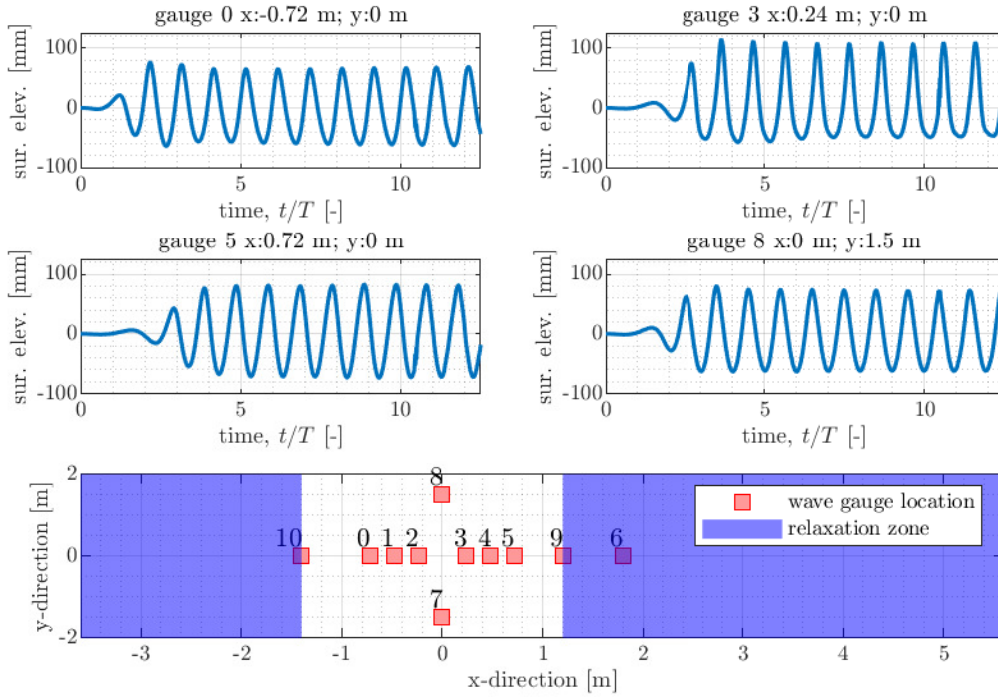


Figure A.7: The wave height at a number of locations in the flow domain for wave period $T = 8$ s, cell size is 50 p.p.w.l., without heave plate and the structure moving freely in heave direction. The locations of the wave gauges are indicated in the lowest figure, where the point (0,0) indicates the location of the structure.

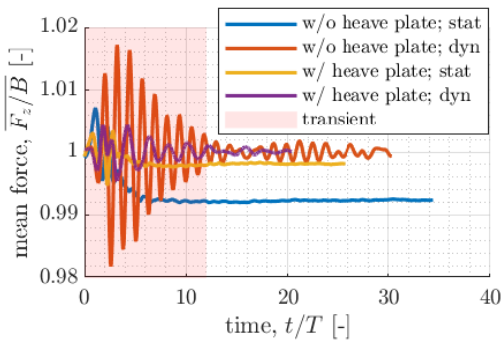


Figure A.8: Moving mean of the heave force normalized by the buoyancy for wave period $T = 8$ s. Width of the window over which the mean was calculated is equal to wave period.

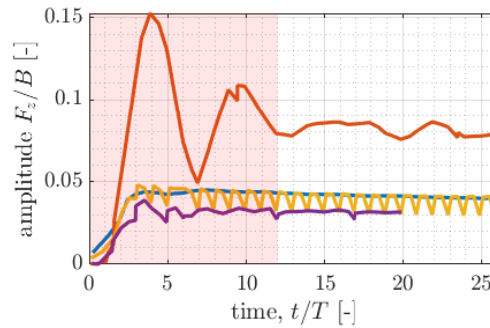


Figure A.9: Time series of the amplitude of the heave force F_z on the structure normalized by the buoyancy B for wave period $T = 8$ s. For the legend refer to Figure 5.2.

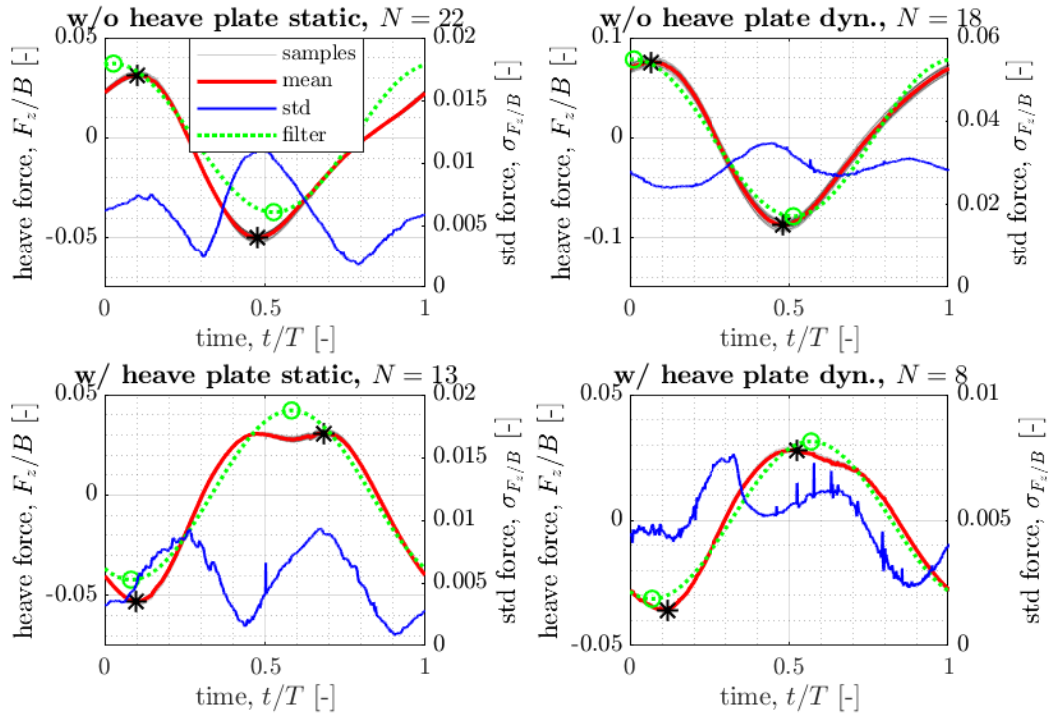


Figure A.10: Average heave force cycles for the DeepCwind column with and without heave plate, subjected to a wave with period $T = 8$ s. The heave force cycles are averaged and normalized by the buoyancy B of the structure. The time is normalized by the wave period. The number of cycles (samples) that was available for the analysis is denoted by the symbol N . The words 'static' and 'dyn.' refer to the fixed and moving column respectively.

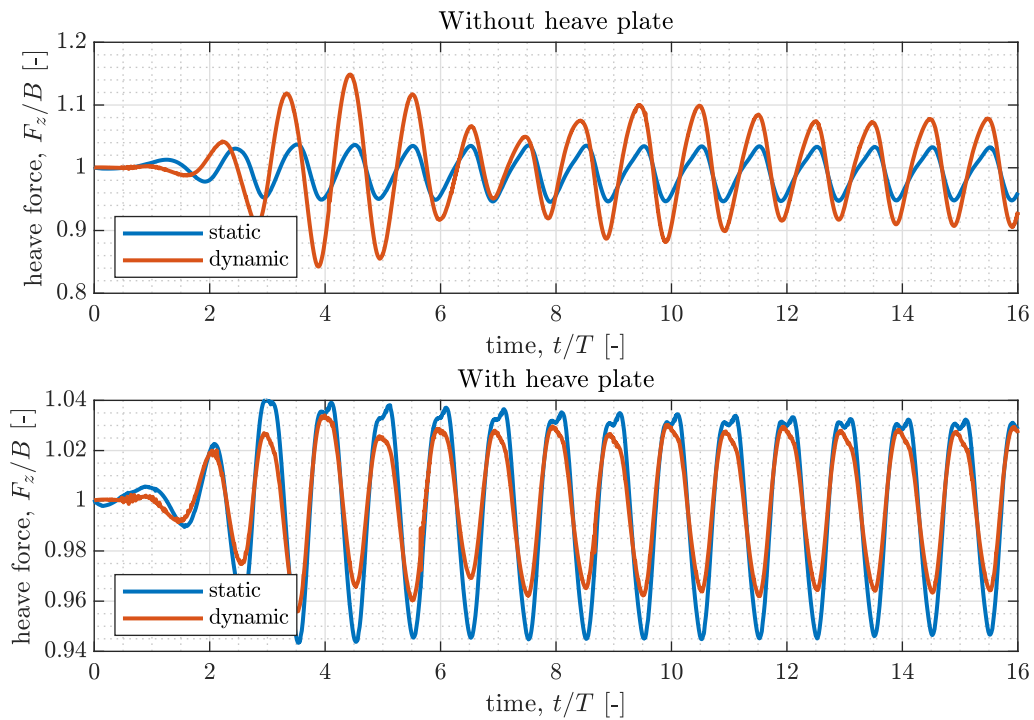


Figure A.11: Heave force time series for the DeepCwind column with and without heave plate, subjected to a wave with period $T = 8$ s. The heave force is normalized by the buoyancy and the time is normalized by the wave period.

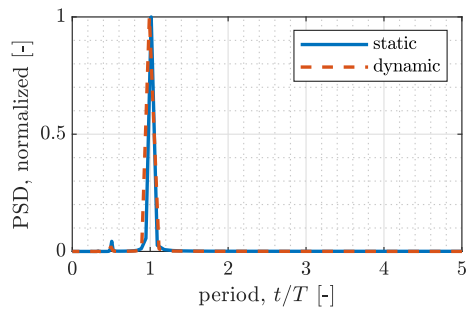


Figure A.12: Power spectral density of the heave force for the column with heave plate subject to a wave period $T = 8$ s as a function the period. The power spectral density has been normalized by its maximum value, whereas the period has been normalized by the wave period.

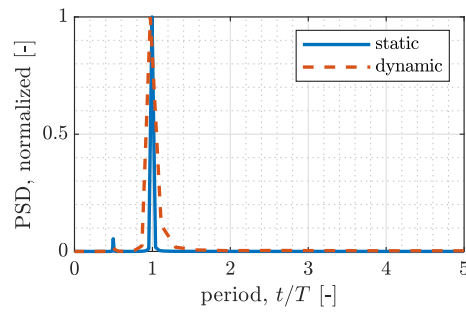


Figure A.13: Power spectral density of the heave force for the column without heave plate subject to a wave period $T = 8$ s as a function the period. The power spectral density has been normalized by its maximum value, whereas the period has been normalized by the wave period.

A.3. Wave Period $T = 17.4$ s

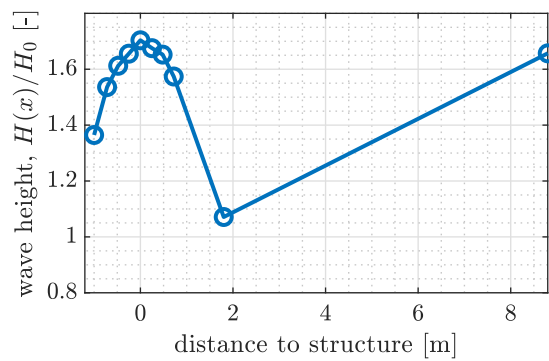


Figure A.14: The average wave height over position in x-direction for wave period $T = 17.4$ s, cell size is 50 p.p.w.l., without heave plate and the structure moving freely in heave direction. The wave height is normalized by the prescribed wave height H_0 from Table 5.11.

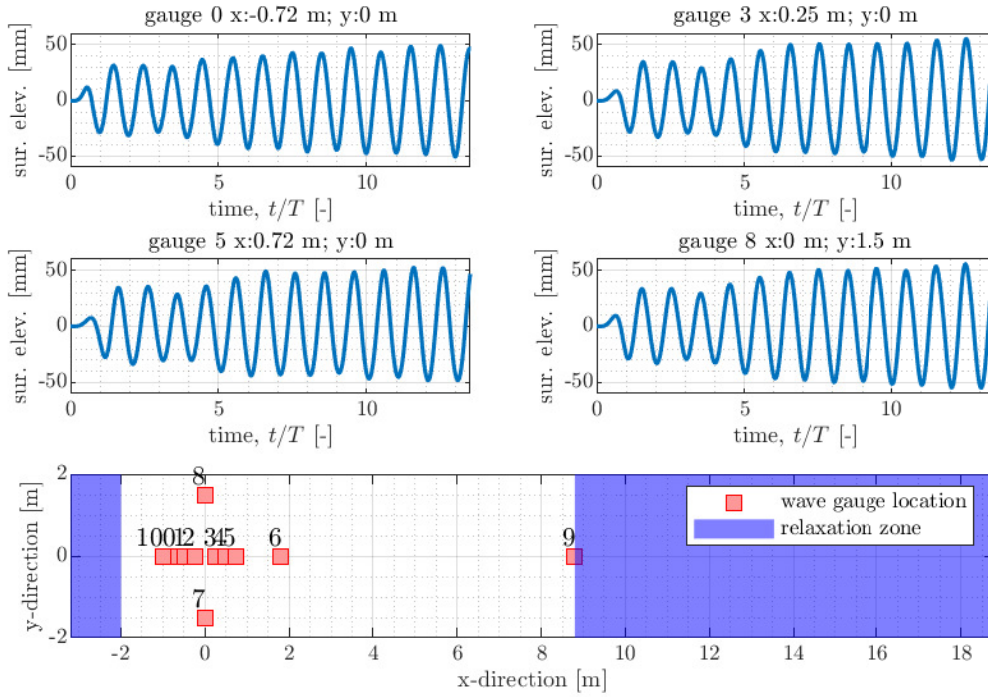


Figure A.15: The wave height at a number of locations in the flow domain for wave period $T = 17.4$ s, cell size is 50 p.p.w.l., without heave plate and the structure moving freely in heave direction. The locations of the wave gauges are indicated in the lowest figure, where the point (0,0) indicates the location of the structure.

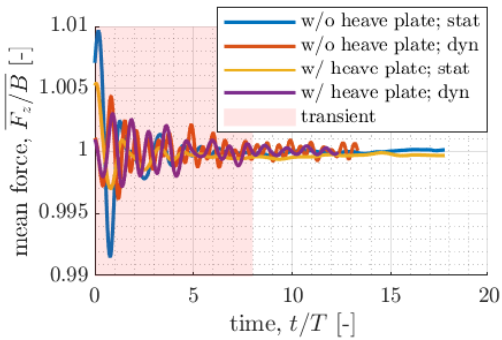


Figure A.16: Moving mean of the heave force normalized by the buoyancy for wave period $T = 17.4$ s. Width of the window over which the mean was calculated is equal to wave period.

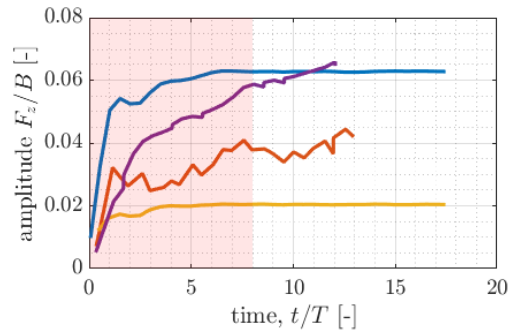


Figure A.17: Time series of the amplitude of the heave force F_z on the structure normalized by the buoyancy B for wave period $T = 17.4$ s. For the legend refer to Figure 5.2.

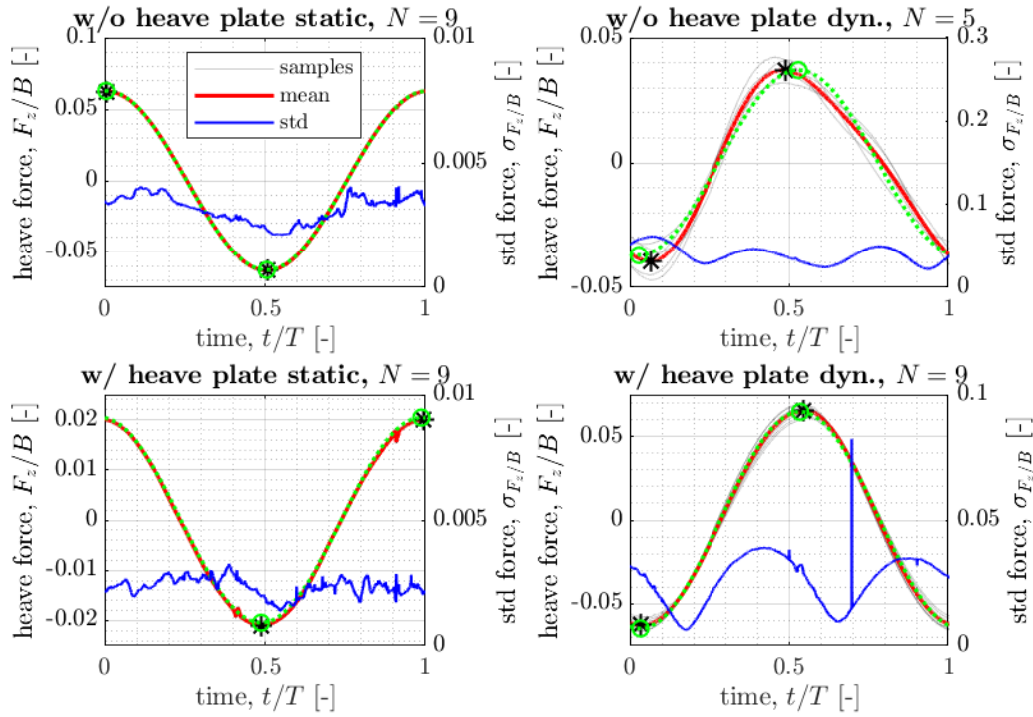


Figure A.18: Average heave force cycles for the DeepCwind column with and without heave plate, subjected to a wave with period $T = 17.4$ s. The heave force cycles are averaged and normalized by the buoyancy B of the structure. The time is normalized by the wave period. The number of cycles (samples) that was available for the analysis is denoted by the symbol N . The words 'static' and 'dyn.' refer to the fixed and moving column respectively.

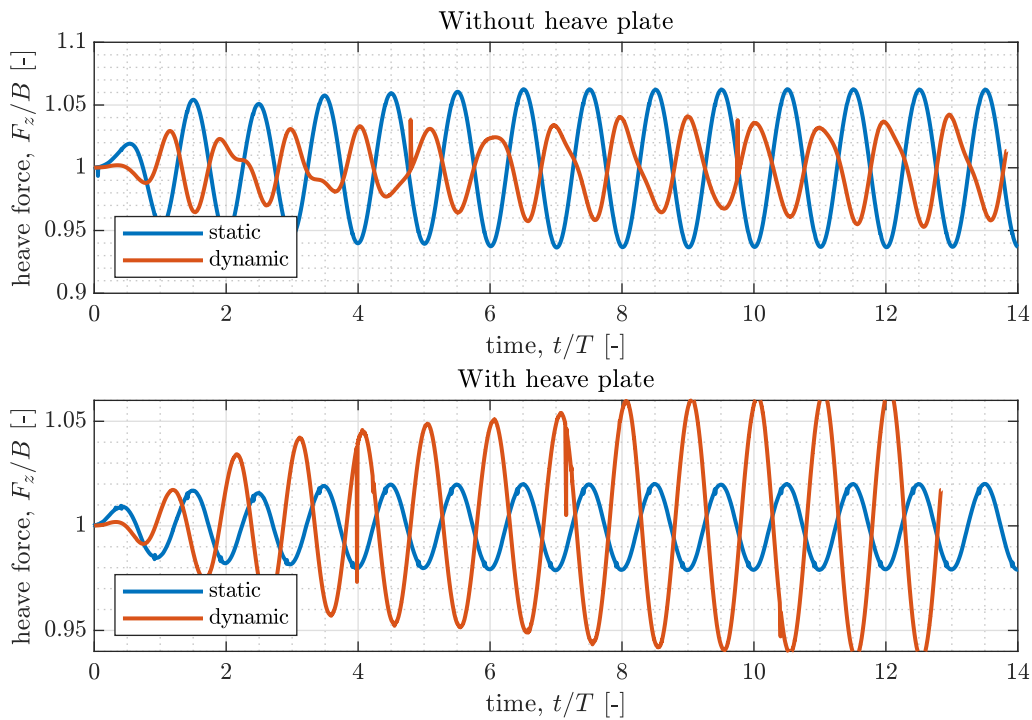


Figure A.19: Heave force time series for the DeepCwind column with and without heave plate, subjected to a wave with period $T = 17.4$ s. The heave force is normalized by the buoyancy and the time is normalized by the wave period.

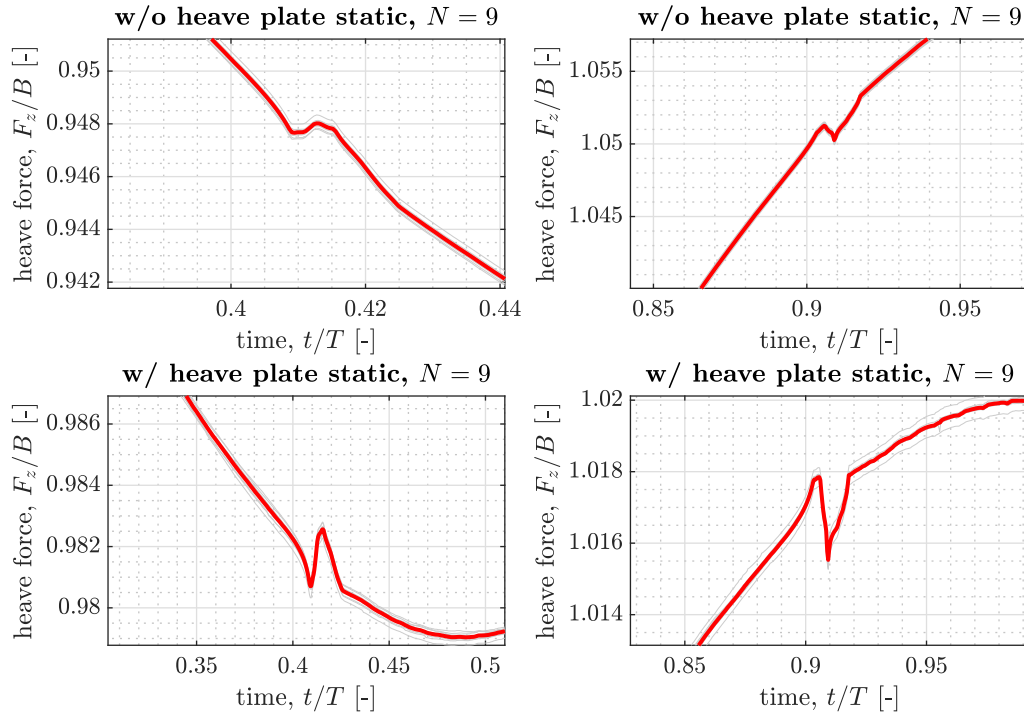


Figure A.20: A detailed view of the disturbances in the heave force for wave period $T = 17.4$ s. The heave force cycles are averaged and normalized by the buoyancy B of the structure. The time is normalized by the wave period. The number of cycles (samples) that was available for the analysis is denoted by the symbol N .

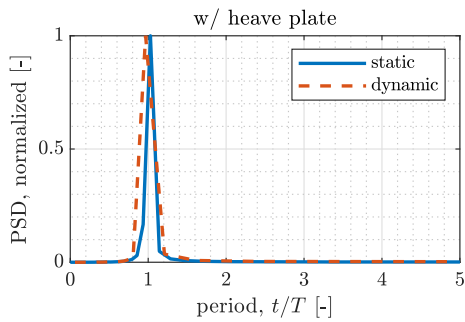


Figure A.21: Power spectral density of the heave force for the column with heave plate subject to a wave period $T = 17.4$ s as a function the period. The power spectral density has been normalized by its maximum value, whereas the period has been normalized by the wave period.

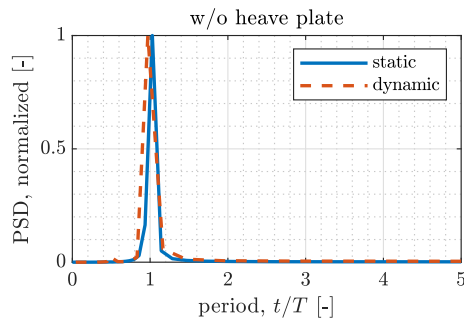


Figure A.22: Power spectral density of the heave force for the column without heave plate subject to a wave period $T = 17.4$ s as a function the period. The power spectral density has been normalized by its maximum value, whereas the period has been normalized by the wave period.

B

OpenFOAM Code

B.1. fvSolution

```
/*----- C++ -----*\
| ===== |
| \ \      / F i e l d      | OpenFOAM: The Open Source CFD Toolbox
| \ \    / O p e r a t i o n | Version: 1.5
| \ \  /   A n d             | Web:      http://www.OpenFOAM.org
| \ \ /    M a n i p u l a t i o n |
|
\*-----*\
FoamFile
{
    version      2.0;
    format       ascii;
    class        dictionary;
    object       fvSolution;
}
// * * * * * //

solvers
{
    "alpha.water.*"
    {
        nAlphaCorr      1;
        nAlphaSubCycles 1;
        alphaOuterCorrectors no;
        cAlpha          1;

        MULESCorr       no;
        nLimiterIter    3;
    }
}
```

```
    solver          PBiCG; //smoothSolver;
    preconditioner  DILU;
    smoother        symGaussSeidel;
    tolerance        1e-8;
    relTol          0;
}

pcorr GAMG
{
    tolerance        1e-4;
    relTol          0.0;

    smoother        DIC;// GaussSeidel;
    nPreSweeps      0;
    nPostSweeps     2;
    nFinestSweeps   2;

    cacheAgglomeration true;
    nCellsInCoarsestLevel 10;
    agglomerator     faceAreaPair;
    mergeLevels      1;
};

pcorrFinal GAMG
{
    tolerance        1e-4;
    relTol          0.0;

    smoother        DIC;// GaussSeidel;
    nPreSweeps      0;
    nPostSweeps     2;
    nFinestSweeps   2;

    cacheAgglomeration true;
    nCellsInCoarsestLevel 10;
    agglomerator     faceAreaPair;
    mergeLevels      1;
};

p_rgh GAMG
{
    tolerance        1e-7;
    relTol          0.0;

    smoother        DIC;// GaussSeidel;
    nPreSweeps      0;
    nPostSweeps     2;
    nFinestSweeps   2;
```

```
    cacheAgglomeration true;
    nCellsInCoarsestLevel 10;
    agglomerator    faceAreaPair;
    mergeLevels    1;
};

p_rghFinal GAMG
{
    tolerance    1e-8;
    relTol    0.0;

    smoother    DIC; // GaussSeidel;
    nPreSweeps    0;
    nPostSweeps    2;
    nFinestSweeps    2;

    cacheAgglomeration true;
    nCellsInCoarsestLevel 10;
    agglomerator    faceAreaPair;
    mergeLevels    1;
};

U PBiCG
{
    preconditioner    DILU;
    tolerance    1e-09;
    relTol    0;
};

UFinal PBiCG
{
    preconditioner    DILU;
    tolerance    1e-09;
    relTol    0;
};

cellDisplacement
{
    solver    GAMG;
    tolerance    1e-10;
    relTol    0;
    smoother    GaussSeidel;
}

cellDisplacementFinal
{
    solver    GAMG;
    tolerance    1e-10;
    relTol    0;
}
```

```
        smoother      GaussSeidel;
    }
}

PIMPLE
{
    momentumPredictor yes;
    nCorrectors      3;
    nNonOrthogonalCorrectors 1;

    nOuterCorrectors 4;
    moveMeshOuterCorrectors true; // Default = false;

    correctPhi true;
}

relaxationFactors
{
    fields
    {
        p_rhg      0.5;
        p_rhgFinal 1;
    }
    equations
    {
        "." 1;
    }
}

// ***** //
```

B.2. fvSchemes

```

/*-----* C++ *-----*/
| ===== |
| \ \      / F i e l d      | OpenFOAM: The Open Source CFD Toolbox
| \ \      / O p e r a t i o n      | Version: 1.5
| \ \      / A n d      | Web:      http://www.OpenFOAM.org
| \ \ /      M a n i p u l a t i o n      |
|
|-----*/
FoamFile
{
    version      2.0;
    format       ascii;
    class        dictionary;
    object       fvSchemes;
}
// * * * * *

ddtSchemes
{
    default Euler;
}

gradSchemes
{
//    default    cellLimited fourth 1;
    default      Gauss linear;
    grad(U)      Gauss linear;
    grad(alpha1) Gauss linear;
}

divSchemes
{
//    default      Gauss linear;
    div(rhoPhi,U) Gauss upwind;
//    div(phi,gamma) Gauss vanLeer;
//    div(rho*phi,U) Gauss MUSCL;
    div((muEff*dev(T(grad(U)))) Gauss linear;
    div(((rho*nuEff)*dev2(T(grad(U)))) Gauss linear;
    div(phi,alpha) Gauss upwind;
    div(phirb,alpha) Gauss interfaceCompression;
//    div(rhoPhi,U) Gauss limitedLinearV 1;
}

laplacianSchemes

```

```
{
    default          Gauss linear corrected;
}

interpolationSchemes
{
    default          linear;
}

snGradSchemes
{
    default          corrected;
}

fluxRequired
{
    default          no;
    p_rgh;
    pcorr;
    alpha.water;
}

// ***** //
```

B.3. waveDyMFoam.C

```

/*-----*\
=====
\\      /  F ield      |  OpenFOAM: The Open Source CFD Toolbox
\\      /  O peration  |
\\      /  A nd        |  Copyright (C) 2011–2016 OpenFOAM Foundation
  \\/    M anipulation |

```

License

This file is part of OpenFOAM.

OpenFOAM is free software: you can redistribute it and/or modify it under the terms of the GNU General Public License as published by the Free Software Foundation, either version 3 of the License, or (at your option) any later version.

OpenFOAM is distributed in the hope that it will be useful, but WITHOUT ANY WARRANTY; without even the implied warranty of MERCHANTABILITY or FITNESS FOR A PARTICULAR PURPOSE. See the GNU General Public License for more details.

You should have received a copy of the GNU General Public License along with OpenFOAM. If not, see <http://www.gnu.org/licenses/>.

Application

interDyMFoam

Group

grpMultiphaseSolvers grpMovingMeshSolvers

Description

Solver for 2 incompressible, isothermal immiscible fluids using a VOF (volume of fluid) phase-fraction based interface capturing approach, with optional mesh motion and mesh topology changes including adaptive re-meshing.

```

/*-----*/

```

```

#include "fvCFD.H"
#include "dynamicFvMesh.H"
#include "CMULES.H"
#include "EulerDdtScheme.H"
#include "localEulerDdtScheme.H"
#include "CrankNicolsonDdtScheme.H"
#include "subCycle.H"
#include "immiscibleIncompressibleTwoPhaseMixture.H"
#include "turbulentTransportModel.H"
#include "pimpleControl.H"
#include "fvOptions.H"

```

```
#include "CorrectPhi.H"
#include "localEulerDdtScheme.H"
#include "fvcSmooth.H"

#include "relaxationZone.H"
#include "externalWaveForcing.H"
// * * * * * //

int main(int argc, char *argv[])
{
    #include "setRootCase.H"
    #include "createTime.H"
    #include "createDynamicFvMesh.H"
    #include "initContinuityErrs.H"

    #include "readGravitationalAcceleration.H"
    #include "readhRef.H"
    #include "gh.H"
    #include "readWaveProperties.H"
    #include "createExternalWaveForcing.H"

    pimpleControl pimple(mesh);

    #include "createControls.H"
    #include "createRDeltaT.H"
    #include "createFields.H"
    #include "createMRF.H"
    #include "createFvOptions.H"

    volScalarField rAU
    (
        IOobject
        (
            "rAU",
            runTime.timeName(),
            mesh,
            IOobject::READ_IF_PRESENT,
            IOobject::AUTO_WRITE
        ),
        mesh,
        dimensionedScalar("rAUf", dimTime/rho.dimensions(), 1.0)
    );

    #include "correctPhi.H"
    #include "createUf.H"

    turbulence->validate();

    if (!LTS)
```

```

{
    #include "CourantNo.H"
    #include "setInitialDeltaT.H"
}

// * * * * * //
Info<< "\nStarting time loop\n" << endl;

while (runTime.run())
{
    #include "readControls.H"

    if (LTS)
    {
        #include "setRDeltaT.H"
    }
    else
    {
        #include "CourantNo.H"
        #include "alphaCourantNo.H"
        #include "setDeltaT.H"
    }

    runTime++;

    Info<< "Time = " << runTime.timeName() << nl << endl;

    // --- Pressure-velocity PIMPLE corrector loop
    while (pimple.loop())
    {
        if (pimple.firstIter() || moveMeshOuterCorrectors)
        {
            scalar timeBeforeMeshUpdate = runTime.elapsedCpuTime();

            mesh.update();

            if (mesh.changing())
            {
                Info<< "Execution time for mesh.update() = "
                    << runTime.elapsedCpuTime() - timeBeforeMeshUpdate
                    << " s" << endl;

                gh = (g & mesh.C()) - ghRef;
                ghf = (g & mesh.Cf()) - ghRef;
            }

            if (mesh.changing() && correctPhi)
            {
                // Calculate absolute flux from the mapped surface velocity

```

```

        phi = mesh.Sf() & Uf;

        #include "correctPhi.H"

        // Make the flux relative to the mesh motion
        fvc::makeRelative(phi, U);

        mixture.correct();
    }

    if (mesh.changing() && checkMeshCourantNo)
    {
        #include "meshCourantNo.H"
    }
}

#include "alphaControls.H"
#include "alphaEqnSubCycle.H"

relaxing.correct();

mixture.correct();

#include "UEqn.H"

// --- Pressure corrector loop
while (pimple.correct())
{
    #include "pEqn.H"
}

if (pimple.turbCorr())
{
    turbulence->correct();
}
}

runTime.write();

Info<< "ExecutionTime = " << runTime.elapsedCpuTime() << " s"
    << "   ClockTime = " << runTime.elapsedClockTime() << " s"
    << nl << endl;
}

Info<< "End\n" << endl;

return 0;
}
// *****

```